Discretisation of the angular two-point correlation function

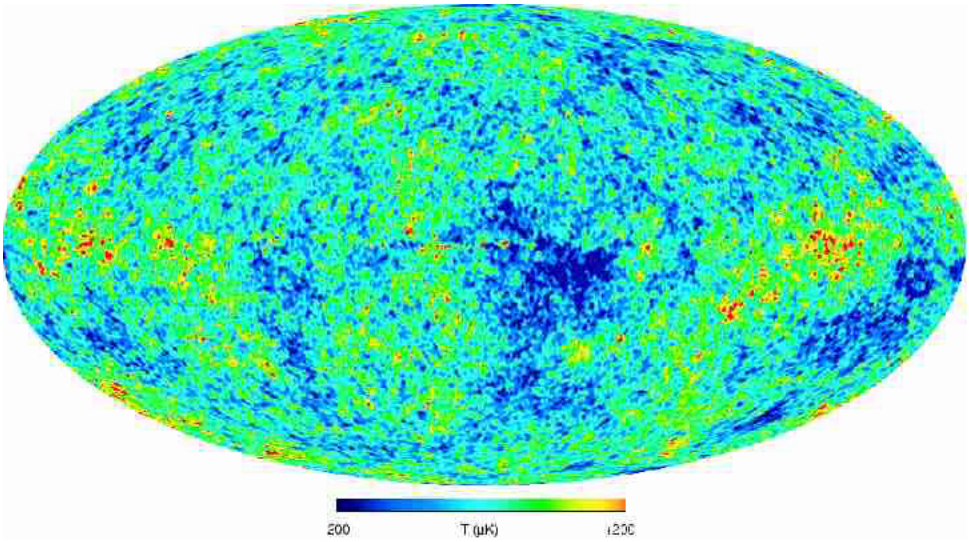

Candidata Scientiarum thesis by
Benedicte Selmer

Institute of Theoretical Astrophysics
University of Oslo
Norway

June 2003

Cover picture: The map is a "internal linear combination" of the WMAP K, Ka, Q, V, and W band maps. The maps are combined in such as way as to maintain unity response to the CMB while minimizing foreground foreground contamination. Note that there is a chance alignment of a particularly warm feature and a cool feature near the Galactic plane (Bennett, 2003b). A higher quality rendering of the map is available on the LAMBDA web site, <URL: http://lambda.gsfc.nasa.gov/>.

Preface

This master thesis is part of the large scale research that precedes the Planck[1] mission. In short, Planck is a satellite due to be launched by the European Space Agency (ESA) in 2007. The satellite is designated to image the anisotropies of the Cosmic Microwave Background (CMB) radiation over the complete sky. Norway, represented by the University of Oslo (UiO), is participating with both payload development and research.

Norway's scientific contribution will mainly be in the following four areas of research: the angular correlation function, non-Gaussianity, cluster science and galactic foregrounds caused by late stages of stellar evolution.

During the time I have been working on this thesis, the following people have been attached to the Planck project at the UiO: Professor Per B. Lilje, Torstein O. Sæbø, Hans Kristian K. Eriksen and Dmitri Novikov. Professor Per B. Lilje is Norway's co-investigator of the Planck project, manager of research and payload development and the Norwegian representative at Planck meetings. Dmitri Novikov held a post-doc position on the project, and has non-Gaussianity as his field of research. Torstein O. Sæbø and Hans Kristian K. Eriksen have both completed their MSc.-theses on CMB research, Torstein O. Sæbø on the angular correlation function and Hans Kristian K. Eriksen on N-point correlation functions and non-Gaussianity. H.K.K. Eriksen is now a Ph.D. student.

Purpose and outline of the thesis

The study of correlation functions is essential in understanding how the large scale structures we see in the sky are grouped. The description of how they are grouped is related to the physics of the Universe when it was just about 10^{-34}s old.

Today the most common way of presenting CMB results is through the angular power spectrum. The angular two-point correlation function is the real space equivalent of the power spectrum and in search of faster methods to determine the power spectrum from CMB sky maps, I was encouraged to take a closer look at this function to see if it might hold the key to a faster, and perhaps at the same time more precise, way of getting the information we want from the CMB.

The purpose of this thesis is twofold: 1) develop analytical expression to take a closer look on how binning of data, *e.g.* in purpose of analysis, might effect the result-

[1] See Section 1.9.5 for more information about the Planck project

ing correlation function, and 2) investigate the statistical properties of the correlation function with the intention of using it in maximum likelihood analysis.

In short the outline of this thesis is as follows: Chapter 1 gives a general introduction to the field of cosmology and the cosmic microwave background, while Chapter 2 makes the reader acquainted with the two main "characters" of this thesis, the power spectrum and the two-point correlation function. In Chapter 3 I derive analytical expressions for the two-point correlation function, and in Chapter 4 the results of the investigation on how discretisation and limited sky coverage affects the correlation function and the power spectrum, is presented. The results of the examination of the statistical distributions of the correlation function is found in Chapter 5 along with an introduction to maximum likelihood analysis and the derivation of two-point two-point covariance matrices. In Chapter 6 I give a short summary of the work and results in the thesis, and also point out some problems that might be worth investigate in future work on the use of the correlation function in CMB analysis through the maximum likelihood method.

Acknowledgements

Although *my* name is the only one to appear on the front page of this thesis, there is no doubt that this thesis would never have become what is had it not been for the many who have given me support along the way.

First I would like to thank my supervisor, Professor Per B. Lilje, for giving me an interesting and challenging thesis, and for helpful and critical remarks during the writing of this thesis. I would also like to thank Krzysztof M. Górski at ESO[2], Garching bei Munchen, who first came up with the idea behind this thesis.

A special thanks goes to Frode K. Hansen, Hans Kristian K. Eriksen and Torstein O. Sæbø. To Frode for pulling me out of all the smaller and larger pitfalls I have stumbled into during my work, patiently answering all my questions whether it be on cosmology, statistics or computer programming. Without his outstanding ability to convert the most complex theory into simple and comprehensive language, this thesis would with out doubt have been a much heavier task to complete. To Hans Kristian who's ingenious Correlation Suite made my calculations and simulations run smoothly, but also for all the clarifying discussions we have had. And to Torstein for useful discussions and fun companionship on our journeys to Munich and Alpbach.
I would also like to thank Susanne Øverlie for teaching me that it is always possible to find a solution, even when seemingly standing at a dead end.

And of course I would like to thank my family and all my friends for their faithful support during these years.

[2]European Southern Observatory.

Finally I would like to thank Lars Ballangrud for his endless patience, love and support. Without him by my side this thesis would have been really tough to get through.

Benedicte Selmer, Oslo, June 2003

Contents

List of Figures

List of Tables

Chapter 1

The Cosmic Microwave Background

In this chapter I will give a general description of the basic physical processes involved in producing the fluctuations of the Cosmic Microwave Background (CMB), and of the processes that can cause alterations of the pure CMB signal on its way towards us. I also give a brief description of various foregrounds, inflation, cosmological parameters, past and present CMB experiments and computational tools used during the work on this thesis. But first I will start with a brief introduction to cosmology and the history of CMB research. Most of this chapter is based on reviews and books by Tegmark (1995), Partridge (1995), Peacock (1999) and Kosowsky (2002).

1.1 Introduction

Cosmology is the branch of astrophysics which studies the Universe as a whole, its origin, evolution and fate. It is a relatively new science, but has a history that can be traced back to the ancient Greek philosophers who challenged the myths of creation and tried to make sense of the vastness around us.

From the humble beginning in the 1920s and until the mid-1960s, cosmology was at the periphery of the physical sciences and almost completely starved for data. This stands in sharp contrast to today's situation, when the field of cosmology has just entered the era of precision cosmology. Researchers are streaming to the field, as huge quantities of data containing a wealth of information about the properties and evolution of the Universe we live in are coming into the hands of the scientific community. At the centre of this revolution we find the CMB radiation. Today this radiation is manifested as a 2.73 K thermal background, but its origin is from when the Universe was merely 300.000 years old and had an overall temperature of 3000 K. As a matter of fact, the CMB radiation provides a unique direct image of the Universe from almost as far back in time as we can hope to see.

The radiation we observe in the microwave background today was once in thermal equilibrium with the primordial plasma of the Universe. At that time the Universe was highly, but not perfectly, uniform. Thus, the CMB radiation is extremely uniform, varying in temperature by only a few parts in 10^5. Had it been perfectly uniform, then subsequently no structures would have formed.

At the time imaged by the CMB, the Universe was also very simple, which is why it is extremely well-described by linear perturbation theory around a completely homogeneous and isotropic spacetime, and also why the physical processes relevant at that time are all relatively simple and very well understood. So by studying the small temperature and polarisation fluctuations in the CMB, we get valuable information about the variations in density and velocity in the early Universe. This information enables us to set very precise constraints on the overall properties of the Universe and makes the CMB a unique astrophysical tool in the quest to understand the Universe we live in.

1.2 The history of CMB research

This brief historical perspective is based on reviews by Fraser et al. (1995), Partridge (1995) and Kosowsky (2002).

There are some questions humankind has been asking itself as far back in history as we can go: How old is the Universe? Does it have any boundaries? How did it form? The answers to these questions were long only within the realms of philosophy and religion, but today we are beginning to see the contours of definite answers to these questions thanks to a few scientists who at the beginning of the 20th century let their curiosity and intuition guide them off the tracks of mainstream physics and into to the strange, unfamiliar landscape that was to become cosmology.

In 1927, the Belgian astronomer George Lemaître presented a theory of an expanding Universe that had a beginning in time. He proposed the initial Universe as a highly compressed state of matter, which he called "*l'atome primitif*", and suggested that the Universe was born in a primordial explosion. The idea was presented in a Belgian journal, but went unnoticed until Hubble's discovery of the expanding Universe in 1929. Although Lemaître's idea differ from modern cosmology in several other respects, he is rightfully looked upon as the father of the Big Bang theory.

The modern version of Lemaître's idea of a giant primordial explosion was worked out in the late 1940s by George Gamow, Ralph Alpher and Robert Herman. Gamow and his colleagues introduced the Hot Big Bang model as a mean to build up elements heavier than hydrogen in the early Universe, and as a by-product of their work they realized that the present Universe would be filled with a blackbody relic of the Hot Big Bang. This blackbody relic would be calculable and of non-zero temperature, and in 1948 Alpher and Herman predicted that the relic background should have a

temperature of about 5 K (Alpher and Herman, 1949). Over the next decade Gamow, Alpher, Herman and their collaborators made a variety of estimates of the background temperature which spanned from 3 to 50 K (see *e.g.* Alpher et al., 1953). The lack of a definitive temperature and of suggestions of its detectability with available technology long contributed to a lack of interest in the prediction among experimenters, despite the immense development of microwave technology during World War II.

In the same year Alpher and Herman published their first temperature predictions of the relics of the Hot Big Bang, Fred Hoyle, Hermann Bondi and Thomas Gold put forward a totally different idea, the Steady State theory (*e.g.* Hoyle, 1948). In this theory the Universe was also expanding, but the idea of an initial explosion was rejected. The Universe, they said, had always been in a "steady state", without a beginning, and without there having to be an end.

In the late 1950s and early 1960s, the fundamental question of whether the Universe had a beginning in time or not, was debated in full public. The adherents of the Big Bang cosmology formulated by Gamow and his colleagues, stood acrimoniously against the supporters of the Steady State model of Bondi, Gold and Hoyle. The controversy was not ended until the discovery of the CMB gave crucial support to the Big Bang theory.

In the early 1960s A.G. Doroshkevich and I.D. Novikov (Doroshkevich and Novikov, 1964) emphasised the detectability of a microwave blackbody as a basic test of Gamow's Hot Big Bang model, and about the same time, R.H. Dicke and his collaborators at Princeton University began searching for the radiation.

Two radio astronomers at Bell Laboratories in New Jersey, Arno Penzias and Robert Wilson, serendipitously discovered the CMB in 1964, using a microwave horn radiometer originally intended for experimenting with telecommunication satellites. During their research, they detected a uniform noise source they gradually concluded had to come from the sky. After getting in touch with R.H. Dicke and his collaborators Peebles, Roll and Wilkinson at Princeton, they realized that what they had detected was the radiation background predicted by Alpher and Herman. Penzias and Wilson published their results in a brief paper (Penzias and Wilson, 1965), closely preceded by a companion paper by the Princeton group explaining the cosmological significance of the discovery (Dicke et al., 1965).

In 1978 Penzias and Wilson was awarded the Nobel Prize of Physics for their revolutionary discovery.

The announcement of Penzias and Wilson's discovery was followed by an explosion of work related to the Big Bang model of the expanding universe. Theorists soon realized that fluctuations in the CMB temperature would have fundamental significance as a reflection of the initial perturbations which grew into galaxies and clusters. The first estimated amplitudes of the temperature fluctuations were one part in a hundred, but experimenters found no observed fluctuations at that level of sensitivity. Over

the next twenty-five years, theorists continually revised their estimates downwards as experimentalists came up with more and more stringent upper limits. By the end of the 1980s, the limits on the fluctuations were well below one part in 10^4, and in 1990 the COBE satellite finally detected fluctuations at the level of a few parts in 10^5 (Smoot, 1992). These results, just consistent with structure formation in inflation-motived Cold Dark Matter (CDM) cosmological models, were soon confirmed by several ground-based (Bersanelli et al., 1994; Baker, 1999) and balloon-borne measurements (de Bernardis, 1990; Fischer, 1991).

There could have been made detections of the CMB before Penzias and Wilson, the first ones in the early 1940s (McKellar, 1940; Adams, 1941). During his work on molecules in interstellar space, Andrew McKellar observed some characteristically sharp lines in the violet and ultraviolet region that he could not determine the source of. He suggested that they might arise from transitions between rotational levels of interstellar molecules at extremely low temperature and calculated the maximum "effective" temperature to be 2.7 K. McKellar's discovery was confirmed by W. S. Adams in 1941, using the Coudé spectrograph of the Mount Wilson Observatory. Unfortunately the significance of these observations was not understood and the results forgotten.

1.3 The underlying cosmology

After the Big Bang, the Universe expanded and cooled. When the Universe was about 300.000 years old, the temperature had dropped to 3000 K and electrons and protons started to combine into hydrogen in a process called recombination. Prior to this, the Universe had been filled with an opaque fluid of coupled baryons, electrons and photons, called the photon-baryon fluid. The opacity was caused by the very high cross section of the free electrons to Thompson scattering. But as a consequence of the recombination process, the photons decoupled from the baryons and began to propagate freely across the Universe. It is this very first light that we observe as CMB radiation today.

When the CMB radiation began to propagate freely during the recombination era, the Universe was a conceptually simple place filled with baryons, electrons, neutrinos, photons and dark matter particles. The Universe was also very close to being homogeneous and isotropic, with only small perturbations in density and velocity. The requirement of the unperturbed Universe to be homogeneous and isotropic determines the background spacetime-metric to be of the standard Robertson-Walker form

$$ds^2 = dt^2 - a^2(t)\left[\frac{dr^2}{1-kr^2} + r^2(d\theta^2 + \sin^2\theta)d\phi^2\right]. \tag{1.1}$$

In this metric the spatial evolution of the Universe is expressed through the cosmological scale factor $a(t)$, given by the Friedmann equations:

$$8\pi G\rho = \frac{3}{a^2}\left(kc^2 + \dot{a}^2\right), \tag{1.2}$$

$$\frac{8\pi G p}{c^2} = -\frac{2\ddot{a}}{a} - \frac{\dot{a}^2}{a^2} - \frac{kc^2}{a^2}. \quad (1.3)$$

Depending on the value of k and the matter density Ω_0, the Friedmann-Robertson-Walker (FRW) spacetime can have three different flavours of spatial curvature: positive, negative or flat. The question of the spatial curvature of the background spacetime is important because it determines whether the Universe is finite or infinite, and because it is connected to the fate of the Universe. The CMB can provide us with the cleanest and most powerful probe of the geometry of the Universe (Kamionkowski et al., 1994), and might therefore give us the answer to this fundamental question.

The sound horizon

The fluctuations in the microwave background depend on two basic physical scales, the sound horizon at last scattering, r_s, and the Silk damping scale, τ_{LSS}.

The sound horizon at last scattering, r_s, is simply the sphere defined by the distance a sound wave could have propagated in the photon-baryon fluid from the time of Big Bang until decoupling occurred. Since the photons where coupled to the baryons before recombination, perturbations evolving in the photon-baryon fluid would set up standing acoustic oscillations, or sound waves, in the fluid. Thus the sound horizon at last scattering, r_s, represents the largest scale on which any causal physical process can influence the primordial plasma.

The surface from which we see the photons last scattered when they began propagating freely across the Universe, we call the last scattering surface (LSS). The LSS is a spherical shell, so any feature in the CMB of a given size will subtend an angle θ on the sky. Thus, when working with CMB fluctuations it is often convenient to use spherical harmonic functions Y_{lm}, and in this representation the angular scale equivalent to the angle θ is given by the multipole l

$$l \simeq \frac{\pi}{\theta}. \quad (1.4)$$

If primordial perturbations were present on all scales prior to recombination, the resulting CMB fluctuations will appear as a featureless power law at large scales (*i.e.* at small l), while the scale at which they began to depart from this behaviour corresponds to the sound horizon. This is precisely the behaviour observed by current measurements, which show a prominent peak in the power spectrum at an angular scale of a degree ($l \simeq 200$). Also, if the CMB power spectrum exhibits acoustic oscillations, then the acoustic peaks appear at harmonics of the sound horizon. Measurements of the angular scales that such features subtend on the sky provide a very general and precise probe of the curvature of the Universe.

Silk damping

Because of Compton scattering of photons off electrons in the photon-baryon fluid, the coupling between the baryons and the photons was not completely perfect. The large

number of free electrons in the fluid caused frequent scattering of the photons, and since the electrons were coupled to the protons through Coulomb interaction, the photons indirectly dragged the baryons with them as they random-walked out of overdense regions in the fluid. This way hot and cold regions got mixed and adiabatic baryonic fluctuations were damped (Partridge, 1995).

During recombination electrons and protons combined to form neutral hydrogen, causing an enormous decrease in the number of free electrons. Since recombination did not happen instantaneously throughout the Universe, the LSS is not infinitely thin, but has a thickness τ_{LSS}. As the number of free electrons decreased, the mean free path of the photons increased until it reached the thickness of the LSS. Thus the effective Silk damping scale became equal to τ_{LSS}, and fluctuations with wavelengths smaller than the mean free photon path were damped. After recombination the free electrons vanished and Silk damping ceased.

Projection effect

The thickness of the LSS influences the primordial fluctuations in the CMB not just through Silk damping. When measuring the CMB temperature in a given direction in the sky, photons at different distances within the LSS are averaged, hence this can be looked upon as a projection effect that washes out fluctuations on scales smaller than τ_{LSS}.

1.4 Primary fluctuations

Blackbody radiation in a perfectly homogeneous and isotropic universe must be at a uniform temperature, by assumption. When perturbations are introduced, three elementary physical processes can produce a shift in the blackbody temperature of the radiation emitted from a particular point in space. So when the CMB photons decoupled from the baryons during the recombination era, they took with them three different imprints of the region on the LSS from which they last scattered. The effects of the different processes will be discussed in more detail later in this section, but first I will take a look at the evolution of first-order perturbations of the underlying cosmology.

The evolution of first-order perturbations in the metric and the various energy density components of the Universe are described by the following sets of equations:

- The photons and neutrinos are described by their distribution functions. The energy density of both components is given by the blackbody distribution, and the time evolution by the Boltzmann equation.
- The dark matter and baryons are both well described by the Euler and continuity equations for their densities and velocities.

- For the metric perturbations, both the evolution and the connection to the matter perturbations are contained in the Einstein equations.

Setting the correct initial conditions for the perturbations of the CMB involves specifying the value of each variable in the equations mentioned above in the limit where the conformal time η, defined by $\eta \equiv \int \frac{dt}{a}$, goes to zero. Numerically determining the initial conditions is difficult for two reasons: in this limit the equations are singular, and they also become increasingly numerically stiff.

A variety of numerical techniques have been developed for evolving the equations above. Particularly important is the line-of-sight algorithm developed by Seljak and Zaldarriaga (Seljak and Zaldarriaga, 1996), implemented in the publicly available CMBFAST code (see Section 1.10.1, and also `<URL: http://ascl.net/cmbfast.html>` or `<URL: http://www.cmbfast.org/>`).

1.4.1 The Sachs-Wolfe effect

The Sachs-Wolfe effect is the dominant mechanism on large scale for perturbations of the primordial CMB, and arise from perturbations of the gravitational potential Φ at last scattering (Sachs and Wolfe, 1967). The perturbations have two effects on the photons as they climb out of the potential wells: gravitational redshift and time dilation. Assuming that the Universe started out with adiabatic initial conditions, an assumption strongly supported by CMB measurements, the combined general relativistic effect of this is (Hwang et al., 2002)

$$\frac{\Delta T}{T} = \frac{\delta\Phi}{3c^2}. \tag{1.5}$$

1.4.2 The Doppler effect

If radiation at a particular point is moving with respect to the observer, the observer will see a Doppler shift in the wavelength of the radiation. All density perturbations within the horizon scale are accompanied by velocity perturbations, and these perturbations appear as oscillations in the photon-baryon fluid. Hence photons last scattered by matter moving away from us, received a Doppler redshift as they left the LSS. This effect dominates at intermediate scales and can be written

$$\frac{\Delta T}{T} = \frac{\delta\mathbf{v}\cdot\mathbf{r}}{c}. \tag{1.6}$$

1.4.3 The adiabatic effect

This effect dominates on small scales, and is caused by the fact that if the radiation density increases via adiabatic compression of the photon-baryon fluid, there will be an increase in the intrinsic temperature of the fluid at that given point in space. As recombination occurs at a temperature of $T_{rec} = 3000$K, hot and cold spots in the fluid recombine at different times. Because they recombine later, the denser spots are less cosmologically red-shifted, and hence they appear hotter. This is why photons last

scattered from an overdense region have a higher intrinsic temperature than photons scattered from less dense regions on the LSS.

Assuming linear growth, the fractional temperature perturbation in the radiation equals one third of the fractional density perturbation.

$$\frac{\Delta T}{T} = \frac{\delta}{3}, \tag{1.7}$$

where δ is given by

$$\delta \equiv \frac{\delta\rho}{\rho}. \tag{1.8}$$

The contributions to the temperature fluctuations in the CMB from the three effects discussed above, are summarised by the equation

$$\frac{\Delta T}{T} = \frac{\delta\Phi}{3c^2} - \frac{\delta\mathbf{v}\cdot\mathbf{r}}{c} + \frac{\delta}{3}, \tag{1.9}$$

where $\mathbf{r}$ is the comoving distance to the last scattering surface, and the fields $\delta\Phi$, $\delta\mathbf{v}$ and δ are to be evaluated at the time of recombination.

Adiabatic or isocurvature initial conditions

According to whether the gravitational potential perturbations $\delta\Phi_{\gamma\mathrm{b}}$ from the photon-baryon fluid is zero or non-zero as conformal time goes to zero, the initial conditions of the equations mentioned at the beginning of this section can be divided into two categories: isocurvature or adiabatic, respectively. In cases of purely one or the other type the calculations of the equations simplifies significantly. Note that in the case of purely isocurvature initial conditions, the Sachs-Wolfe effect in Equation (1.5) is larger by a factor of six.

If the Universe started off with adiabatic initial conditions, *i.e.* with non-zero gravitational potential perturbations $\delta\Phi_{\gamma\mathrm{b}}$, the ratio of baryon to photon number densities is constant in space, and the photon-baryon fluid can be treated as a single fluid. Because of the tight coupling between radiation and matter in the fluid, matter would feel a significant pressure that would counteract any tendency for the matter to collapse gravitationally. As mentioned earlier, perturbations evolving in the density, velocity and gravitational potential fields in this fluid would set up standing acoustic waves on scales smaller than the sound horizon, r_s. For perturbations on larger scales, we get the Sachs-Wolfe effect in Section 1.4.1. With adiabatic initial conditions, the location of the gravitational potential wells and the overdensities also coincide, so that the first and the third term in Equation (1.9) partially cancel.

If on the other hand the Universe started off with isocurvature initial conditions, *i.e.* with gravitational potential perturbations $\delta\Phi_{\gamma b} = 0$, the baryon and photon number densities would vary in such a way that they compensate each other. So instead of evolving in curvature, these perturbations would evolve in entropy. Evolution of isocurvature perturbations attempts to keep the density constant by making the matter perturbations decrease while the amplitude of the fluctuations in the radiation field increase. Hence, in a matter-dominated Universe, the entropy perturbations at late times are carried entirely by the photons. This leads to an increased amplitude of the CMB anisotropies in isocurvature models compared to adiabatic ones. Isocurvature perturbations can arise from causal processes like phase transitions.

1.5 Polarisation

A more detailed discussion of the CMB polarisation and its power spectra is outside the scope of this thesis, but it is nevertheless worth mentioning.
In contrast to the temperature fluctuations which predominantly reflect density perturbations, polarisation fluctuations mainly reflect velocity perturbations at last scattering. As electrons at last scattering experienced an anisotropic radiation field, non-zero polarisation is inevitable. If such polarisation fluctuations are detected, the polarisation spectra will reveal perturbations of the velocity field, and possible also the presence of gravitational waves and primordial magnetic fields, present at last scattering. Polarisation also proves a much thinner volume at LSS.

1.6 Secondary fluctuations

The effects under this heading is primarily referring to processes that have affected the CMB photons on their way from the last scattering surface to us.

1.6.1 Integrated Sachs-Wolfe effect

The Sachs-Wolfe effect is often dived into two effects, the effect described in section 1.4.1 and the Integrated Sachs-Wolfe (ISW) effect. The latter arises when gravitational potentials are evolving with time and has three manifestations: Early ISW, Late ISW and the Rees-Sciama effect (Tegmark, 1995).

In a matter-dominated universe gravitational potentials remain constant in time as long as the density fluctuations evolve linearly. Thus in models where the Universe is matter-dominated during the time the CMB radiation propagates freely, the Integrated Sachs-Wolfe effect is zero. In models with matter density significantly less than the critical density (*e.g.* the ΛCDM models), matter-radiation equality occurs late enough for the gravitational potentials to evolve when the CMB radiation decouples. This leads to a non-negligible Integrated Sachs-Wolfe effect.

The ISW effect on a single photon is given by the integral over $\dot{\Phi}$, the conformal time derivative of the gravitational potential, at a fixed position in space

$$\frac{\Delta T}{T} = \int \dot{\Phi}[\mathbf{r}(t), t]dt,$$

where $\dot{\phi}$ is the conformal time derivative of the gravitational potential at a fixed position in space. The three manifestations of the ISW correspond to the three cases when $\dot{\Phi} \neq 0$.

Early ISW

Shortly after recombination, the photon contribution to the density of the Universe was still not altogether negligible. As a result, the gravitational potential decayed somewhat.

Late ISW

If the cosmological constant $\Lambda > 0$, the Universe will eventually become vacuum dominated. If the sum of the total energy density and the cosmological constant $\Omega + \Omega_\Lambda \neq 1$, the Universe may become curvature dominated. In both cases spacetime will be stretched, causing a redshift of the CMB photons. This is known as the late ISW effect, since vacuum energy and curvature become important only at low redshifts.

The Rees-Sciama effect

Once non-linear structures such as galaxy clusters form, linear perturbation theory breaks down and the result from linear perturbation theory that $\dot{\phi} = 0$, is no longer valid. The contribution to the ISW from non-linear perturbations is called the Rees-Sciama effect.

Weak gravitational lensing

The ISW effect can be thought of as the gravitational fields giving the photons momentum kicks parallel to their flight paths, causing a a change in their energy, but not their paths.

There is also a twin effect to the ISW, where the gravitational fields give the photons momentum kicks perpendicular to their flight paths. This leaves the energy unchanged, but deflects the photon trajectories, which means that it is essentially an issue of weak gravitational lensing. The effect of this angular jumbling is that power is redistributed from the peaks of the power spectrum to the troughs, preserving the total power in the fluctuations. Although the effect is small, typically a few percent, it may well be detectable in the data from WMAP and the upcoming Planck experiment.

1.6.2 Sunyaev-Zel'dovich effect

The peculiar velocity, $\mathbf{v}$, and density fluctuations, δ, can only influence the CMB photons after recombination if the baryons become reionized in other ways than ISW, locally or throughout all of space. Local reionization, confined to for instance hot clusters of galaxies, manifests itself in two ways. Both are known as the Sunyaev-Zel'dovich (SZ) effect (Sunyaev and Zel'dovich, 1970, 1980; Rephaeli, 1995):

i) If a cluster of galaxies is moving away from us, Thompson scattering of CMB photons off the hot intra-cluster gas will cause a Doppler redshift in the direction of the cluster. This corresponds to the impact of $\mathbf{v}$ on CMB photons and is known as the **kinematic SZ-effect**.

ii) The high temperature of the free electrons will, independent of the cluster velocity, distort the Planck spectrum by depleting the low frequency tail and overpopulate the high frequency tail. This, known as the **thermal SZ-effect**, appears as a redshift below and as a blueshift above 218 GHz, and corresponds to the impact of the density fluctuations δ on CMB photons.

Both kinematic and thermal SZ-effect cause spectral distortions of the CMB radiation as it passes through hot ionized regions (Birkinshaw, 1999). The impact on the CMB can be quite large in the directions of cluster cores, but is likely to be negligible on the overall CMB power spectrum (Persi et al., 1995).

1.6.3 Reionization

If reionization occurred throughout space, the effects on the CMB power spectrum would be quite radical. One would get a new last scattering surface where the temperature observed in a given direction on the sky would be the weighted average of the temperature of part of the $z = 1000$ last scattering surface.
This smearing would be on an angular scale corresponding to the angle subtended by the sound horizon at the redshift of the latest scattering. Thus by increasing the effective Silk damping scale, reionization would suppress temperature fluctuations on scales smaller than the new r_s. D.N. Spergel et *al.* claim to have found such a signature in the WMAP data at a redshift of $z \sim 20$ (Spergel, 2003).

1.6.4 Non-linear effects

Apart from the Rees-Sciama effect in Section 1.6.1, the discussion has so far assumed that the CMB power spectrum is perfectly described by linear perturbation theory. Since the temperature perturbations are so small, linear theory is a very good approximation. But on small scales non-linear effects become important, and can even dominate over the linear contributions.

The most important non-linear effects are the combined effect of the thermal and kinetic Sunyaev-Zeldovich effect described in Section 1.6.2, the so-called Ostriker-Vishniak effect (Ostriker and Vishniac, 1986) and gravitational lensing by large-scale structures (Seljak, 1996). All three effects are measurable and give important additional constraints on cosmology.

1.7 Foregrounds

Whether the goals of determining the different cosmological parameters to a level of a few percent can actually be achieved, depends on the level of foreground contamination and systematic effects (see *e.g.* Tegmark and Efstathiou, 1996). As foreground effects tend to depend strongly on multipoles l and on frequency ν, knowledge about how the different foregrounds depend on both is equally important.

1.7.1 Extragalactic point sources

The l-dependence for point sources is well known, but the frequency dependence in the microwave region is not. But what is known, is that radio and infrared point sources contribute to the same range of multipoles $l = [10^3 - 10^4]$, but to different ranges of frequency. Radio point sources contribute mainly to the frequency range of $\nu = [0 - 50]$ GHz, while infrared point sources contribute to the range $\nu = [500 - 1000]$ GHz. WMAP and Planck will be observing in the frequency ranges $\nu = [30 - 1000]$ GHz, so accurate data about radio point sources above 50 GHz and infrared point sources at the high frequency end, is badly needed.

1.7.2 Diffuse galactic sources

There are three different major diffuse galactic contaminants: thermal dust, free-free and synchrotron emission. In addition there is also possibly emission in the microwave range from spinning and magnetic dust particles. All contaminants are caused by emission from diffuse blobs of gas.

Dust

Dust radiates significantly at microwave frequencies and is the dominant foreground emission component on frequencies above 70 GHz. As our galaxy contains large amounts of dust, the galactic foreground is a severe source of contamination in CMB observations. Dust emission usually has a spectrum that rises with frequency (see Figure 1.1), and is not uniformly distributed on the sky, but rather concentrated in the galactic plane, with fainter, but pervasive, diffuse emission on other parts of the sky.

Free-free and synchrotron emission

Free-free and synchrotron emission also radiates significantly at microwave frequencies. Free-free emission arise from electron-ion scattering, while synchrotron emission arises

from the acceleration of relativistic cosmic ray electrons in magnetic fields. Unlike dust, they have spectra that are falling with frequency, and as can be seen in Figure 1.1, the synchrotron emission dominates the free-free emission at frequencies below 30 GHz. But they also have some similarities with dust: in sky maps free-free and synchrotron emission is found in the galactic plane or as fainter diffuse emission on other parts of the sky.

The dust, free-free and synchrotron emission spectra cross each other at a frequency of around 70 GHz (see Figure 1.1), where the amplitude of the foreground emission is low enough to create a frequency window in which the cosmological temperature fluctuations dominated the foreground. Since these foregrounds have frequency spectra that differ from that of the CMB, the foregrounds can be separated from the CMB signal at other frequencies by measuring in several different frequencies and projecting out the portion of the signal with non-CMB frequency spectra.

Galactic foregrounds limit the area of clean sky available, thus increasing the error bars of the estimated CMB power spectrum as the inverse square root of the fraction of the sky. In addition, foreground subtraction will increase the noise in the CMB maps and thus cause a further increase in the error bars.

1.7.3 Local sources

Microwaves have wavelengths significant compared to geometric structures in the antenna and instrument, and there will therefore be sidelobes not totally insignificant out to 180°. Sidelobes from the Sun, the Moon, the Earth and other planets as well as electronic receiver noise, are also problems that have to be dealt with in CMB experiments, whether the experiment is ground-based, balloon-borne or a satellite mission. Groundbased and balloon-borne experiments also have to deal with atmospheric emission.

1.7.4 Systematic effects

Systematic effects such as sidelobes of the beam, calibration and striping in the maps from 1/f-noise, also degrade the sensitivity of CMB experiments.

A problem of a somewhat different nature is pixelisation noise. CMB maps are not continuous, but divided into pixels, which give rise to what is called pixelisation noise. The pixelisation noise can be described by a power spectrum $C_l(\nu)$ and treated on equal footing with the other contaminants. Most current experiments oversample the sky with respect to their beam, so the pixelisation noise is negligible.

Discreteness

A problem that resembles that of pixelisation noise, is discreteness. Discreteness enters when we do the analysis in practice, particularly when dealing with large quantities of

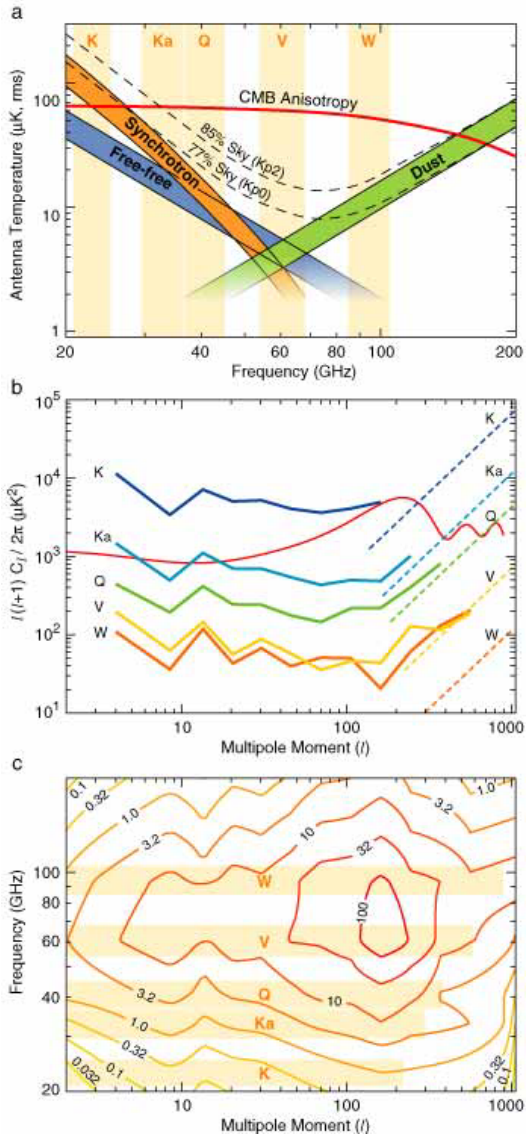

Figure 1.1: The WMAP frequency bands were chosen to be in a region where the CMB anisotropy dominates over the Galactic and extragalactic foreground emission. (a) show the spectra of the CMB and the Galactic emission modelled from the Maximum Entropy Method. (b) show the foreground power spectra for each WMAP band. The band-by-band point source fits to an l^2 term are shown in the dashed lines on the right. The power spectra are expected to asymptotically join these lines. Note that the total foreground spectrum (excluding point sources) go as $C_l \sim l^{-2}$. (c) The contour plot shows the ratio of CMB to foreground anisotropy power as a function of frequency and multipole moment. Reprinted from Bennett (2003a).

data. In order to handle large data sets, we often have to split the data into smaller parts of more manageable size. It has long been assumed that making data sets discrete in this way, have no or very little effect on the results of the analysis. Whether this is truly the case or not, will be looked into in greater detail in Chapter 4 of this thesis.

1.8 What can the CMB anisotropies tell us?

Before decoupling, the matter in the Universe was tightly coupled to the radiation and therefore had significant pressure, a pressure that counteracted any tendency for the matter to collapse gravitationally. During this epoch, density perturbations were setting up standing waves in the plasma. These waves left a distinctive imprint on the last scattering surface. Today these imprints can be seen in the power spectrum of the CMB and provides us with a basis for precision constraints on the cosmological parameters.

1.8.1 The different cosmological models

The CMB is the probe of cosmology most tightly connected to the fundamental properties of the Universe and least influenced by astrophysical complications, and thus has the potential to determine the fundamental cosmological parameters describing the Universe with percent-level precision. If this potential is realized, the standard model of cosmology would compare with the standard model of particle physics in terms of physical scope, explanatory power and detail of confirmation. The cosmological parameters determined from the CMB are model-dependent, *i.e.* different cosmological models predict different values for the different parameters. This is because the physical mechanisms that can introduce temperature fluctuations into the CMB, behave differently in the different models, thus leaving a distinct model-dependent imprint on the CMB.

Cold Dark Matter (CDM) models

The CDM models are the cosmological models most consistent with CMB observations, and has cold dark matter as the dominant component of the matter density.

In general, the ratio of CDM to the total matter density is assumed to be $\frac{\Omega_{CDM}}{\Omega_m} \simeq 0.7-0.9$, and it is also common to assume a Harrison-Zel'dovich spectrum. CDM models can be both adiabatic and isocurvature, but measurements tend to point towards models with adiabatic fluctuations. Figure 1.2 shows a typical power spectrum for an adiabatic CDM model.

The characteristic peaks and troughs in Figure 1.2 are produced by the three effects described in Section 1.4. The flat region a at low values of l, *i.e.* at large scales, is that dominated by the Sachs-Wolfe effect. At smaller scales, $\theta \leq 0.5^\circ$ or $l \geq 100$, Doppler perturbation dominate. And at even smaller scales, $l \approx 100-1000$, the power spectrum is dominated by the adiabatic effect.

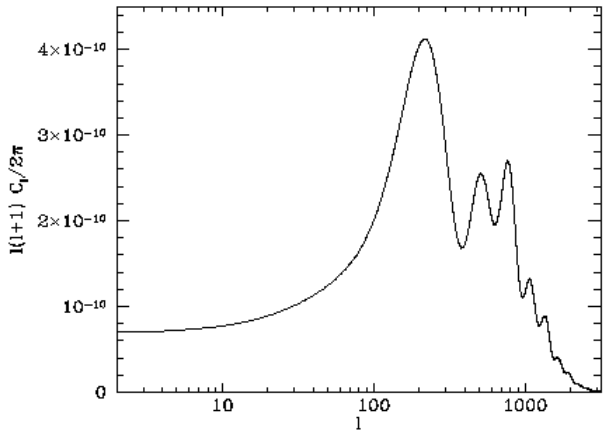

Figure 1.2: The angular power spectrum of a standard CDM model ($\Omega = 1, \Omega_b = 0.06, h = 0.5, n_s = 1$). Reprinted from Tegmark (1995).

The classic CDM model was closed and had no energy density except CDM and baryons, *i.e.* $\Omega_m = 1.0$ and $\Omega_{CDM} \sim 0.95$. This model has been ruled out by various constraints, supernovae, and the amplitude of perturbations on large scales compared to small scales. However, a variant CDM model, the ΛCDM class has become very popular in the last decade. In these models so-called vacuum energy, also called dark energy, is the dominant component. This vacuum energy is the modern variant of Einstein's cosmological constant Λ, and acts as repulsive force on the Universe to counteract for the tendency of matter to collapse gravitationally, causing the expansion of Universe to decelerate.

The other two components that contribute to the present density of the Universe in this model is baryonic matter and non-baryonic dark matter. Both dark matter and vacuum energy interacts with gravity, but their interaction with ordinary matter and radiation is extremely weak, there is slightly any interaction at all.

In the latest data from WMAP the total matter density to the critical density was found to be $\Omega_m = 0.29 \pm 0.07$, with $\Omega_b = 0.047 \pm 0.006$ and $\Omega_{CDM} = 0.24 \pm 0.08$, while the vacuum energy density was found to be $\Omega = 0.73 \pm 0.09$ (Spergel, 2003).

Hot Dark Matter (HDM) models

HDM models have hot dark matter, *e.g.* neutrinos of nonzero mass, as their dominant density component.

These models predict somewhat larger values of the temperature fluctuations $\Delta T/T$ on degree scales and above, than do comparable CDM models. But compared with observations, these models produce too little power on small scales compared to the power on large scales, to explain structure formation on scales of *e.g.* galaxies.

Baryon-only models

The earliest predictions of CMB fluctuations, made before dark matter and vacuum energy came into fashion, were naturally based on cosmological models of a purely baryonic Universe.

If the CMB fluctuations are as small as observed, the amplitude of the adiabatic fluctuations in the matter found in these models is much smaller than those found in dark matter models. This is because in the baryon-only models there are no potential-wells formed by dark-matter perturbations for the baryons to fall into after recombination. Hence, larger initial perturbations are required in order to produce the fluctuations observed on the surface of last scattering.

One way to avoid the small amplitudes of the CMB anisotropies predicted in adiabatic baryonic models, is to assume isocurvature perturbations. As these perturbations evolve in entropy and entropy perturbations primarily are carried by photons, there will be smaller matter perturbations and larger fluctuations in the radiation field in isocurvature models compare to adiabatic ones.

Inflationary models

By definition, inflation is a stage of accelerated expansion in the early Universe that most likely occurred when the Universe was only 10^{-34} seconds old. Inflation is not a precise theory, but rather a mechanism for exponential expansion of the universe which can be realized in a variety of specific physical models.

A very simple, broad, and well-motivated set of cosmological models are motivated by inflation: a universe described by a homogeneous and isotropic background with phase-coherent, power-law primordial perturbations which evolves only via gravitational instability. This set of cosmological models is relatively simple to calculate and also appears to fit all current data far better than any other proposed models. These are some of the predictions that the CMB can hope to test:

- The most basic prediction of inflation is that the curvature of the Universe is flat. The flatness problem was one of the fundamental motivations for considering inflation in the first place.

- Inflation generally predicts primordial perturbations which have a Gaussian statistical distribution.

- The simplest models of inflation give adiabatic primordial perturbations. More complex models of inflation results in dominant adiabatic perturbations with some admixture of isocurvature fluctuations.

- Inflation generically predicts primordial perturbations on all scales. Inflation further predicts that the primordial power spectrum should be close to a scale-invariant power law.

- Inflationary perturbations results in phase-coherent acoustic oscillations. The CMB temperature and polarisation power spectrum will together reveal coherent oscillations.

When inflation was introduced in the early 1980's, it was commonly believed that the inflationary scenario would result in the imprint of pure Gaussian fluctuations on the CMB. Since then it has become clear that in the more complicated models of the inflationary process, inflation can produce significant levels of non-Gaussianity. But, if inflation occurred, we will get strongly supporting evidence from the above signatures, along with precision measurements of the cosmological parameters describing our Universe. If on the other hand, inflation did not occur, we may not be able to recover cosmological parameters as precisely, but the CMB will still be equally important in finding the correct model of our universe. Over the next few years results from WMAP and the upcoming results from Planck will give the answer to these questions.

1.8.2 The different cosmological parameters

The parameters defining the cosmological model space can be broken down into three types: background cosmological parameters, parameters describing initial conditions and parameters for additional physical effects.

Background cosmological parameters

This type of parameters describes the underlying spacetime of the early Universe.

- Ω_{tot}, the ratio of the total energy density to the critical density $\rho_c = \frac{8\pi}{3H^2}$. This parameter determines the curvature of the Universe: $\Omega_{\text{tot}} = 1$ gives a flat universe, $\Omega_{\text{tot}} < 1$ an open universe and $\Omega_{\text{tot}} > 1$ a closed universe. Current measurements points towards a value close to $\Omega_{\text{tot}} = 1$ (Balbi, 2001; Melchiorri, 2000; Spergel, 2003).

- Ω_b, the ratio of the baryon density to the critical density. Predictions from primordial nucleosynthesis and observations of the deuterium abundance at high redshift puts strong constraints on this parameter (Tytler et al., 2000).

- Ω_m, the ratio of the dark matter density to the critical density. The sum of Ω_m and Ω_b gives the total matter parameter, $\Omega_0 = \Omega_m + \Omega_b$. Numerous evidence points to a value of $\Omega_0 = 0.3$ (Balbi, 2001; Melchiorri, 2000; Spergel, 2003).

- Ω_Λ, the ratio of vacuum energy density Λ to the critical density. Λ is the famous cosmological constant, which was reintroduced when an apparent acceleration in the expansion of the Universe was discovered (Riess, 1998; Perlmutter, 1999).

- h, the present Hubble parameter. Present estimates gives $h = 0.72$ km/s/Mpc with errors in the order of 10% (Plionis, 2002).

In addition to the parameters over, there are parameters describing additional contributions to the energy density of the Universe, from for instance quintessence.

Parameters describing initial conditions

These parameters give the physical conditions at the 'time' when the Universe was born.

- Q, the amplitude of the temperature fluctuations. This parameter was fixed to high accuracy by COBE (Bennett, 1996).
- n_s, the spectral index of initial adiabatic density fluctuations. Comparison of CMB and large scale structure measurements shows that n_s is close to unity.

Other parameters describing departures of the perturbations from a power law or a small admixture of isocurvature perturbations also belong under this heading.

Parameters for additional physical effects

These parameters describes miscellaneous additional physical effects that may have affected the evolution of the Universe prior to recombination.

- m_ν, a cosmologically significant neutrino mass.
- N_ν, the effective number of neutrino species.
- z_r, the redshift of reionization.

A realistic parameter analysis might include at least eight free parameters. For the correct model, parameter values should be insensitive to the size of the parameter space and the particular priors invoked.

Table 1.1 gives an overview of the present values of some of the different parameters in Section 1.8.2. How the different parameters affect the power spectrum will be discussed in Section 2.3.1.

1.9 CMB experiments

Since the first detection in 1964, the CMB radiation has been measured by a number of experiments, covering the frequency rage from 1 to 500 GHz. The majority of the first experiments focused on determining the average radiation temperature and the precise Planck spectrum. As theoretical progress made it clear that extremely valuable information about the fundamental properties and the evolution of the Universe lay hidden in the CMB anisotropies, focus was shifted towards detecting these anisotropies.

Parameters	Mean and 68% Confidence Errors
Ω_b	0.044 ± 0.004
Ω_m	0.27 ± 0.04
h	$0.71^{+0.04}_{-0.03}$
n_s	0.93 ± 0.03
z_r	17 ± 4
r_s	147 ± 2 Mpc

Table 1.1: Some basic and derived cosmological parameters. The parameters are fitted to the WMAP, CBI, ACBAR, 2dFGRS and Lyman α forest data. The table is a edited version of Table 10 in Spergel (2003).

It soon became clear that new and improved technology was needed in order to succeed in gaining this information. And after years of hard work, measurements of the anisotropies were finally achieved by the COBE satellite in 1990. However, there is still need for improvement, particularly concerning resolution and sensitivity, and this is the primary goal of several upcoming CMB missions.

Present and future CMB experiments will be able to reach the required angular resolution, sensitivity, sky coverage and reduction of systematic effects to probe the acoustic features in the CMB spectrum. With this kind of sensitivity, most of the cosmological parameters of near scale-invariant adiabatic models can be fit to the level of a few percent (see *e.g.* Jungman et al., 1996).

Most of this Section is based on the official home-pages of COBE[1], BOOMERanG[2], MAXIMA[3], WMAP[4] and Planck[5].

1.9.1 COBE

The COBE (COsmic Background Explorer) satellite was launched in 1989 with two distinct aims: to measure the CMB radiation temperature to a very high accuracy, and to try to detect the anisotropies of the CMB radiation field.

In order to achieve the first aim, a polarising Michelson interferometer (FIRAS) was used. FIRAS detected an almost perfect blackbody radiation at a temperature of 2.725 ± 0.010K, with less than one part in 10^4 deviation (Hu, 1995). This is the smallest deviation from a Planck spectrum ever measured, and made a perfect match with the theoretical expectations. Figure 1.3 shows the Planck spectrum measured by FIRAS.

The second set of measurements were a lot more difficult to achieve. Prior to COBE, all instruments used in the search for such anisotropies had failed to detect any up to the level of 10^{-4} Kelvin. On-board COBE there was an instrument called DMR, consisting of six differential microwave radiometers with two nearly independent

[1] <URL: http://space.gsfc.nasa.gov/astro/cobe/cobe_home.html>
[2] <URL: http://cmb.PHYS.cwru.edu/boomerang/>
[3] <URL: http://cosmology.berkeley.edu/group/cmb/>
[4] <URL: http://map.gsfc.nasa.gov/>
[5] <URL: http://astro.estec.esa.nl/Planck/>

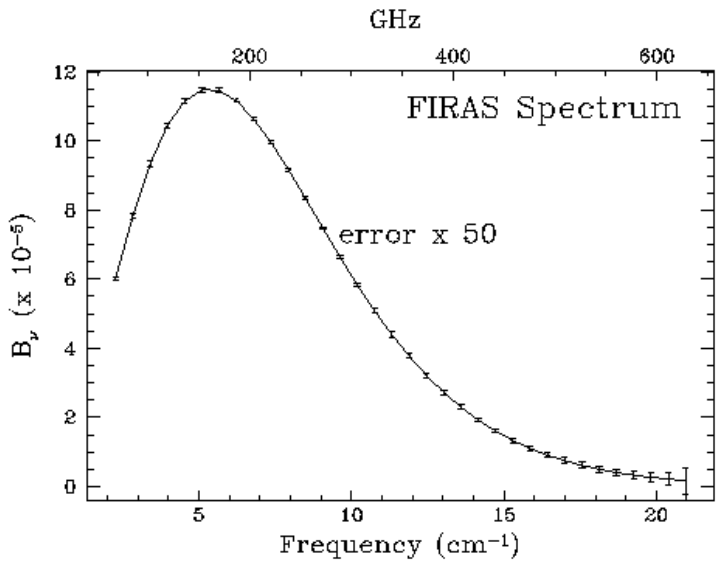

Figure 1.3: Within the precision of the FIRAS instrument on board the COBE satellite, the Planck spectrum of the CMB is as perfect blackbody spectrum with a maximum deviation of $3 \cdot 10^{-4}$. No spectral distortion have been measured to date excluding nearly all options for its formation except in the early stages of a Hot Big Bang. The intensity is plotted in ergs $\mathrm{cm}^{-2}\ \mathrm{s}^{-1}\ \mathrm{sr}^{-1}$ cm. Reprinted from (Hu, 1995).

channels, each operating at 31.5, 53 and 90 GHz. The DMR aperture was designed to detect differences in temperature as small as 10^{-5} degrees Kelvin, a sensitivity which proved to be high enough to finally prove the existence of anisotropies in the CMB. The dipole was discovered after just a few months of observations, and when analysing the completed data sets, the presence of even smaller temperature variations were confirmed.

The sky maps that COBE produced (see Figure 1.4) consist of only 6144 pixels (Bennett, 2003a). It was not possible to detect any individual structures in the CMB radiation because of the low resolution, neither was it possible to measure multipoles up to the full resolution ($l \sim 20$). It was, however, possible to find an almost perfect power spectrum up to a multipole value of $l = 10$, corresponding to a resolution of 20 degrees.

For more information on COBE, see the mission's official home-page:
<URL: http://space.gsfc.nasa.gov/astro/cobe/cobe_home.html>.

1.9.2 MAXIMA and BOOMERanG

Detector technology has developed immensely since COBE was built in the 1980s, but the costs of a new satellite mission was long considered to be too expensive. The

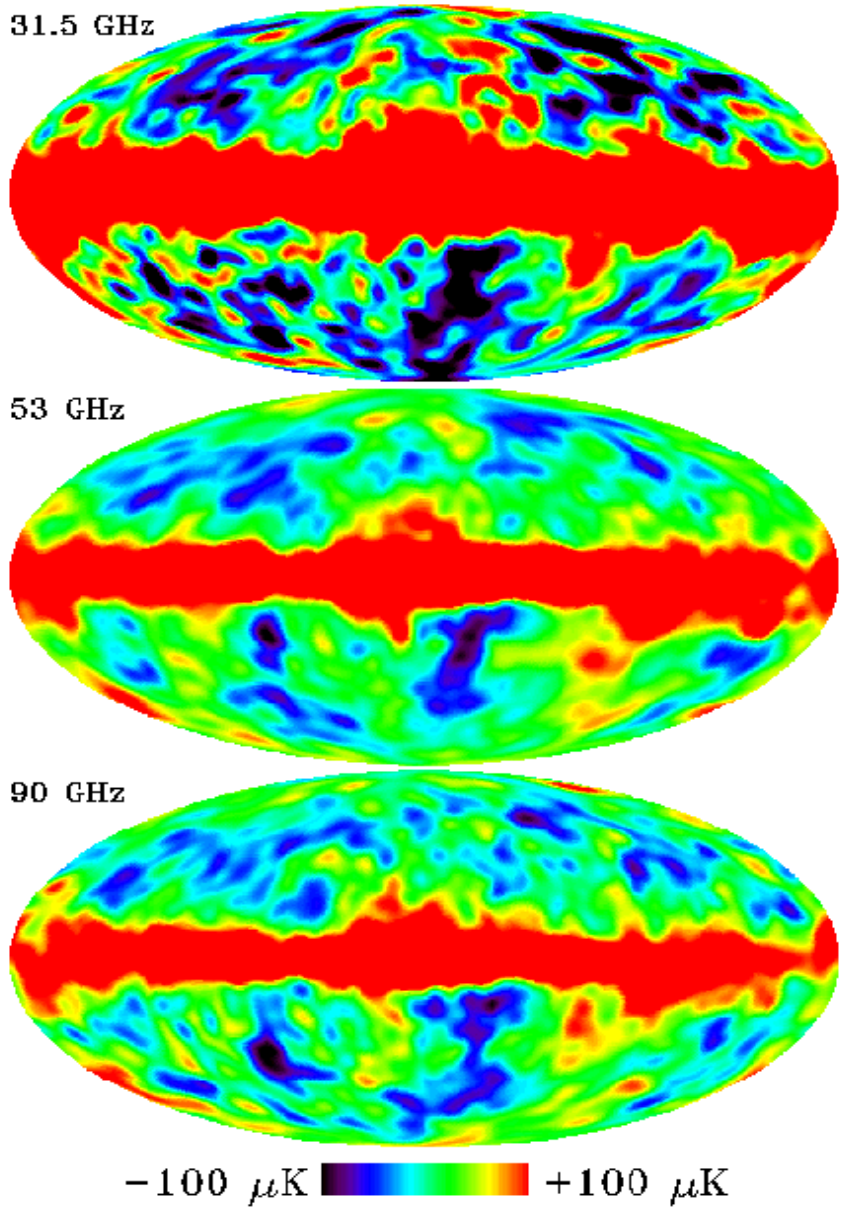

Figure 1.4: The complete microwave sky temperature maps obtained from each of the three COBE DMR frequencies - 31.5, 53, and 90 GHz - following dipole subtraction. The broad, red band at the centre of each sky map is the Milky Way. Reprint of <URL:http://space.gsfc.nasa.gov/astro/cobe/dmr_smooth_sum_maps.gif>.

solution became to send balloons up over the lower atmosphere.

MAXIMA 1, the first balloon of the MAXIMA (Millimeter Anisotropy eXperiment IMaging Array) project, was launched in Texas, USA August 1998. This was the first of two successive balloon flights of the project. MAXIMA 1 flew for three hours at an altitude of 36 kilometres, and had a sky coverage of 124 square degrees. MAXIMA 2 was launched June 1999, flew for twelve hours at an altitude of 41 kilometres and had roughly twice the sky coverage of MAXIMA 1.

Between the two balloon flights of the MAXIMA project, another balloon experiment was initiated. BOOMERanG (Balloon Observations Of Millimetric Extragalactic Radiation and Geophysics) was launched from Antarctica on December 29, 1998, and flew for ten days at an altitude of 37 kilometres. The Antarctic was chosen to be the best suited location for this long-duration flight because of the low infrared atmospheric radiation in the cold polar areas. The favourable temperature conditions and the high angular resolutions made it possible to detect fluctuations on angular scales between 0.3 and 3.6 degrees.

The results from the two balloon-born experiments were released in the spring of 2000 (Mauskopf, 2000; Winant, 2000), and the data from the two experiments were found to be consistent up to calibration uncertainties. The data showed a large peak in the power spectrum centred around $l = 200$, clearly delineated and providing good evidence that the Universe is spatially flat, *i.e.* $\Omega = 1$ (see Figure 1.6).

Earlier data from the previous year (Miller, 1999) had clearly demonstrated the existence and angular scale of the first peak in the power spectrum and produced the first maps of the CMB at angular scales below a degree.

One of the most recent balloon-borne experiments is Archeops. This experiment is designed to obtain large sky coverage in a single flight, using Planck HFI technology. Archeops provides the scientific community with the highest noise-to-signal ratio mapping of the first acoustic peak and its low-l side, and also covers the largest multipole range, to date. Results from the flight made February 7, 2002, show CMB signals with a clear peak at $l \simeq 200$, consistent with inflationary-motivated cosmological models and with previous CMB experiments (Benoît, 2003).

1.9.3 Ground-based missions

The balloon-born experiments of MAXIMA and BOOMERanG were soon followed by several ground-based experiments. In December 2000, The DASI (Degree Angular Spectroscopic Interferometer) group released their first measurements made at the Amundsen-Scott South Pole station during December 1999 and January 2000 (Carlstrom and DASI Collaboration, 2000).

The results from the DASI group were confirmed in 2001 by another ground-based interferometry experiment called the Cosmic Background Imager (CBI), and the com-

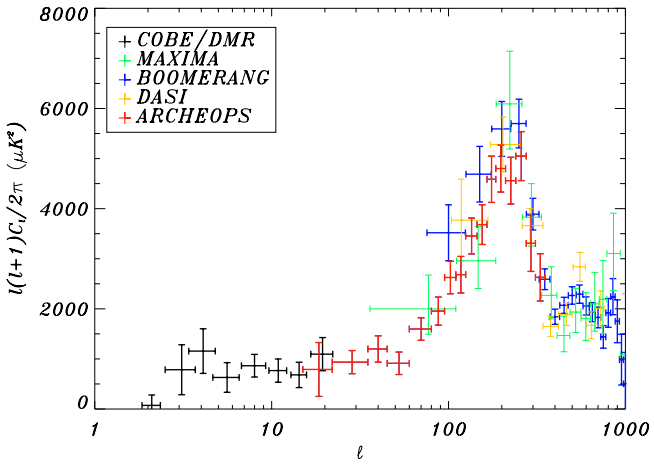

Figure 1.5: The Archeops power spectrum compared with the results of COBE, BOOMERanG, DASI and MAXIMA. Reprinted from (Benoît, 2003).

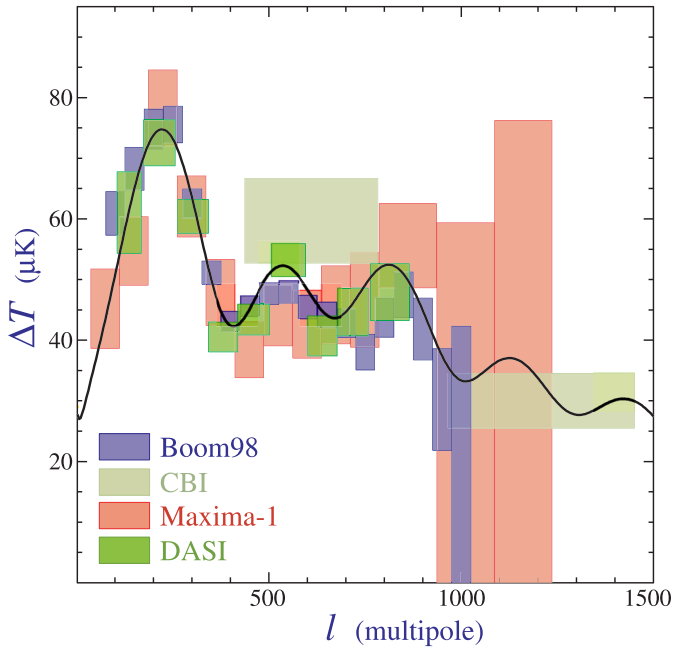

Figure 1.6: The angular power spectrum from MAXIMA, BOOMERanG, CBI and DASI. The power spectrum is the best fit to the combined results of the MAXIMA, BOOMERanG, CBI and DASI experiments. The boxes illustrates measurements and uncertainties in the different experiments. Reprinted from <URL:http://background.uchicago.edu/~whu/physics/tour.html>.

bined data from the balloon-born and the ground-based experiments let the scientists see the third peak of the power spectrum for the first time (see Figure 1.6).

The VSA (Very Small Array) is the latest ground-based experiment. The VSA is an interferometer designed to study CMB anisotropies on angular scales of 2.4 - 0.2 degrees on the sky, corresponding to multipole values of $l = 150 - 1800$. The telescope has been making observations of CMB fields since September 2000, and the latest results were released in December 2002 (Grainge, 2002).

1.9.4 The WMAP satellite

In June 2001 NASA launched the Wilkinson Microwave Anisotropy Probe (WMAP) satellite. This is the first satellite to use the virtual point in space called the 2nd Lagrangian point (L2) of the Sun-Earth system, an unstable equilibrium position 1.5 million km from Earth in the direction opposite the Sun, as its permanent observing station. The satellite measures the CMB temperatures accurately over the complete sky, with high angular resolution and sensitivity. The aim is to be able to measure the relative CMB fluctuations with an angular resolution of 0.3 degrees or better, a sensitivity of 20μ K per 0.3 degree square pixel and with systematic effects limited to $5\mu K$ per pixel.

In October 2002, the satellite completed its two first full sky observations. The first sky maps and scientific results were released in February 2003. The resulting power spectra put strong constraints on several cosmological parameters simultaneously, ruled out many variants of cosmological models and put significant pressure on the models outlined in Section 1.8.1 (Hinshaw, 2003; Page, 2003).

More information about WMAP can be found on the mission's official home-page: `URL: http://map.gsfc.nasa.gov/`.

1.9.5 Planck

The most promising of the upcoming CMB experiments is ESA's (European Space Agency) Planck satellite mission. The Planck satellite is to be launched in 2007 together with Herschel, ESA's next infrared and submillimetre space observatory, and will operate in an orbit close to the L2 point of the Sun-Earth system. Once in orbit, the Planck satellite has a lifetime expectancy of 1.5 years, and during this time the satellite will map the CMB sky twice at all angular scales larger than $10''$ with significantly better resolution and sensitivity than the WMAP mission. The goal is to determine the CMB fluctuations to an accuracy of a few parts in 10^6. The satellite will also map nearly all major galactic and extra-galactic sources of microwave emission, and is expected to detect thousands of new extra-galactic microwave sources in so far poorly observed frequency ranges.

The instruments on-board the satellite will consist of a telescope with a primary mirror of 1.5 meters, and a payload which consists of two arrays of highly sensitive detectors called the Low Frequency Instrument (LFI) and the High Frequency Instrument

(HFI).

The LFI instrument is an array of 56 tuned radio receivers operating at a temperature of 20 K. These receivers are based on so-called High Electron Mobility Transistor technology, where the incoming signal is amplified and then converted into voltage, and will be grouped into three frequency channels centred between 30 and 70 GHz.

The HFI instrument is an array of 48 bolometric detectors, which work by converting radiation into heat. This heat is then measured by a highly sensitive thermometer, which in turn is read out and converted into real temperatures in a on-board computer. The detectors will work in six different frequency channels centred between 100 and 857 GHz, and operate at a temperature of 0.1 K. To achieve such an extremely low temperature, several complex refrigerators are used on-board the satellite.

The two instruments are designed and built by each their consortium of more than 20 scientific institutes.

The Planck sky maps will use HEALPix pixelisation with $\sim 10^7$ ($12 \cdot 1024^2$) pixels, almost a factor of 10^4 more than that of the COBE experiment. The primary scientific target of the Planck mission is to measure an accurate power spectrum up to a multipole value of $l \sim 1000$. Because of foregrounds and noise, it is highly likely that this is the physical limit for what we can achieve, even if we had infinite resolution.

If Planck fulfils its potential, the mission will provide estimates of all cosmological parameters to an accuracy of a few percent.

More information about the Planck mission can be found on
`URL: http://astro.estec.esa.nl/Planck/`.

1.10 Computational tools

As mentioned in Section 1.1, in the past, cosmology was a science where detailed observations were rare, and data analysis easily manageable. Today data are streaming in from satellite missions and other experiments, and computers have become an indispensable tool in the data analysis. But the next generation of CMB experiments will produce such large amounts of observational data that straightforward analysis will be impossible with the methods in use today. New and more efficient approaches are therefore vital.

There have been suggested several new and improved computational tools for working with power spectra and CMB maps theoretically, analytically and numerically, but so far there are only two that are widely accepted within the scientific society, CMBFAST and HEALPix. Most of this chapter is based on Górski et al. (2000), Eriksen (2002) and information found on the official home-pages of CMBFAST and HEALPix.

1.10.1 CMBFAST

CMBFAST is a computer algorithm that generates power spectra based on different cosmological models. The algorithm was first developed in 1996 by U.Seljak and M.

Zaldarriaga, (Seljak and Zaldarriaga, 1996) and has later been revised several times.

The power spectra computed with the CMBFAST are based on integration over the sources along the photon past light cone. The integral is divided into a time integral over a geometrical term and a source term.

The source term is model dependent and can be expressed in terms of photon, baryon and metric perturbations using a small number of differential equations. Because the source term is a slowly varying function, it only needs to be evaluated in a small number of points. The geometrical term is a fast varying function and needs to be evaluated in a large number of points. But since this term does not depend on the particular cosmological model, it can be computed separately.

This split of the integral allows a significant reduction in the computational time compared to standard methods, and is what makes the algorithm superior to competing algorithms.

The CMBFAST algorithm is publicly available at `URL:http://www.cmbfast.org/`, and also at `URL:http://ascl.net/cmbfast.html`.

1.10.2 The HEALPix package

When using computers in data analysis, the information has to be discretised in one way or another. How we choose to do this depends on what kind of analysis we wish to perform.

When working on the sphere, HEALPix is one way of dividing the sphere into discrete pixels. HEALPix is short for 'Hierarchical, Equal Area, isoLatitude Pixelisation', and as the name implies, has three main features built into the pixelisation:

1. All pixels are organised in an hierarchical system with respect to resolution.
2. All pixels have equal area.
3. The pixel centres lie on rings of constant latitude.

The first feature enables fast nearest-neighbour searches, the second enables fast numerical integration on the sphere, and the third feature is necessary if we want to apply the Fast Fourier Transform to our maps. This last property will become extremely valuable for the analysis of the mega-pixel CMB maps from missions like WMAP and Planck.

As of today HEALPix is the only pixelisation scheme which has been able to incorporate all the three features mentioned above. Since HEALPix further comes with with a set of mature implementations of both basic algorithms and a also number of special-purpose programs, it is probably the strongest available candidate for a standard pixelisation scheme at the moment, and for these reasons it has also been chosen to be the official pixelisation for both the WMAP and the Planck missions. Several other pixelisations have been suggested during the last years, and there are still others under development. The strongest competitor is probably Igloo, developed by a Cambridge-based team led by Crittenden and Turok. But the corresponding software is not as

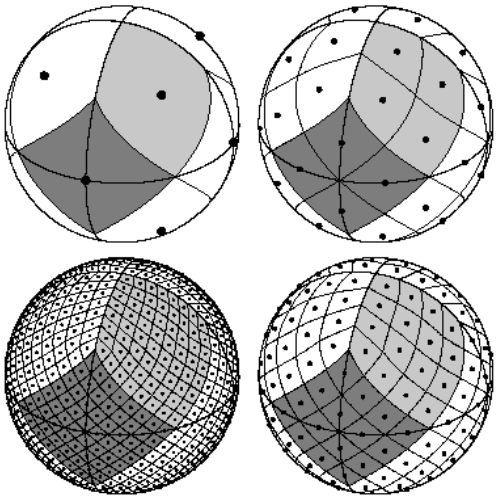

Figure 1.7: View of the HEALPix partition of the sphere. Overplot of equator and meridians illustrates the octahedral symmetry of HEALPix. Light-grey shading shows one of the eight (four north and four south) identical polar base-resolution pixels. Dark-grey shading shows one of the four identical equatorial base-resolutions.The different panels show how each of the base-resolution pixels can be divided into smaller pixels, thus increasing the resolution. Reprinted from (Górski et al., 2000).

refined, and as a result it has not yet been able to establish itself as a widespread standard.

Let us take a closer look at how HEALPix actually divides the sphere into pixels. First the sphere is divided into 12 base pixels of equal area, as shown in the upper left panel of Figure 1.7. Note that these base pixels all lie on tree rings of constant latitude.

If we want to increase the resolution, each existing pixel is dived into four new pixels, and the process is repeated until the desired resolution is obtained. The pixel division process is illustrated in Figure 1.7.

The HEALPix software is divided into three parts:

1. A library of general-purpose routines.
2. Six special-purpose Fortran 90 programs.
3. Several IDL-utilities.

The most important special-purpose Fortran 90 programs for this thesis is without doubt **synfast**. This program reads a user-defined power spectrum, C_l, and returns a Gaussian realization based on that spectrum. The underlying method is quite straightforward; for each spherical harmonic coefficient a_{lm} **synfast** draws a random complex

number from a two-dimensional Gaussian distribution with vanishing mean and variance given by C_l. Then it sums up all the individual terms for each pixel according to the formula

$$\frac{\Delta T}{T} = \sum_{lm} a_{lm} W_l Y_{lm}(\Omega). \tag{1.10}$$

Here W_l is a Gaussian window function of user defined FWHM (full width, half maximum), and Y_{lm} is the spherical harmonic at the given solid angle $\Omega = (\phi, \theta)$.

The **anafast** utility is another useful program provided by the HEALPix package. This program returns the power spectrum C_l from a pixelized map, using Fast Fourier Transforms.
Other programs included in the HEALPix software package are **hotspot** (which finds the maxima and minima of a HEALPix map), **map2gif** (which produces a gif-image from a map), **smoothing** (which convolves a map with a Gaussian beam) and **udgrade** (which translates a map from one N_{side} to another, using either averages or interpolation).

The complete HEALPix package can be obtained by sending an email to K. M. Górski (kgorski@eso.org). For more information about the HEALPix, see the official HEALPix site: `<URL: http://www.eso.org/science/healpix/>`.

1.10.3 H.K. Eriksen's Correlation Suite

The Correlations Suite was created by Hans Kristian Eriksen in 2002 as part of his master thesis (Eriksen, 2002). The Suite consists of about 20 programs, divided into two main sub-menus, **correlations.pl** and **analysis.pl**, for use in calculations and analysis of different types of correlations functions and power spectra. I will only give a brief description of the three programs from the Correlation Suite that I have used in my thesis:

genmask:	generates a suitable mask for the k-block structure.
structures:	creates the initial structure of k-blocks.
twopt_calc_element:	calculates a given bin of the two-point correlation function from the given structure and mapinfo files.

The mapinfo file contains the N_{side} value of the maps, the number of map files and a list of all the filenames. All information needed to compute a given bin is contained in the corresponding k-block.

A more thorough description of the Correlation Suite can be found in Hans Kristian Eriksen's master thesis.

Chapter 2

The power spectrum and the two-point correlation function

In this chapter I give an introduction to the statistics of the CMB. Then I define the angular power spectrum C_l, and review how it is affected by the different cosmological parameters from Section 1.8.2, before I review the mathematical connection between the power spectrum and the angular two-point correlation function.

2.1 Statistics

Statistics, and particularly the theory of random fields, is a very useful tool in CMB analysis. Any given cosmological theory will predict an underlying distribution of the fluctuations in the CMB. The fluctuations are assumed to arise from some random statistical process, and the exact pattern of fluctuations we observe on the sky is only one single realization of this process. But we are not interested in the exact pattern of the realization, just in the underlying statistics. So in this section I will give a brief introduction to some basic statistical concepts commonly encountered in cosmology, with weight on two of the most basic statistical properties that describes fluctuations: the angular temperature power spectrum and its equivalent, the two-point correlation function.

Statistical properties are often presented through Fourier representation. But since we observe the CMB as a two-dimensional temperature distribution on the sky, *i.e.* on a sphere, it is more common to present the CMB temperature observations through spherical harmonics. Thus I have tried to use this representation consistently throughout my thesis.

Most of this introduction is based on Tegmark (1995) and Watts and Coles (2003).

2.1.1 Random fields

A random field is a realization of a stochastic process and is rigorously defined in terms of the joint probability distribution of its values at any n points, $n = 1, 2, 3, \ldots$ Hence,

a random field δ is defined by specifying all the n-dimensional probability distributions of $[\delta(\mathbf{x_1}), \ldots, \delta(\mathbf{x_n})]$ for $\mathbf{x_1}, [\mathbf{x_1}, \mathbf{x_2}]$, *etc.* In CMB applications density perturbations $\delta\rho/\rho$, velocity perturbations $\delta\mathbf{v}$ and gravitational potential perturbations $\delta\phi$ represent three such random fields on the celestial sphere at last scattering. In this thesis I will mainly be concerned with the measured temperature field, T.

Gaussian random fields

In most popular models for origin of cosmic structure, particularly those involving cosmic inflation, the initial fluctuations form a Gaussian random field, which are the simplest of all random fields.

One of the most important properties of Gaussian fields is that they are completely described by their second-order statistics, like the angular power spectrum C_l or the two-point correlation function $C(\chi)$. This makes analysis of Gaussian fields relatively straightforward, because their statistical properties are fixed once the two-point correlation function, or equivalently the power spectrum, is determined.

If the hypothesis of primordial Gaussianity is correct, then the cosmological density fields began with random phases. As the Universe evolved, perturbations grew in mass and generated non-linear, non-random phases that contain much information about the spatial patterns of the fluctuations.

Homogeneity and isotropy

The formal definition of strict statistical homogeneity for a random field is that the joint probability distributions must be invariant under spatial translations for any $\mathbf{r}$ and for all orders. For a Gaussian field to be strictly homogeneous it is a necessary and sufficient condition that the correlation function $C(\mathbf{r}) = \langle f(\mathbf{r_1}) f(\mathbf{r_2}) \rangle$, where $\mathbf{r}$ is the distance between $\mathbf{r_1}$ and $\mathbf{r_2}$, is a function of the scalar quantity $r \equiv |\mathbf{r_1} - \mathbf{r_2}|$ only. By requiring rotational invariance, the fields also becomes statistically isotropic.

All standard cosmologies are based on the Cosmological Principle, which states that at any given cosmological time the Universe is homogeneous and isotropic on large scales. Thus, in cosmology the random fields are always assumed to be homogeneous and isotropic, and hence the 1-point distribution is independent of $\mathbf{r_1}$ and the 2-point distribution only depend on r, *i.e.* $\langle f(\mathbf{r_1}) \rangle = 0$ and $C(\mathbf{r}) = C(r)$. So if the temperature perturbations are well approximated as a homogeneous and isotropic Gaussian random field, as CMB maps so far suggests, then C_l and $C(\chi)$ contain all statistical information about the temperature distribution.

2.2 The two-point correlation function

The statistical properties of the 3-dimensional fluctuations causing the CMB are often presented through a Cartesian Fourier representation. But what we observe is the two-dimensional temperature distribution on the sky. Thus the usual approach to presenting the CMB temperature observations is through spherical harmonics.

When looking at the temperature fluctuations of the CMB, the two-point correlation function expresses the correlation between the temperature perturbations at two points $\Omega_i = (\theta_i, \phi_i)$ and $\Omega_j = (\theta_j, \phi_j)$ separated by an angle χ_{ij}.

In spherical coordinates the temperature fluctuations at a given point (Ω) on the celestial sphere are given by

$$\Delta T = \Delta T(\Omega) = T(\Omega) - \langle T \rangle, \tag{2.1}$$

where $T(\Omega)$ is the temperature at the point Ω, and $\langle T \rangle$ is the mean temperature of the Universe.

In this context, the two-point correlation function is defined as

$$C(\chi_{ij}) = \langle \Delta T_i \Delta T_j \rangle. \tag{2.2}$$

When estimating the two-point correlation function from observations, the angle brackets represent the average taken over the observed sky. Estimating the two-point correlation function from theoretical simulations, the angle brackets represent the average taken over the ensemble.

The correlation function is related to the probability distribution of ΔT: if the fluctuations form a Gaussian random field then the probability distributions of ΔT_i, $\langle \Delta T_i \Delta T_j \rangle$, are χ^2-distributed with $2l+1$ degrees of freedom. For high enough l ($l \geq 20$), $\langle \Delta T_i \Delta T_j \rangle$ will be very close to Gaussian (see Section 5.3).

I have chosen to limit my work to the two-point correlation function, but there also exist higher-order correlation functions. These contain information about the statistical distribution and large scale structures, amongst others. For more information on higher order correlation functions, see *e.g.* Eriksen (2002) or Eriksen et al. (2002).

The mathematical relation between the power spectrum and the angular two-point correlation function will be reviewed in Section 2.4.

2.3 The power spectrum

The angular temperature power spectrum C_l reflects the fluctuation power at a given angular scale. In other words, the angular temperature power spectrum tells us what the amplitude of the CMB fluctuations is that have a given angular extension on the sky. Figure 1.2 shows a typical power spectrum for a CDM universe model.

In spherical harmonic representation the expansion of the fluctuations over the sky can be written as

$$\boxed{\frac{\Delta T}{T}(\Omega) = \sum_{l=0}^{\infty} \sum_{m=-l}^{m=l} a_{lm} Y_{lm}(\Omega),} \tag{2.3}$$

where a_{lm} are the temperature multipole, or spherical harmonic, coefficients.

In this representation the angular power spectrum is defined as

$$\boxed{C_l \equiv \frac{1}{2l+1}\sum_m \langle \mid a_{lm} \mid^2 \rangle \ .} \tag{2.4}$$

The angle brackets represent averaging over all realization, but as we only can observe the Universe we live in, we only have **one** realization to observe. This apparently unsolvable problem is solved by invoking the *fair sample hypothesis*, which states that averages over finite sky patches of the Universe can be treated as averages over some probability ensemble.

However, there is one problem we cannot get around: the low l modes in Equation 2.4 have only a small number of independent spherical harmonic coefficients, a_{lm}, so that estimates of the angular power spectrum at low l are uncertain even if the whole sky is available. Since there is nothing that can be done to improve this uncertainty, this is an irreducible source of uncertainty, which is why it is called *'cosmic' variance*.

The first experimentally determined power spectrum was presented to the scientific community when the first results from the COBE DMR instrument were published in 1992 (Smoot, 1992).

As the sensitivity of the CMB experiments constantly improves, the information in the higher peaks is uncovered, providing us with a more accurate measurement of the different parameters, and hence the assumptions made about the underlying model can be relaxed. With the latest data from WMAP we seem to have a definite measurement of the first acoustic peak at $l = 220$ and a second peak at $l \sim 540$. Evidence also points towards the existence of a third peak at $l \sim 800$ (Hinshaw, 2003). Hence the most interesting power spectrum feature to focus on in upcoming experiments like Planck will be to confirm the third peak, the possible detection of any higher orders and the accurate measurements of the positions and amplitudes of all peaks and troughs.

2.3.1 The power spectrum and the cosmological parameters

As pointed out earlier, the CMB offers a completely independent method of determining the classical cosmological parameters with comparable or significantly higher accuracy than any other observations and has fewer astrophysical systematic effects to worry about. One of the main reasons why the CMB has generated such excitement is that it contains enough information to constrain numerous parameters simultaneously. But these exciting possibilities only hold if the Universe is accurately represented by a model (see 1.8.1). Though, when simultaneously using totally different methods (*e.g.* clustering of galaxies, supernova luminosity relations *etc.*) to constrain degeneracies among parameters, very accurate estimates can in principle be found.

Given a set of power spectrum data, we want to know two pieces of information about the cosmological parameters:

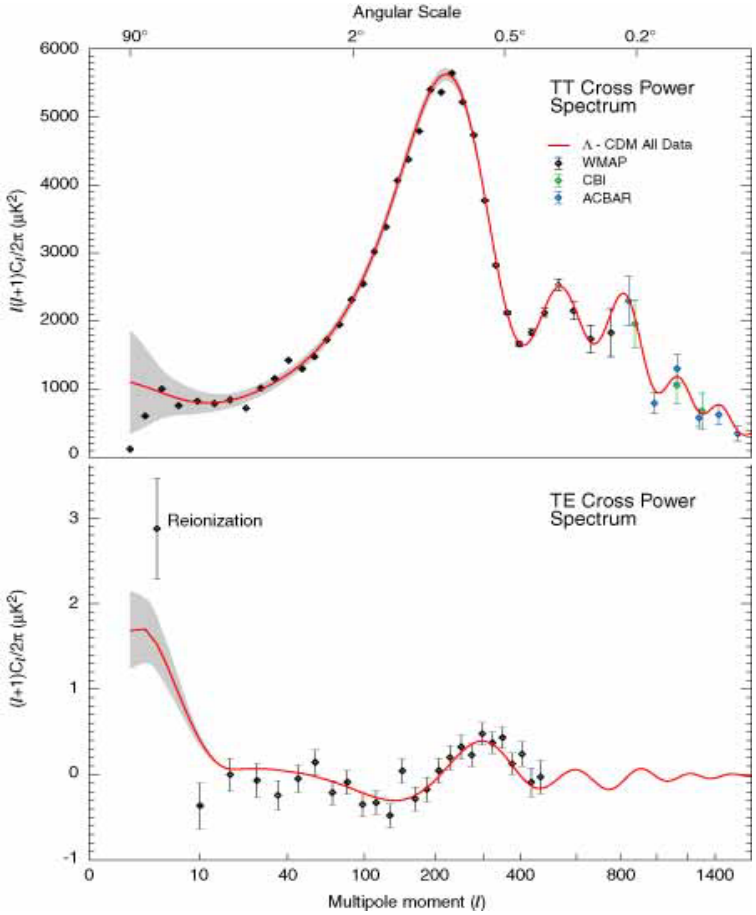

Figure 2.1: The WMAP angular power spectrum. The upper panel shows the WMAP temperature (TT) angular power spectrum. The WMAP temperature results are consistent with the ACBAR and CBI measurements, as shown. The TT angular power spectrum is now highly constrained. The best fit running index ΛCDM model is shown. The grey band represents the cosmic variance expected for that model. The WMAP temperature-polarisation (TE) cross-power spectrum is shown in the lower panel. Reprinted from Page (2003).

(1) What parameter values provide the best-fit model?

(2) What are the error-bars on these parameters?

I will not go much into details on the error-bars here.

The features in the CMB power spectrum depend on various physical quantities which can be expressed in terms of combinations of the cosmological parameters presented in Section 1.8.2. Examples of such quantities are the baryon density $\Omega_b h^2$, the total matter density $\Omega_0 h^2$, the dark energy density Ω_Λ and curvature $\Omega_k = 1 - \Omega_0 - \Omega_\Lambda$. Once we know how these quantities behave in various models, we will be able to retrieve accurate information on cosmological parameters from the power spectrum, as well as on the physical scales associated with the formation of primary and secondary anisotropies, matter-radiation equality, Silk damping and other mechanisms present in the early Universe.

Curvature, Ω_k

In his famous theory of general relativity, Einstein found that curvature of space-time is equivalent to gravity and hence can be used as a measure of the amount of matter in the Universe.

In practice the curvature of the Universe is measured by the size of the temperature anisotropies in the CMB. The anisotropies appear at harmonics of the sound horizon, which is a fixed physical scale at last scattering, the angular scale that these features subtend on the sky gives a precise measure of the curvature of the Universe. Since the natural period of the fluctuations sets the separation between the peaks in models where the variations in the gravitational potential is slow compared to the natural frequency of the oscillations, the spacing between the peaks in the power spectrum provides the most robust test of the curvature (Hu and White, 1996).

Spatial curvature was irrelevant before recombination, *i.e.* when the fluctuations in the CMB was created, thus changing the curvature does not effect the shape of the power spectrum, it merely shift the peaks sideways. But conversion from physical scales into angular scales depends strongly on how space is curved. Negative curvature (*i.e.* positive Ω_k) decreases the angle that a feature subtends on the sky and hence shifts the peaks to towards higher l. Positive curvature (*i.e.* negative Ω_k) makes the peaks shift towards lower l. The dependence of the power spectrum on the curvature can be seen in Figure 2.2.

So far I have only considered effects that arise purely from the last scattering surface, where the presence of the curvature merely scale the features in angular or multipole space. But foregrounds such as the ISW is also affected by the curvature, because in addition to shifting the peaks sideways, curvature also cause the fluctuations in the gravitational field to decrease over time, so that photons passing a potential well will have an excess blueshift after climbing out of the well. This is the late ISW effect

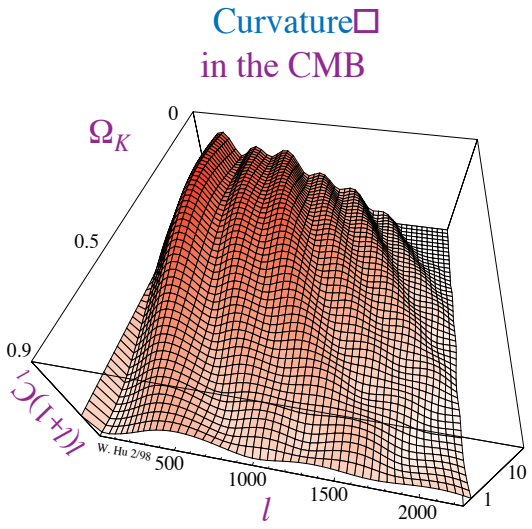

Figure 2.2: The Ω_k-dependence of the power spectrum. Changing the curvature Ω_k shifts the peaks sideways, but does not effect the shape of the power spectrum. A decrease in curvature shifts the peaks to towards higher l, while an increase in curvature makes the peaks shift towards lower l.
Reprinted from <URL: http://background.uchicago.edu/~whu/metaanim.html>.

described in Section 1.6.1, and shows up as an increase in power at large scales, *i.e.* small l.

Changing the curvature, keeping Ω_Λ and all the other matter densities fixed, the Hubble parameter h will also change, since there exists a degeneracy between some of the parameters.

Matter density, $\Omega_0 h^2$

Because the gravitational potentials in the CMB only grows during the radiation dominated era, and $\Omega_0 h^2$ solely determine the time of matter-radiation equality, then the matter density determines the size of the ISW effects, i.e. the amount of potential decay due to radiation pressure inside the horizon during radiation domination. This decay boosts the acoustic peaks, so lowering h and keeping Ω_0 constant will increase this boost by delaying the matter-radiation equality. By changing the expansion rate, this will also shift the peaks somewhat. How changes in the Hubble parameter affects the power spectrum when Ω_0 is fixed, can be seen in the Figure 2.3.

$\Omega_0 h^2$ also affects the size of the dark matter fluctuations, since dark matter starts to collapse gravitationally only after matter-radiation equality.

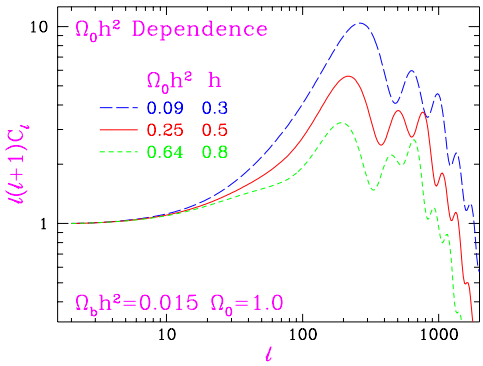

Figure 2.3: The dependence of the power spectrum on the Hubble parameter h. Lowering h and keeping Ω_0 constant boosts the acoustic peaks, but also shift the peaks towards higher l's. Reprinted from <URL: http://background.uchicago.edu/~whu/metaanim.html>.

Baryon density, $\Omega_b h^2$

The baryon density creates a distinct signature in the acoustic oscillations (Hu and Sugiyama, 1996). If the oscillations in the photon-baryon fluid were effectively about the mean temperature, they would be of the same amplitude, and the peaks of the power spectrum would all have the same height. Without baryons there would be no acoustic oscillations, so naturally the peaks get higher as the baryon density increases. But if the baryons contributed a significant mass, then the zero-point of the oscillations would be displaced, and the odd-numbered peaks, *i.e.* the peaks in the power spectrum arising from the positive oscillations, would get boosted more than the even-numbered peaks, *i.e.* the peaks arising from the negative oscillations. The physical interpretation of this effect is that, as baryon density increases, the potential wells deepened and the plasma within the wells became increasingly compressed. This alternating peak height signature is a distinctive signature of baryon mass, and helps distinguish baryons from cold dark matter. Measurement of the heights of the first acoustic peaks thus allows a precise determination of the cosmological baryon density.

The dependence of the power spectrum on the baryon density can be seen in Figure 2.4.

Dark energy density, Ω_Λ

Like curvature, the cosmological constant Λ was irrelevant at the time of recombination, so changing Ω_Λ does not alter the shape of the power spectrum, it merely shifts the peaks sideways. This is analogous to increasing the curvature, but the shift goes in the opposite direction. Because of the parameter degeneracy, the Hubble parameter h is changed as well, causing a shift, though not as strong as the shift caused by the alterations in the cosmological constant.

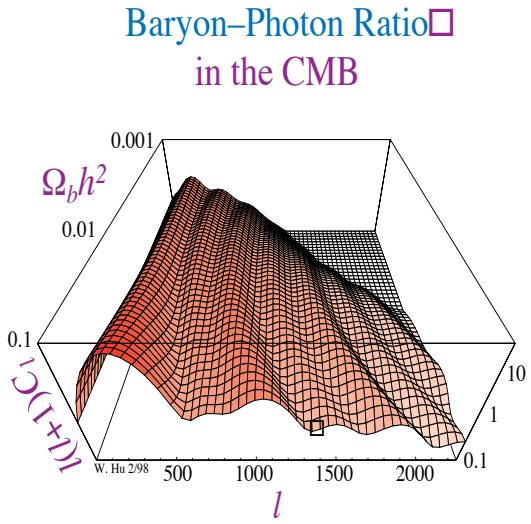

Figure 2.4: The Ω_b-dependence of the power spectrum. Increasing the baryon density boosts the peaks in the power spectrum. Note that the odd-numbered peaks is boosted more than the even-numbered peaks.
Reprinted from <URL: http://background.uchicago.edu/~whu/metaanim.html>.

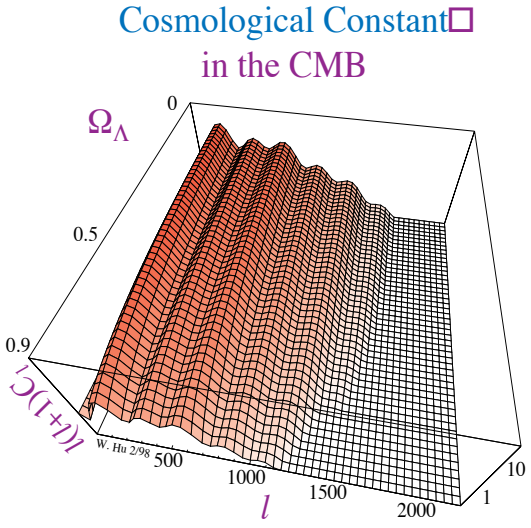

Figure 2.5: The dependence of the power spectrum on the cosmological constant Λ. Changing Ω_Λ shifts the peaks sideways, but does not change the shape of the power spectrum. Increasing the vacuum density, keeping the total density fixed, both lowers the peaks and shifts them towards higher l's.
Reprinted from <URL: http://background.uchicago.edu/~whu/metaanim.html>.

Keeping the total density fixed and increasing the vacuum density, reduces the baryon fraction of the Universe and lowers the peaks. Increasing the dark matter content of the Universe also pushes the time of matter-radiation equality further back in time, shifting the peaks of the power spectrum towards smaller scales, as well as sliding the power spectrum upwards.

In addition to shifting the peaks sideways, Λ also causes fluctuations in the gravitational field to decrease over time. Since these extra fluctuations in the photon temperature happen at late times (late ISW effect, see Section 1.6.1), they cause an increase in the power at large scales, *i.e.* to the left in the power spectrum.

The dependence of the power spectrum on the cosmological constant can be seen in Figure 2.5.

The spectral index, n_s

Changing the spectral index of the density fluctuations simply tilts the power spectrum, altering the ratio of small-scale to large-scale power. Increasing n_s will raise the right side of the spectrum relative to the left. This is especially visible in the low-l, Sachs-Wolfe region of the power spectrum.

If the perturbations were purely adiabatic, the power-law initial conditions are determined by the parameters Q, n_s and r_s from Section 1.8.2.

Neutrino species and neutrino masses

There have been made claims that the CMB should be able to constrain the effective number of neutrino species, N_ν. N_ν determines the radiation energy density of the Universe and thus modifies the time of matter-radiation equality, causing a boost in the power spectrum. This effect can be distinguished from a change in $\Omega_0 h^2$ because it affects other physical parameters differently than a shift in either Ω_0 or h. The radiation density is fixed by the current CMB temperature, known from COBE, as well as from the density of the neutrino backgrounds.

In principle the effect of neutrino masses, m_ν, can also be extracted from the CMB. Massive neutrinos have several small effects on the CMB, like slight increase in the sound horizon r_s at decoupling, increase in the monopole perturbations due to free streaming of massive neutrinos around the time of last scattering and a larger Sachs-Wolfe effect induced by the delay in matter-radiation equality. This will suppress the peaks in power spectrum.

Radiation velocities, Silk damping and reionization

In practice one also has to consider the contribution to the power spectrum from radiation velocities. This effect fills in the valleys between the power spectrum peaks. In addition, the amplitudes of the power spectrum peaks are suppressed by Silk damping. Early reionization will also suppress the power spectrum, but only at angular scales $l \ll 10$.

Parameter degeneracy

Note that not all of the parameters discussed above are independent. If Ω_b, Ω_0, h, and Λ are taken as independent parameters, there exists degenerate power spectra. Luckily, other observables not associated with CMB break the degeneracy, for instance the acceleration parameter q_0, which is measured directly by high-redshift supernova experiments.

There also exist other degeneracies in the temperature power spectrum: one between Q and r_s, and one between z_r and n_s. The first is illusory and the latter one will be lifted by the power spectrum of large-scale fluctuations, polarisation measurements and small-scale second-order temperature fluctuations.

Pixel noise, detector noise and beam width

Given a pixelized map of the CMB sky, one need to determine the contribution of pixelisation noise, detector noise and beam width to the multipole moments and power spectrum. Most current experiments oversample the sky with respect to their beam, so the pixelisation noise is negligible.

A map with pixels of a few arcminutes in size and a signal-to-noise ratio of around 1 per pixel can determine Ω_{tot}, $\Omega_0 h^2$, $\Omega_b h^2$, Ω_Λ, Q, n_s and z_r at a level of a few percent simultaneously, up to the degeneracy mentioned above (see Bond et al. 1998). Significant constraints can also be placed on r_s and N_ν.

The power spectrum and the correlations function

Having seen how the different parameters can be found from the power spectrum, it is not difficult to understand that a precise estimate of the power spectrum is important in order to find the correct model of the Universe. The power spectrum can be found directly from the maps of the observed CMB temperature fluctuations, and have become the standard way of presenting CMB results, particularly after advances in detector technology have lead to experiments with increasing sensitivity and hence larger data sets.

There is in principle no loss of information when calculating the power spectrum or the two-point correlation function, which is the real-space equivalent of the power spectrum, from pixel data. Hence calculating the power spectrum from the two-point function, should in principle not lead to any loss of information either. Thus in search of faster and more precise methods to determine the power spectrum from CMB sky maps, it could be that the two-point correlation function is a useful intermediate step in the transition from pixels to power spectrum representation. And here we are at the very essence of this thesis, because this is precisely what I wish to examine.

2.4 The equations

In this section I will review some properties of the angular two-point correlation function.

2.4.1 C(χ), the angular two-point correlation function on the full sphere

The angular two-point correlation function is defined as

$$\boxed{C(\chi) \equiv \langle T(\mathbf{\Omega_1})T(\mathbf{\Omega_2})\rangle,} \tag{2.5}$$

where T is the temperature function at a given position $\Omega = (\theta, \phi)$, χ is the angle between the two directional unit vectors $\mathbf{\Omega_1}$ and $\mathbf{\Omega_2}$. Here $\langle\rangle$ represents the average over the sphere.

In principle one can also define the average as an average over an infinite ensemble of realizations and use that to study the statistical properties of the ensemble. But when using the correlation function on astrophysical problems, there is only one sky available, *i.e.* **one** realization. One can then invoke the "fair sample" hypothesis which states that the ensemble average should be equivalent to taking averages over large enough sample areas.

Expressing the average as an integral over the sphere, the angular two-point correlation function is

$$\boxed{C(\chi) \equiv \frac{\int\int T(\mathbf{\Omega_1})T(\mathbf{\Omega_2})\delta(\cos\chi - \cos\alpha_{12})d\mathbf{\Omega_1}d\mathbf{\Omega_2}}{\int\int \delta(\cos\chi - \cos\alpha_{12})d\mathbf{\Omega_1}d\mathbf{\Omega_2}}.} \tag{2.6}$$

The expression in the denominator comes from the normalisation of the angular correlation function over the sphere. The angle between $\mathbf{\Omega_1}$ and $\mathbf{\Omega_2}$ is in general given by

$$\cos\alpha_{12} = \cos\theta_1\cos\theta_2 + \sin\theta_1\sin\theta_2\cos(\phi_1 - \phi_2). \tag{2.7}$$

The first step is to show that the denominator in (2.6) equals $8\pi^2$. One starts by looking at the Kroenecker δ-function. This function can be expanded into a sum of Legendre polynomials,

$$\delta(\cos\chi - \cos\alpha_{12}) = \sum_{l=0}^{\infty} a_l P_l(\cos\alpha_{12}) = \sum_l a_l P_l(\cos\alpha_{12}), \tag{2.8}$$

using the convention that $\sum_l = \sum_{l=0}^{\infty}$.

By multiplying both sides of (2.8) by $P_{l'}(\cos\alpha_{12})$, integrating over α_{12} and using the orthogonality and normalisation relation for Legendre polynomials,

$$\int_{-1}^{1} P_l(x)P_{l'}(x)dx = \frac{2\delta_{l,l'}}{2l+1}, \tag{2.9}$$

one finds

$$P_{l'}(\cos\chi) = \sum_l a_l \frac{2\delta_{ll'}}{2l+1}. \tag{2.10}$$

From this one gets that the coefficient a_l is

$$a_l = \frac{2l+1}{2} P_l(\cos\chi). \tag{2.11}$$

Substituting (2.11) into (2.8), one sees that the Kroenecker δ can be expressed as

$$\delta(\cos\chi - \cos\alpha_{12}) = \sum_l \frac{2l+1}{2} P_l(\cos\chi)P_l(\cos\alpha_{12}). \tag{2.12}$$

The addition theorem for spherical harmonics says that, for two given direction unit vectors on the full sphere where the angle between them is given by equation (2.7),

$$P_l(\cos\alpha_{12}) = \frac{4\pi}{2l+1} \sum_m Y^*_{lm}(\theta_1,\phi_1)Y_{lm}(\theta_2,\phi_2), \tag{2.13}$$

using the convention that $\sum_m = \sum_{m=-l}^{l}$.

Thus the δ-function can be written

$$\boxed{\delta(\cos\chi - \cos\alpha_{12}) = 2\pi \sum_{lm} P_l(\cos\chi)Y^*_{lm}(\theta_1,\phi_1)Y_{lm}(\theta_2,\phi_2).} \tag{2.14}$$

The dependence on the two direction vectors are now separated.

Since

$$Y_{00}(\theta,\phi) = Y^*_{00}(\theta,\phi) = \frac{1}{\sqrt{4\pi}}, \tag{2.15}$$

both $Y^*_{lm}(\theta_1,\phi_1)$ and $Y_{lm}(\theta_2,\phi_2)$ are given by

$$Y^{(*)}_{lm}(\theta,\phi) = \sqrt{4\pi}Y_{00}(\theta,\phi)Y^{(*)}_{lm}(\theta,\phi). \tag{2.16}$$

The orthonormality relation for spherical harmonics, (2.9), gives

$$\int_0^{2\pi}\int_0^{\pi} Y_{lm}(\theta,\phi)\sin\theta d\theta d\phi = \int_0^{2\pi}\int_0^{\pi} Y^*_{lm}(\theta,\phi)\sin\theta d\theta d\phi = \sqrt{4\pi}\delta_{l0}\delta_{m0}. \tag{2.17}$$

Thus, using that for $l = 0$ the Legendre polynomial is

$$P_0(x) = 1, \tag{2.18}$$

the denominator in (2.6) is

$$\int\int \delta(\cos\chi - \cos\alpha_{12}) d\mathbf{\Omega_1} d\mathbf{\Omega_2} = 8\pi^2 P_0(\cos\chi) = 8\pi^2. \tag{2.19}$$

Now it remains to show that the numerator in (2.6) is equal to $2\pi \sum_{lm} |a_{lm}|^2 P_l(\cos\chi)$. The spherical harmonic coefficient a_{lm} can be written as

$$a_{lm} = \int_0^{2\pi} \int_0^{\pi} T(\theta,\phi) Y^*_{lm}(\theta,\phi) \sin\theta d\theta d\phi. \tag{2.20}$$

From this one finds the product $\mid a_{lm} \mid^2 = a_{lm} a^*_{lm}$ to be

$$\mid a_{lm} \mid^2 = \int\int T(\mathbf{\Omega_1}) T(\mathbf{\Omega_2}) Y^*_{lm}(\mathbf{\Omega_1}) Y_{lm}(\mathbf{\Omega_2}) d\mathbf{\Omega_1} d\mathbf{\Omega_2}, \tag{2.21}$$

using the definition $d\mathbf{\Omega} = \sin\theta d\theta d\phi$.

Multiplying (2.21) by $2\pi P_l(\cos\chi)$ and taking the sum over all l's and m's, one finds

$$2\pi \sum_{lm} P_l(\cos\chi) \mid a_{lm} \mid^2 = 2\pi \sum_{lm} \int\int P_l(\cos\chi) T(\mathbf{\Omega_1}) T(\mathbf{\Omega_2}) Y^*_{lm}(\mathbf{\Omega_1}) Y_{lm}(\mathbf{\Omega_2}) d\mathbf{\Omega_1} d\mathbf{\Omega_2}. \tag{2.22}$$

Using (2.14), the numerator in (2.6) becomes

$$\int\int T(\mathbf{\Omega_1}) T(\mathbf{\Omega_2}) \delta(\cos\chi - \cos\alpha_{12}) d\mathbf{\Omega_1} d\mathbf{\Omega_2} = 2\pi \sum_{lm} \mid a_{lm} \mid^2 P_l(\cos\chi). \tag{2.23}$$

From (2.19) and (2.23), one sees that the angular two-point correlation function on the full sphere is given by

$$\boxed{C(\chi) = \frac{1}{4\pi} \sum_{lm} \mid a_{lm} \mid^2 P_l(\cos\chi).} \tag{2.24}$$

This relation was applied to astronomy for the first time by Peebles (1973).

$\langle C(\chi) \rangle$, the average angular two-point correlation function on the full sphere

When averaging over infinitely many realizations, *e.g.* infinitely many universes, the angular two-point correlation function on the full sphere is

$$\langle C(\chi) \rangle = \frac{1}{4\pi} \sum_l (2l+1) C_l P_l(\cos\chi) \tag{2.25}$$

where C_l is the angular power spectrum, and the average $\langle\rangle$ is taken over all realizations.

This can be seen in the following way: When taking the average of Equation (2.6), only the temperature functions $T(\Omega)$ are affected. Thus the denominator is unaffected by the average and is given by Equation (2.19). The numerator is given by

$$\int\int \langle T(\mathbf{\Omega_1})T(\mathbf{\Omega_2})\rangle \delta(\cos\chi - \cos\alpha_{12}) d\mathbf{\Omega_1} d\mathbf{\Omega_2} = 2\pi \sum_{lm} \langle \mid a_{lm} \mid^2 \rangle P_l(\cos\chi). \tag{2.26}$$

The relationship between the power spectrum and the spherical harmonic coefficients a_{lm} is

$$\langle a_{lm} a^*_{l'm'} \rangle = \delta_{ll'}\delta_{mm'} C_l, \tag{2.27}$$

and the angular power spectrum, C_l, is defined as

$$\boxed{C_l \equiv \frac{1}{2l+1} \sum_m \langle \mid a_{lm} \mid^2 \rangle,} \tag{2.28}$$

since there are $(2l+1)$ m-modes for each l-mode.

Using (2.28), the average angular two-point correlation function on the full sphere is

$$\boxed{\langle C(\chi) \rangle = \frac{1}{4\pi} \sum_l (2l+1) C_l P_l(\cos\chi).} \tag{2.29}$$

Chapter 3

Deriving the correlation functions

The exact equations that connect C_l and $C(\chi)$ reviewed in Chapter 2 build on two assumptions: 1) The field $T(\mathbf{\Omega})$ is a continuous field making the integrals real integrals, and 2) the field $T(\mathbf{\Omega})$ is defined over the whole sphere, so that the orthogonality of the spherical harmonics can be exploited. In real world applications, none of these assumptions are fulfilled. In any CMB experiment the temperature will be measured in discrete pixels on the sky. And the correlations functions must be evaluated in bins, by multiplying and adding the pixel values for all pixel pairs with an angular separation that is within the limits of each bin. With this discretisation, integrals must be replaced by sums. Furthermore, quite large parts of the sky are polluted by foregrounds and must be cut out before the estimation of the correlations function. Also, when there is little interest in the largest scales, one may divide up the sky in many patches, estimate $C(\chi)$ on each patch and then average them. One main goal of this dissertation is to study the effect on C_l-estimation from measuring $C(\chi)$ in bins in χ and from basing the estimate on non-complete parts of the sky.

In this chapter I will derive analytically the connection between C_l and $C(\chi)$ when $C(\chi)$ is estimated in bins in χ, both for complete sky and when only circular patches or rings are accessible on the sky.

3.1 The binned two-point correlation function

3.1.1 Full sky coverage

The binned two-point correlation function for a bin with lower limit χ_1 and upper limit χ_2 is given as the average of $\langle \Delta T(\mathbf{\Omega_1}) \Delta T(\mathbf{\Omega_2}) \rangle$ where the angle between $\mathbf{\Omega_1}$ and $\mathbf{\Omega_2}$ is in the range $\chi_1 < |\mathbf{\Omega_1} - \mathbf{\Omega_2}| < \chi_2$. For full sky coverage it can easily be seen that by replacing the Dirac-delta function in Equation (2.6) with a step function $S(\cos\alpha_{12})_{\mu_1}^{\mu_2}$, where $\mu_1 = \cos\chi_1$ and $\mu_2 = \cos\chi_2$ limits the bin, the binned two-point function is given by

$$C(\chi)_{\chi_1}^{\chi_2} = \frac{\int\int T(\mathbf{\Omega_1}) T(\mathbf{\Omega_2}) S(\cos\alpha_{12})_{\mu_1}^{\mu_2} d\mathbf{\Omega_1} d\mathbf{\Omega_2}}{\int\int S(\cos\alpha_{12})_{\mu_1}^{\mu_2} d\mathbf{\Omega_1} d\mathbf{\Omega_2}}. \tag{3.1}$$

Since all functions, given some qualifications, can be written as a sum of Legendre polynomials, I expand the step-function into such a sum with coefficients $b_l{}^{\mu_2}_{\mu_1}$:

$$S(\cos\alpha_{12})^{\mu_2}_{\mu_1} = \sum_l b_l{}^{\mu_2}_{\mu_1} P_l(\cos\alpha_{12}). \tag{3.2}$$

I then multiply both sides of Equation (3.2) with $P_{l'}(\cos\alpha_{12})$, and integrate over $\cos\alpha_{12}$:

$$\int_{-1}^{1} S(\cos\alpha_{12})^{\mu_2}_{\mu_1} P_{l'}(\cos\alpha_{12}) d(\cos\alpha_{12}) = \sum_l b_l{}^{\mu_2}_{\mu_1} \int_{-1}^{1} P_l(\cos\alpha_{12}) P_{l'}(\cos\alpha_{12}) d(\cos\alpha_{12}). \tag{3.3}$$

Using the orthogonality and normalisation relation for Legendre polynomials (2.9), I find that

$$\int_{-1}^{1} S(\cos\alpha_{12})^{\mu_2}_{\mu_1} P_{l'}(\cos\alpha_{12}) d(\cos\alpha_{12}) = \sum_l \frac{2}{2l+1} b_l{}^{\mu_2}_{\mu_1} \delta_{ll'}. \tag{3.4}$$

From this I find that the coefficients can be written

$$b_l{}^{\mu_2}_{\mu_1} = \frac{2l+1}{2} \int_{-1}^{1} S(\cos\alpha_{12})^{\mu_2}_{\mu_1} P_l(\cos\alpha_{12}) d(\cos\alpha_{12}). \tag{3.5}$$

Using the addition theorem for spherical harmonics (Eq. (2.13)) on Equation (3.2), I can write the step function in terms of spherical harmonics,

$$S(\cos\alpha_{12})^{\mu_2}_{\mu_1} = \sum_l \frac{4\pi}{2l+1} b_l{}^{\mu_2}_{\mu_1} \sum_m Y^*_{lm}(\Omega_1) Y_{lm}(\Omega_2). \tag{3.6}$$

By redefining the set of coefficients with a more convenient normalisation

$$k_l{}^{\mu_2}_{\mu_1} \equiv \frac{4\pi}{2l+1} b_l{}^{\mu_2}_{\mu_1}, \tag{3.7}$$

I can write the step-function as

$$\boxed{S(\cos\alpha_{12})^{\mu_2}_{\mu_1} = \sum_{l=0}^{\infty} \sum_{m=-l}^{l} k_l{}^{\mu_2}_{\mu_1} Y^*_{lm}(\mathbf{\Omega_1}) Y_{lm}(\mathbf{\Omega_2}).} \tag{3.8}$$

The new coefficients $k_l{}^{\mu_2}_{\mu_1}$, which I call the Legendre transform, are hence

$$k_l{}^{\mu_2}_{\mu_1} = \frac{8\pi^2}{2l+1} \sum_{m=-l}^{l} \int_{-1}^{1} S(\cos\alpha_{12})^{\mu_2}_{\mu_1} Y^*_{lm}(\mathbf{\Omega_1}) Y_{lm}(\mathbf{\Omega_2}) d(\cos\alpha_{12}). \tag{3.9}$$

The angle α_{12} between the directional unit vectors $\mathbf{\Omega_1}$ and $\mathbf{\Omega_2}$ is given by Equation (2.7).

From (2.13), I see that $k_l^{\mu_2}_{\mu_1}$ can be written

$$k_l^{\mu_2}_{\mu_1} = 2\pi \int_{\mu_1}^{\mu_2} P_l(\cos\alpha_{12}) d(\cos\alpha_{12}), \tag{3.10}$$

since

$$S(\cos\alpha_{12})^{\mu_2}_{\mu_1} = \begin{cases} 1 & \text{for} \qquad \mu_1 \leq \cos\chi \leq \mu_2, \\ 0 & \text{otherwise.} \end{cases}$$

In Equation (3.10) $\cos\alpha_{12}$ is an arbitrary variable, so I choose to change the variable to μ. Thus the Legendre coefficient is given by

$$\boxed{k_l^{\mu_2}_{\mu_1} = 2\pi \int_{\mu_1}^{\mu_2} P_l(\mu) d\mu.} \tag{3.11}$$

Replacing $S(\mu_\alpha)^{\mu_2}_{\mu_1}$ with (3.8) in Equation (3.1) gives

$$C(\chi)^{\chi_2}_{\chi_1} = \frac{\sum_{lm} k_l^{\mu_2}_{\mu_1} \int\int T(\mathbf{\Omega_1}) T(\mathbf{\Omega_2}) Y^*_{lm}(\mathbf{\Omega_1}) Y_{lm}(\mathbf{\Omega_2}) d\mathbf{\Omega_1} d\mathbf{\Omega_2}}{\sum_{lm} k_l^{\mu_2}_{\mu_1} \int\int Y^*_{lm}(\mathbf{\Omega_1}) Y_{lm}(\mathbf{\Omega_2}) d\mathbf{\Omega_1} d\mathbf{\Omega_2}}. \tag{3.12}$$

Using (2.17), the denominator in Equation (3.1) becomes

$$4\pi \sum_{lm} k_l^{\mu_2}_{\mu_1} \delta_{l0} \delta_{m0} = 4\pi k_0^{\mu_2}_{\mu_1}. \tag{3.13}$$

By expanding $T(\mathbf{\Omega})$ into a sum of spherical harmonics

$$T(\mathbf{\Omega}) = \sum_{lm} a_{lm} Y_{lm}(\mathbf{\Omega}), \tag{3.14}$$

and using that $T(\mathbf{\Omega}) = T^*(\mathbf{\Omega})$, the numerator in (3.1) becomes

$$\begin{aligned} &\sum_{l,l',l''} \sum_{m,m',m''} k_l^{\mu_2}_{\mu_1} a_{l'm'} a^*_{l''m''} \int Y^*_{lm}(\mathbf{\Omega_1}) Y_{l'm'}(\mathbf{\Omega_1}) d\mathbf{\Omega_1} \int Y_{lm}(\mathbf{\Omega_2}) Y^*_{l''m''}(\mathbf{\Omega_2}) d\mathbf{\Omega_2} \\ &= \sum_{lm} k_l^{\mu_2}_{\mu_1} \mid a_{lm} \mid^2 . \end{aligned} \tag{3.15}$$

since

$$\int Y^*_{lm}(\mathbf{\Omega}) Y_{l'm'}(\mathbf{\Omega}) d\mathbf{\Omega} = \delta_{ll'} \delta_{mm'}. \tag{3.16}$$

From Equations (3.13) and (3.15) I find that the binned two-point correlation function on the full sphere is

$$\boxed{C(\chi)^{\chi_2}_{\chi_1} = \frac{1}{4\pi k_0} \sum_{lm} k_l^{\mu_2}_{\mu_1} \mid a_{lm} \mid^2,} \tag{3.17}$$

where the Legendre transform $k_l^{\mu_2}_{\mu_1}$ is given by Equation (3.11).

The average binned two-point correlation function - full sky coverage

When taking the average of Equation (3.17) over all realizations, only the a_{lm}'s are affected. This gives

$$\langle C(\chi)_{\chi_1}^{\chi_2} \rangle = \sum_{lm} k_l{}_{\mu_1}^{\mu_2} \langle \mid a_{lm} \mid^2 \rangle. \tag{3.18}$$

Using the definition of the power spectrum in Equation (2.28), I find that the binned correlation function is given in terms of the power spectrum C_l by

$$\boxed{\langle C(\chi)_{\chi_1}^{\chi_2} \rangle = \frac{1}{4\pi k_0} \sum_l (2l+1) C_l k_l{}_{\mu_1}^{\mu_2}.} \tag{3.19}$$

3.2 The angular two-point correlation function - partial sky coverage

Most CMB experiments observe smaller patches of the sky, and even experiments scanning the full sky will, because of various foregrounds, never be able to observe the CMB radiation from the complete celestial sphere. On the cut sphere the Legendre polynomials are no longer independent or normalised, since Equation (3.16) is only valid on the full sphere. This makes Equations (2.24) and (2.29), and their binned equivalents (3.17) and (3.19), invalid in cases of partial sky coverage.

3.2.1 The angular two-point correlation function - disk-shaped sky patches

In this section I derive the two-point correlation functions in the case where the sky patches are shaped like disks of various sizes. The unbinned equations were derived independently by Torstein O. Sæbø and myself, while the binned equations are based on the equations I derived in Section 3.1.

First I review the unbinned case. From the Equations (2.6), (2.14) and (2.15) it is easy to see that, independent of sky coverage, the denominator can be written as

$$\begin{aligned} &\int_{\delta\Omega} \int_{\delta\Omega} \delta(\cos\chi - \cos\alpha_{12}) d\boldsymbol{\Omega_1} d\boldsymbol{\Omega_2} \\ &= 8\pi^2 \sum_l P_l(\cos\chi) \sum_m \int_{\delta\Omega} Y_{00}(\Omega_1) Y_{lm}^*(\Omega_1) d\Omega_1 \int_{\delta\Omega} Y_{00}(\Omega_2) Y_{lm}(\Omega_2) d\Omega_2. \end{aligned} \tag{3.20}$$

The integrals are taken over the surface area $\delta\Omega$ of the observed sky patch.

On a circular patch of the sphere with radius $\theta_{\max}$, the normalisation of the spherical harmonic functions Y_{lm} are no longer given by Equation (3.16). In order to obtain a new normalisation, I use the fact that the Y_{lm}'s can be written as a function of the associated Legendre polynomials

$$Y_{lm}(\Omega) = A_{lm} P_{lm}(\cos\theta) e^{im\phi}, \tag{3.21}$$

where

$$A_{lm} = \sqrt{\frac{(2l+1)}{4\pi}\frac{(l-m)!}{(l+m)!}}. \tag{3.22}$$

Hence

$$\begin{aligned}\int_{\delta\Omega} Y_{lm}(\Omega) Y^*_{l'm'}(\Omega)\mathrm{d}\Omega &= A^{mm'}_{ll'} \int_{\theta_{\min}}^{\theta_{\max}} P_{lm}(\cos\theta) P_{l'm'}(\cos\theta)\sin\theta \mathrm{d}\theta \int_0^{2\pi} e^{i(m-m')\phi}\mathrm{d}\phi \\ &= 2\pi A^{mm'}_{ll'} \int_{\theta_{\min}}^{\theta_{\max}} P_{lm}(\cos\theta) P_{l'm'}(\cos\theta)\sin\theta \mathrm{d}\theta \delta_{mm'} \end{aligned} \tag{3.23}$$

where

$$A^{mm'}_{ll'} = \frac{\sqrt{(2l+1)(2l'+1)}}{2}\sqrt{\frac{(l-m)!}{(l+m)!}\frac{(l'-m')!}{(l'+m')!}}. \tag{3.24}$$

Defining the integral $I^{mm'}_{ll'}$,

$$\boxed{I^{mm'}_{ll'} = 2\pi \int_{\cos\theta_{max}}^{\cos\theta_{min}} P_{lm}(\mu) P_{l'm'}(\mu) d\mu,} \tag{3.25}$$

the normalisation on a circular patch of the sphere is:

$$\boxed{\int_{\delta\Omega} Y_{lm}(\Omega) Y^*_{l'm'}(\Omega) d\Omega = A^{mm'}_{ll'} I^{mm'}_{ll'} \delta_{mm'}.} \tag{3.26}$$

As the position of the sky patch on the sphere is unimportant, I have chosen the orientation of the sphere so that the patch I look at is centred on the north pole/one of the poles, thus obtaining azimuthal symmetry. This means that $m = m'$, and the expressions $I^{mm'}_{ll'}$ and $A^{mm'}_{ll'}$ reduces to $I^{m}_{ll'}$ and $A^{m}_{ll'}$ respectively. For the denominator, this gives

$$8\pi^2 \sum_l P_l(\mu) \sum_m (A^0_{l0} I^0_{l0})^2 = 2\pi^2 \sum_l (2l+1) P_l(\cos\chi) I^2_l \tag{3.27}$$

where

$$A^2_l = (A^0_{l0})^2 = \frac{2l+1}{4}, \tag{3.28}$$

and

$$I_l = I^0_{l0} = \int_{\cos\theta_{max}}^{\cos\theta_{min}} P_l(\mu) d\mu, \tag{3.29}$$

having used the Legendre property of Equation (2.18).

The expression for the denominator for a circular patch can be simplified even further. Setting $\theta_{min} = 0$ and $\theta_{max} = r$, we see that for $l \geq 1$, the integral over $P_l(\mu)$ is

$$\int_{\cos r}^{1} P_l(\mu)d\mu = \frac{(P_{l-1,0}(\cos r) - P_{l+1,0}(\cos r))}{2l+1} = -\sin r P_{l,-1}(\cos r), \tag{3.30}$$

where I have used the following recursion formulas for Legendre and associated Legendre polynomials:

$$(2l+1)P_l(x) = \frac{d}{dx}P_{l+1}(x) - \frac{d}{dx}P_{l-1}(x) \tag{3.31}$$

and

$$\frac{P_{l-1,m}(x) - P_{l+1,m}(x)}{(2l+1)} = \sqrt{1-x^2}P_{l,m-1}(x). \tag{3.32}$$

Note that both recursion formulas are only valid for l$\geq$ 1.

Thus, for disk-shaped sky patches with radius r, the integral I_l is

$$I_l = \int_{\cos r}^{1} P_l(\mu)d\mu = \begin{cases} 1-\cos r & \text{for} \quad l = 0, \\ -\sin r P_{l,m=-1}(\cos r) & \text{for} \quad l \geq 1. \end{cases} \tag{3.33}$$

The denominator in this case therefore becomes

$$\int_{\delta\Omega}\int_{\delta\Omega} \delta(\cos\chi - \cos\alpha_{12})d\mathbf{\Omega_1}d\mathbf{\Omega_2} = 2\pi^2(1-\cos r)^2 + \sin r^2 \sum_{l=1}^{\infty}(2l+1)P_l(\cos\chi)[P_{l,-1}(\cos r)]^2). \tag{3.34}$$

From Equations (2.6) and (2.14) it is easy to see that independent of sky coverage the numerator can be written as

$$\begin{aligned} &\int_{\delta\Omega}\int_{\delta\Omega} T(\mathbf{\Omega_1})T(\mathbf{\Omega_2})\delta(\cos\chi - \cos\alpha_{12})d\mathbf{\Omega_1}d\mathbf{\Omega_2} \\ &= 2\pi\sum_l P_l(\cos\chi)\sum_m \int_{\delta\Omega} T(\Omega_1)Y^*_{lm}(\Omega_1)d\Omega_1 \int_{\delta\Omega} T(\Omega_2)Y_{lm}(\Omega_2)d\Omega_2. \end{aligned} \tag{3.35}$$

By using that $T(\Omega) = T(\Omega)^*$ and expanding the temperature function $T(\Omega)$ into a sum of spherical harmonic, this becomes

$$\begin{aligned} &\int_{\delta\Omega}\int_{\delta\Omega} T(\mathbf{\Omega_1})T(\mathbf{\Omega_2})\delta(\cos\chi - \cos\alpha_{12})d\mathbf{\Omega_1}d\mathbf{\Omega_2} \\ &= 2\pi\sum_{lm} P_l(\cos\chi)\sum_{l'm'} a_{l'm'}\int_{\delta\Omega} Y_{l'm'}(\Omega_1)Y^*_{lm}(\Omega_1)d\Omega_1 \sum_{l''m''} a^*_{l''m''}\int_{\delta\Omega} Y^*_{l''m''}(\Omega_2)Y_{lm}(\Omega_2)d\Omega_2. \end{aligned} \tag{3.36}$$

One way of proceeding is to use the pseudo power spectrum defined by E. Hivon, B. Wandelt and K. Gorski (Wandelt et al., 2001),

$$\boxed{\tilde{C}_l = \frac{1}{2l+1}\sum_m \tilde{a}_{lm}\tilde{a}^*_{lm},} \tag{3.37}$$

where the pseudo spherical harmonic coefficient is

$$\boxed{\tilde{a}_{lm} = \sum_{l'm'} a_{l'm'} \int_{\delta\Omega} Y_{l'm'}(\Omega) Y^*_{lm}(\Omega) d\Omega.} \tag{3.38}$$

Note that all dependence on the geometry of the sky patch is contained in the $\tilde{a}_{lm}$'s.

Using the notation above, the numerator (Eq. 3.36) can be written

$$2\pi \sum_l P_l(\mu) \sum_m \mid \tilde{a}_{lm} \mid^2 = 2\pi \sum_l (2l+1)\tilde{C}_l P_l(\cos\chi). \tag{3.39}$$

Thus the angular two-point correlation function in the case of disk-shaped sky patches, is

$$\boxed{C(\chi)_{\rm disk} = \frac{\sum_l (2l+1)\tilde{C}_l P_l(\cos\chi)}{D(\chi)},} \tag{3.40}$$

or equivalently

$$C(\chi)_{\rm disk} = \frac{\sum_{lm} P_l(\cos\chi)\tilde{a}_{lm}\tilde{a}^*_{lm}}{D(\chi)}, \tag{3.41}$$

where $D(\chi)$ in the case of azimuthal symmetry is

$$D(\chi) = \pi \left[(\cos r - 1)^2 + \sin^2 r \sum_{l=1}^{\infty} (2l+1) P_l(\cos\chi) \left[P_{l,-1}(\cos r) \right]^2 \right], \tag{3.42}$$

and the $\tilde{a}_{lm}$'s are found by using Equations (3.26) and (3.38).

The average angular two-point correlation function
- disk-shaped sky patches

Taking the average of Equation (3.41) over all realizations, only the $\tilde{a}_{lm}$'s are affected. The denominator is given by (3.42).

The average equivalent to the pseudo power spectrum in (3.37) is

$$\boxed{\langle \tilde{C}_l \rangle = \frac{1}{2l+1}\sum_m \langle \tilde{a}_{lm}\tilde{a}^*_{lm} \rangle.} \tag{3.43}$$

Replacing the average $\tilde{a}_{lm}$'s with (3.43), the average two-point correlation function in the case of disk-shaped sky patches becomes

$$\boxed{\langle C(\chi)_{\rm disk}\rangle = \frac{\sum_l (2l+1)\langle \tilde{C}_l\rangle P_l(\cos\chi)}{D(\chi)},} \tag{3.44}$$

where $D(\chi)$ is given by Equation (3.42).

3.2.2 The binned two-point correlation function - disk-shaped sky patches

In the case of partial sky coverage, the binned two-point correlation function is given by

$$C(\chi)^{\chi_2}_{\chi_1,\rm partial} = \frac{\int_{\delta\Omega}\int_{\delta\Omega} T(\mathbf{\Omega_1})T(\mathbf{\Omega_2})S(\mu_\alpha)^{\mu_2}_{\mu_1} d\mathbf{\Omega_1} d\mathbf{\Omega_2}}{\int_{\delta\Omega}\int_{\delta\Omega} S(\mu_\alpha)^{\mu_2}_{\mu_1} d\mathbf{\Omega_1} d\mathbf{\Omega_2}}, \tag{3.45}$$

where the step function $S(\mu_\alpha)^{\mu_2}_{\mu_1}$ is given by Equation (3.8). The integrals are taken over the surface area $\delta\Omega$ of the observed sky patch.

I combine the procedures of Sections 3.1.1 and 3.2.1. First I take a look at the denominator in (3.45). To exploit azimuthal symmetry, I split the spherical harmonic Y_{lm} in a polar and and azimuthal part. Using this and Equation (3.8), I find that

$$\int_{\delta\Omega}\int_{\delta\Omega} S(\mu_\alpha)^{\mu_2}_{\mu_1} d\mathbf{\Omega_1} d\mathbf{\Omega_2} = \sum_{lm} k_l{}^{\mu_2}_{\mu_1} A^2_{lm} \int_{\delta\Omega}\int_{\delta\Omega} P_{lm}(\mu_{1'}) P_{lm}(\mu_{2'}) e^{im(\phi_1-\phi_2)} d\mu_{1'} d\mu_{2'} d\phi_1 d\phi_2, \tag{3.46}$$

where $\mu_{i'} = \cos\theta_i$.

In (3.46) $\mu_{i'}$ are arbitrary variables, and the integrals over ϕ_i equals zero unless $m = 0$. Thus the integrals can be written

$$\int_{\delta\Omega}\int_{\delta\Omega} S(\mu_\alpha)^{\mu_2}_{\mu_1} d\mathbf{\Omega_1} d\mathbf{\Omega_2} = 4\pi^2 \sum_l k_l{}^{\mu_2}_{\mu_1} A^2_l \left[\int_{\cos\theta_{\rm max}}^{\cos\theta_{\rm min}} P_l(\mu) d\mu\right]^2. \tag{3.47}$$

A^2_l is given by (3.28).

Looking at a disk with radius r on the sphere, this becomes

$$4\pi^2 \sum_l k_l{}^{\mu_2}_{\mu_1} A^2_l \left[\int_{\cos\theta_{\rm max}}^{\cos\theta_{\rm min}} P_l(\mu) d\mu\right]^2 = 2\pi^2 \left(k_0{}^{\mu_2}_{\mu_1} (\cos r - 1)^2 + \sum_{l=1}^{\infty} (2l+1) k_l{}^{\mu_2}_{\mu_1} [\int_{\cos r}^{1} P_l(\mu) d\mu]^2 \right). \tag{3.48}$$

Using (3.33), the denominator in Equation (3.45) becomes

$$\int_{\delta\Omega}\int_{\delta\Omega} S(\mu_\alpha)^{\mu_2}_{\mu_1} d\mathbf{\Omega_1} d\mathbf{\Omega_2} = 2\pi^2 \left(k_0{}^{\mu_2}_{\mu_1} (\cos r - 1)^2 + \sin^2 r \sum_{l=1}^{\infty} (2l+1) k_l{}^{\mu_2}_{\mu_1} [P_{l,-1}(\cos r)]^2 \right). \tag{3.49}$$

I now look at the numerator: When I replace $T(\mathbf{\Omega})$ with the sum of harmonics (3.14), and use that $T(\mathbf{\Omega}) = T^*(\mathbf{\Omega})$, the numerator becomes

$$\int_{\delta\Omega}\int_{\delta\Omega} T(\mathbf{\Omega_1})T(\mathbf{\Omega_2})S(\mu_\alpha)_{\mu_1}^{\mu_2} d\mathbf{\Omega_1} d\mathbf{\Omega_2} \tag{3.50}$$
$$= \sum_{l,l',l''}\sum_{m,m',m''} k_{l\,\mu_1}^{\mu_2} \int_{\delta\Omega} a_{l'm'} Y_{l'm'}(\mathbf{\Omega_1}) Y^*_{lm}(\mathbf{\Omega_1}) d\mathbf{\Omega_1} \int_{\delta\Omega} a^*_{l''m''} Y^*_{l''m''}(\mathbf{\Omega_2}) Y_{lm}(\mathbf{\Omega_2}) d\mathbf{\Omega_2}.$$

From Equation (3.23) I see that when integrating over $\delta\Omega$, only $m = m' = m''$ contributes to the sums over all m' and m''. Hence, using Equation (3.38), the numerator in (3.45) becomes

$$\sum_l k_{l\,\mu_1}^{\mu_2} \sum_m \tilde{a}_{lm}\tilde{a}^*_{lm} = \sum_l k_{l\,\mu_1}^{\mu_2} \langle \tilde{C}_l \rangle, \tag{3.51}$$

with the pseudo power spectrum $\tilde{C}_l$ from Equation (3.37).

I therefore find that in the case of partial sky coverage with disk-shaped sky patches, the two-point pseudo correlation function on the sphere is

$$\boxed{\langle C(\chi)^{\chi_2}_{\chi_1,\mathrm{disk}} \rangle = \frac{\sum_l (2l+1)\tilde{C}_l k_{l\,\mu_1}^{\mu_2}}{2\pi D(\chi)_{\mathrm{bin}}},} \tag{3.52}$$

or equivalently

$$\langle C(\chi)^{\chi_2}_{\chi_1,\mathrm{disk}} \rangle = \frac{\sum_l k_{l\,\mu_1}^{\mu_2} \sum_m \mid \tilde{a}_{lm} \mid^2}{2\pi D(\chi)_{\mathrm{bin}}}. \tag{3.53}$$

In the case of azimuthal symmetry $D(\chi)_{\mathrm{bin}}$ is

$$D(\chi)_{\mathrm{bin}} = \pi \left[k_{0\,\mu_1}^{\mu_2} (\cos r - 1)^2 + \sin^2 r \sum_{l=1}^{\infty} (2l+1) k_{l\,\mu_1}^{\mu_2} [P_{l,-1}(\cos r)]^2 \right]. \tag{3.54}$$

The average binned two-point correlation function - disk-shaped sky patches

When taking the average of Equation (3.53) over all realizations, once again only the $\tilde{a}_{lm}$'s are affected and the denominator is given by Equation (3.49).

Using the expression for $\langle |\tilde{a}_{lm}|^2 \rangle$ from Equation (3.43), the numerator becomes

$$\int_{\delta\Omega}\int_{\delta\Omega} T(\mathbf{\Omega_1})T(\mathbf{\Omega_2})S(\mu_\alpha)_{\mu_1}^{\mu_2} d\mathbf{\Omega_1} d\mathbf{\Omega_2} = \sum_l (2l+1)\langle \tilde{C}_l \rangle k_{l\,\mu_1}^{\mu_2}. \tag{3.55}$$

So when averaging over infinitely many realizations, e.g. infinitely many universes or disk-shaped sky patches of equal size, the binned two-point pseudo correlation function becomes

$$\boxed{\langle C(\chi)^{\chi_2}_{\chi_1,\mathrm{disk}} \rangle = \frac{\sum_l (2l+1)\langle \tilde{C}_l \rangle k_{l\,\mu_1}^{\mu_2}}{2\pi D(\chi)_{\mathrm{bin}}}.} \tag{3.56}$$

Equivalently

$$\langle C(\chi)^{\chi_2}_{\chi_1,\mathrm{disk}} \rangle = \frac{\sum_l k_{l\,\mu_1}^{\mu_2} \sum_m \langle \tilde{a}_{lm}\tilde{a}^*_{lm} \rangle}{2\pi D(\chi)_{\mathrm{bin}}}. \tag{3.57}$$

3.2.3 Ring-shaped sky patches

There is a relatively natural further step in the development of the these equations, and that is the case of ring-shaped sky patches. I will not investigate this case any further in my thesis, but have included the expressions for completeness.

The two-point pseudo correlation function - ring-shaped sky patches

The only difference from circular patches is that a ring on the sphere will have an inner radius r_1 so that the lower limit of the bin is $\theta_{min} = r_1$ instead of 0. Thus the two-point correlation function in the case of ring-shaped sky patches with azimuthal symmetry is

$$C(\chi)_{\text{ring}} = \frac{\sum_l (2l+1)\tilde{C}_l P_l(\cos\chi)}{E(\chi)}, \tag{3.58}$$

and the average pseudo correlation function

$$\langle C(\chi)_{\text{ring}} \rangle = \frac{\sum_l (2l+1)\langle\tilde{C}_l\rangle P_l(\cos\chi)}{E(\chi)}. \tag{3.59}$$

In the case of azimuthal symmetry $E(\chi)$ is

$$E(\chi) = \pi \left[(\cos r_2 - \cos_{r_1})^2 + \sum_{l=1}^{\infty} (2l+1) P_l(\cos\chi) [\sin r_2 P_{l,-1}(\cos r_2) - \sin r_1 P_{l,-1}(\cos r_1)]^2) \right]. \tag{3.60}$$

The binned two-point correlation function - ring-shaped sky patches

In the case of binned ring-shaped sky patches, the two-point pseudo correlation function is

$$\boxed{C(\chi)^{\chi_2}_{\chi_1,\text{ring}} = \frac{{}_l(2l+1)\tilde{C}_l k_l^{\mu_2}_{\mu_1}}{2\pi E(\chi)_{\text{bin}}},} \tag{3.61}$$

and the average pseudo correlation function is

$$\langle C(\chi)^{\chi_2}_{\chi_1,\text{ring}} \rangle = \frac{\sum_l (2l+1)\langle\tilde{C}_l\rangle k_l^{\mu_2}_{\mu_1}}{2\pi E(\chi)_{\text{bin}}}. \tag{3.62}$$

In the case of azimuthal symmetry $E(\chi)_{\text{bin}}$ is

$$E(\chi)_{\text{bin}} = \pi \left[k_0^{\mu_2}_{\mu_1} (\cos r_2 - \cos_{r_1})^2 + \sum_{l=1}^{\infty} (2l+1) k_l^{\mu_2}_{\mu_1} [\sin r_2 P_{l,-1}(\cos r_2) - \sin r_1 P_{l,-1}(\cos r_1)]^2) \right]. \tag{3.63}$$

Chapter 4

Work and results

In chapter 3, I derived analytic formulae for the unbinned and binned angular two-point correlation functions, both for full sky coverage and for the case when only a disk or a ring of the sky is available for analysis. In this chapter I use these formulae to test whether binning is important and needs to be taken into account when the power spectrum is derived, and how these results are affected by limited sky coverage.

4.1 Full sky coverage

I start my analysis with the case with the least complications: complete sky coverage. Then I can isolate and do a detailed study of the effect of binning the data, making it easier to distinguish the binning effect from the effects of partial sky coverage later on.

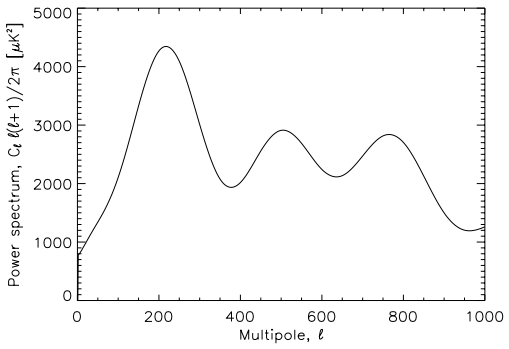

Figure 4.1: Plot showing the input power spectrum used in the calculations.

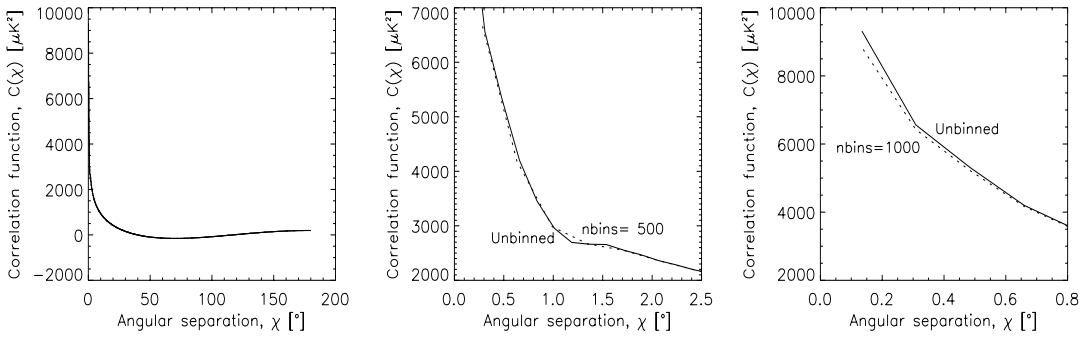

Figure 4.2: The unbinned and binned analytical two-point correlation functions for $N_{\rm bins} = 500$ and $N_{\rm bins} = l_{\rm max} = 1000$ at full sky coverage. In the left panel it is impossible to distinguish the three functions. The panel in the middle shows a close-up of the region around 2°, where the binned two-point function with $N_{\rm bins} = 500$ depart from the unbinned two-point function. In the right panel is a close-up of the region where the binned two-point function with $N_{\rm bins} = 1000$ begin to depart from the unbinned two-point function. Comparing the two close-ups, one can see that the fewer the bins are, the larger the deviations between the binned and the unbinned two-point functions become.

4.1.1 The binned and unbinned correlation function

To do a first analytical comparison of the binned and the unbinned two-point correlation functions, I calculated the average unbinned and binned analytical two-point correlation functions of Equations (2.29) and (3.19), using a fixed power spectrum pre-calculated with CMBFAST to fit the theoretical expectations of a CDM model, as input power spectrum. A plot of the input spectrum, which contains 1000 multipoles, is shown in Figure 4.1. The results of the correlation function calculations are shown in Figure 4.2.

In the left panel of Figure 4.2 I have plotted the binned and the unbinned correlation functions for multipoles up to $l_{\rm max} = 1000$. At first glance there does not seem to be any difference between the two functions, but a close-up of the plots shows a less comfortable reality. The panel in the middle shows a plot of the unbinned two-point function and the binned function with 500 bins ($N_{\rm bins} = 500$). Here one can clearly see that the largest differences appear in the first few bins, in this particular case at angles smaller than 2 degrees. This is as expected, since the bins have little sensitivity to features that are smaller than the bin size, the binning will have largest effect at small scales. The smallest features will simply be smoothed out. Unfortunately, these features are often also the cosmologically most interesting ones. So, in other words, the binning effect is largest at precisely those angles were we need the uncertainty to be as small as possible. Since the bin size sets the lower limit on how small a feature can be before it becomes undetectable, the differences between the binned and the unbinned

functions decrease as the number of bins increase, and hence the bin size is decreased. In this process, the number of differing bins between the two functions naturally also did decrease. When the number of bins equal the number of multipoles ($N_{\text{bins}} = l_{\text{max}}$) only the bins containing pairs with angular separation of less than 0.6 degrees, differed (see the right panel of Figure 4.2).

For reasons concerning sky coverage, as mentioned earlier, I have no way to compare the analytical full sky results with real CMB data. I could have simulated maps and calculated the average correlation function from them for comparison, but since I already in this first analytical examination found that it was difficult to read out any informative trends or details about the binning effect apart from the positive effect of increasing N_{bins}, I decided that the calculations would take up too much CPU time with the necessary map resolution ($N_{\text{side}} \geq 128$) compared to the little new information I would gain from the results.

4.1.2 The rederived power spectrum

In order to retrieve a more 'easy-to-read' picture of the loss of information caused by the binning, I decided instead to numerically rederive the power spectrum from the correlation functions to compare with the input spectrum. To rederive the power spectrum from the correlation function I chose to use Gauss-Legendre integration

$$C_l^{\text{recalc}} = 2\pi \int_0^{\pi} C(\chi)_{\text{binned}} P_l(\cos\chi) \sin\chi \mathrm{d}(\cos\chi) \simeq 2\pi \sum_{i=1}^{N_{\text{bins}}} w_i C(\arccos\mu_i)_{\text{binned}} P_l(\mu_i), \tag{4.1}$$

where $\mu_i = \cos\chi_i$, N_{bins} are the number of bins in the correlation function and w_i are weight functions estimated at the roots of Legendre polynomials (Press et al., 1992). For a more thorough discussion on the numerical integration of (4.1), see *e.g.* Sæbø (2002).

I also added both a beam and a pixel window to the rederived power spectra to get results that were closer to the results expected from satellite observations. Both the beam and the pixel window are window functions, *i.e.* functions that correct for effects that arises in the observation because of the choice of set up in the experiment, like beam geometry or pixelisation scheme. The rederived power spectra are shown in Figure 4.3, and compared with the input power spectrum.

We see that when the number of bins is smaller than the maximum number of multipoles present in the input spectrum, $N_{\text{bins}} < l_{\text{max}}$, it is difficult to regain much information about the input spectrum (see upper left panel of Figure 4.3). As the number of bins increase, the rederived power spectrum begins to more and more resemble the input spectrum, and already at $N_{\text{bins}} = l_{\text{max}}/2$ it is possible to recognise some of the features from the input spectrum in the rederived spectrum.

When the bin size is too large compared to the structures we are looking at, we are unable to gain any information about the object. In this case the structures are pixel pairs separated with an angular distance χ, so I will be unable to gain any information

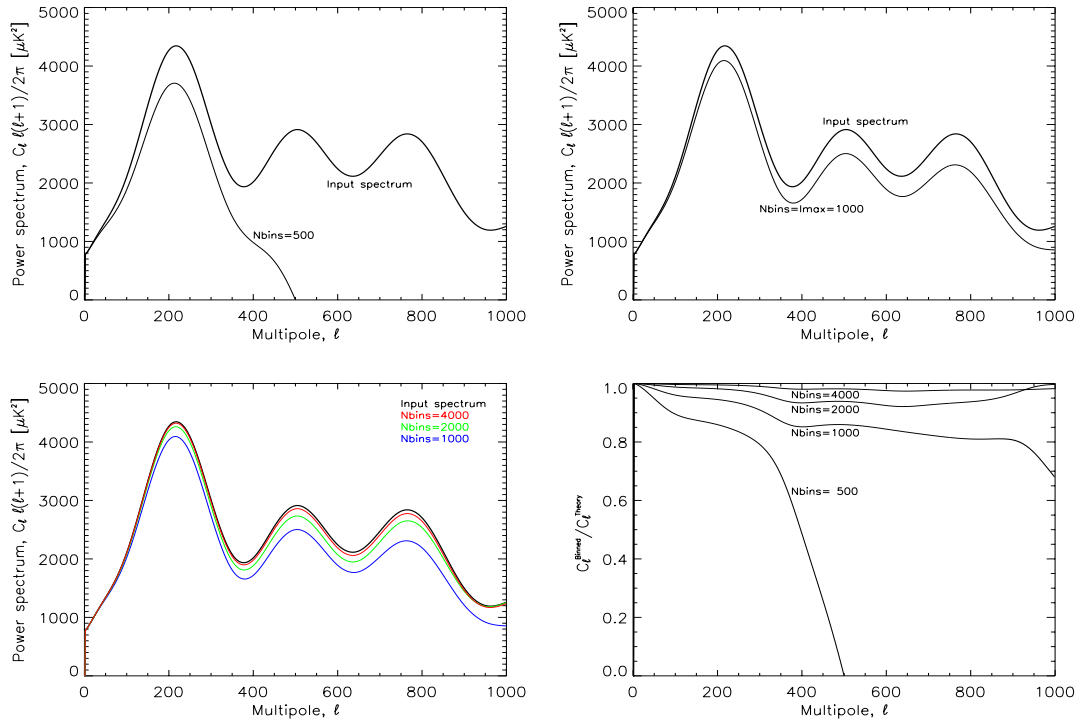

Figure 4.3: Comparison of the input power spectrum and the binned power spectra with different N_{bins} values for full sky coverage. The upper left panel shows the binned power spectrum for $N_{\text{bins}} \ll l_{\text{max}}$. Although some of the features from the input spectrum are recognisable in the rederived spectrum, most of the information from the input spectrum is lost. The upper right panel shows the binned spectrum of $N_{\text{bins}} = l_{\text{max}}$ versus the input spectrum. All features from the input spectrum are now recognisable, but the rederived spectrum still has less power than than the original spectrum. The lower left panel shows different binned power spectra where $N_{\text{bins}} \geq l_{\text{max}}$ versus the input power spectrum. The rederived spectra move asymptotically towards the input spectrum as the number of bins increase, and at $N_{\text{bins}} = 4l_{\text{max}}$ the difference between the input and the binned spectrum is almost negligible. The lower right panel shows the ratio of the binned power spectrum to the input spectrum for four different values of N_{bins}. Here one can see that at most the $N_{\text{bins}} = 4000$ spectrum differs 2% from the input spectrum. An analytical expression for the relation $C_l^{\text{Binned}}/C_l^{\text{Theory}}$ will give a binning window function W_b that can correct for the binning effect.

about the pairs unless the bin size is larger that the angular separation of the pixels. Knowing this, the observed behaviour in the rederived spectrum is just as expected, since the average bin size decreases as the number of bins increases.

The lower limit on the bin size is given by the pixel size used in the particular experiment, since the bins cannot be smaller than the pixels themselves. But how many bins do we *need* to retrieve all information in the input spectrum? This is much the same problem that the Nyquist sampling theorem is dealing with. The Nyquist theorem is related to Fourier transforms, and states that you need at least twice as many sampling points, or in my case bins, as there are 'input points' to get a good reproduction of the input data (Press et al., 1992). I am working with Legendre polynomials, so I cannot use the theorem directly, but since all functions, under some assumptions, can be written as Fourier series, it will still be of relevance. One factor that plays a role when using the Legendre polynomials, is where I position the sampling points. Torstein O. Sæbø investigated this matter in his master thesis and found that the best results were obtained when sampling at the angles χ where the derivate of Legendre polynomials with respect to χ became zero (Sæbø, 2002). Using this sampling regime, I have found that it is possible to reproduce a power spectrum once $N_{\text{bins}} \geq l_{\text{max}}$, *i.e.* when the number of bins is equal to or higher than the maximum number of multipoles (l_{max}) in the input spectrum, as can be seen in Figure 4.3.

Naturally, I also found that the rederived power spectra are consequently lying below the input spectrum, since the information loss that the binning causes naturally leads to less power in the rederived power spectra. When the number of bins increased, this loss decreased, and I got the observed asymptotic movement of the rederived power spectra towards the input spectrum, as seen in the lower left panel in Figure 4.3. When $N_{\text{bins}} \geq 4l_{\text{max}}$, the difference between the rederived spectrum and the input spectrum is less than 2% (see the lower left panel of Figure 4.3), so in this case the binning effect is so small that we need not take it into account when the power spectrum is calculated from the correlation function. For lower N_{bins} values a correction is needed, and a binning window function W_b can be developed from the relation $C_l^{\text{Binned}}/C_l^{\text{Theory}}$. The relation between the binned and the analytical power spectrum is plotted for different N_{bins} values in the lower right panel of Figure 4.3.

Conclusions

For full sky coverage the conclusion are the following: From an analytical comparison of the binned and the unbinned two-point correlation functions the two correlation functions were found to differ most at those scales where the features in the CMB was approximately equal to or smaller than the bin size, since the bins have little or no sensitivity at these scales.

If the input power spectrum is defined up to l_{max}, most of the information in the higher l's are lost if the correlation function is measured with $N_{\text{bins}} < l_{\text{max}}$. If $N_{\text{bins}} \gtrsim 4l_{\text{max}}$, the rederived power spectrum differs very little from the input power spectrum. This shows that in this case the binning makes a very small effect and need

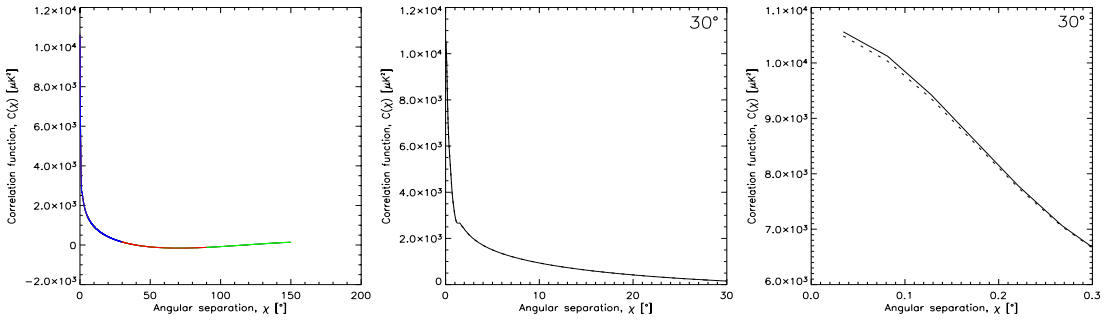

Figure 4.4: The binned and unbinned analytical two-point correlation functions at partial sky coverage. The left panel shows the binned and unbinned correlation functions for $R_{\max} = 30°$ (blue), 90° (red) and 150° (green), with $N_{\text{bins}} = N_{\text{bins}}^{\text{opt}}$ $N_{\text{bins}}^{\text{opt}}$ is the number of bins necessary to obtain less than 1% difference between the binned and the unbinned rederived power spectra. The panel in the middle shows the binned (dotted line) and the unbinned correlation function (solid line) for $R_{\max} = 30°$. As seen in the left and the middle panel, the two functions are apparently indistinguishable. The right panel shows a close-up of the smallest angles, where a small difference between the two functions is detectable at small angles. For $R_{\max} = 30°$ the two correlation functions only begin to differ at $\chi < 0.3°$ when $N_{\text{bins}} = N_{\text{bins}}^{\text{opt}}$.

not be taken into account when the power spectrum is calculated from the correlation function using Gauss-Legendre integration, but for $l_{\max} \leq N_{\text{bins}} \leq 4l_{\max}$ it is probably a good idea to use *e.g.* a binning window W_b to correct for the binning effect. Because of time limitation, I have not been able to look further into this matter.

4.2 Partial sky coverage

To get a more realistic picture of how the binning effect affects CMB experiments, the next step was to examine the behaviour of two-point correlation functions in the case of partial sky coverage.

4.2.1 The binned and unbinned correlation function

I calculated the unbinned and the binned analytical correlation functions from Equations (3.44) and (3.57), using the same original input power spectrum as in the case of full sky coverage. These correlation functions are shown in Figure 4.4. Apart from the cut off in the functions caused by the partial sky coverage (see the left panel in Figure 4.4), it is difficult to see any new features of the binning effect in these results.

4.2.2 The rederived power spectra

As for the case with full sky coverage, I rederived the power spectrum from the binned correlation functions in the same way as in Chapter 4.1.2. The results are shown in Figures 4.5 and 4.6. The number of bins necessary to obtain less than 1% difference between the binned and the unbinned rederived power spectra is called $N_{\rm bins}^{\rm opt}$. For more on how $N_{\rm bins}^{\rm opt}$ is found and how it is related to sky coverage and $l_{\rm max}$, see Section 4.2.3. I have also compared the pseudo power spectrum, calculated from Equation (3.37), with the input power spectrum. These results can be seen in Figure 4.7.

For all values of $l_{\rm max}$, the unbinned and the binned power spectra clearly oscillate around the pseudo-C_l's at partial sky coverage (see Figures 4.5 and 4.6). Both the wavelength and the amplitude of the oscillations depend on the sky coverage (i.e. $R_{\rm max}$), but is independent of the number of bins and multipoles l, as can be seen in Figure 4.6.

The oscillations are caused by the cutoff in the correlation function due to the fact that we have partial sky coverage, and were also seen by Torstein Sæbø during the work on his master thesis (Sæbø, 2002). In his thesis he suggests to correct for this by letting the "missing" part of the correlation function be represented by a constant. Instead of correcting for the oscillations by inserting a constant in the correlation functions, I will in Section 4.2.3 try to remove the oscillation from the rederived power spectra through filtering, first using a Fast Fourier Transform (FFT) filter and then a running average filter.

Whether correcting the two-point function or filtering of the power spectra as mentioned above is the correct thing to do in the light of further use and analysis, is a subject for further investigation. If it turns out that not correcting for this gives incorrect results in a maximum likelihood analysis, or other types of data analysis, we end up with wrong conclusions for the Universe. If so, the need for a correction is definitively present.

Since both the binned and unbinned power spectra are oscillating, it is difficult to read anything from them without filtering out the oscillations (see Figures 4.5 and 4.6). But the pseudo power spectrum and the input power spectrum are naturally not affected by the oscillations, since they are neither binned nor sampled, and are thus readable without filtering. A comparison of the input and pseudo spectrum can be seen in Figure 4.7. The input spectrum is naturally constant, since it is not affected by any of the processes involved. The pseudo spectrum is unaffected by the binning, but vary slightly with $R_{\rm max}$ because of the coupling between the a_{lm}'s (see Figure 4.7). The smaller $R_{\rm max}$ is, the larger the coupling between the a_{lm}'s become, and hence the larger the deviation between the input spectrum and the pseudo spectrum.

As can be seen in Figure 4.7, the pseudo-C_l's follow the input-C_l's very well, particularly near the peaks (see the upper panels in Figure 4.7). The most prominent deviations are in the troughs between the peaks, like in the multipole range $l \sim [300 - 450]$ seen in the lower right panel in Figure 4.7. There is also a small visible difference between the two power spectra for the very lowest multipole values, $l = [0, \sim 5]$ (see the

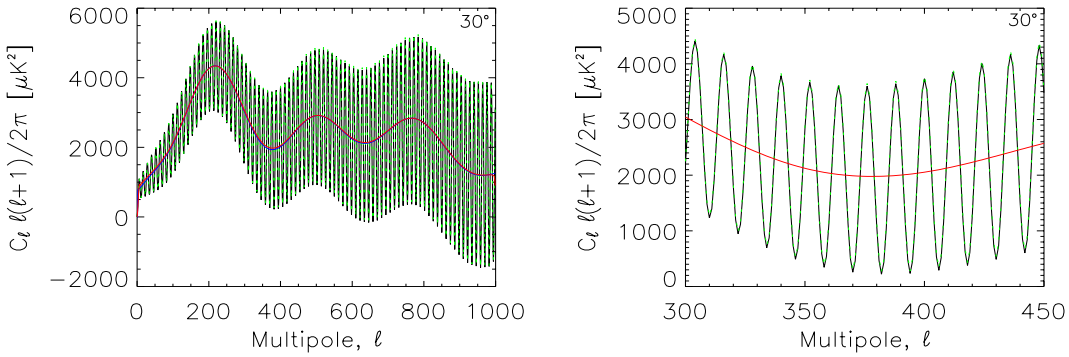

Figure 4.5: Plots of the oscillations in the rederived binned and unbinned power spectra at partial sky coverage ($R_{\max} = 30°, N_{\text{bins}} = 1000, l_{\max} = 1000$). In both panels the rederived binned spectrum (dotted green line) and unbinned spectrum (solid black line) are seen to be oscillating around the pseudo power spectrum (solid red line). In the left panel the amplitude of the oscillations is seen to increase towards higher l, but as the close-up of the region around the first trough in the right panels shows, the wavelength remains constant for all l.

lower right panel in Figure 4.7) and for the very highest multipole values, $l = [0, \sim 5]$ and $l = [\sim 990, 1000]$, where the pseudo-C_l is over- and underestimated respectively, compared to the input spectrum.

4.2.3 Filtering

As seen in the last section, recomputing the power spectrum by integrating over the binned or the unbinned correlation function gives power spectra that oscillate strongly at all $R_{\max}$ values. In order to remove the oscillations, I tried out two different filters, a Fast Fourier Transform filter and a running average filtering.

FFT filtering The FFT filter was applied by using the following procedure: first I found the Fast Fourier Transform of the power spectrum using a predefined IDL procedure. Then I located the frequencies of the oscillations, manually removed these, and then used the IDL procedure to calculate the inverse FFT of this adjusted Fourier transform. If the frequency of the oscillations was successfully removed, the resulting power spectra would be smooth. But in most cases the frequencies were not properly removed and the resulting power spectra still inhabited oscillations, though profoundly reduced compared to the original oscillations. As I needed the oscillations to be completely removed in order to properly distinguish between the effects of binning and the effects of partial sky coverage, I would have to repeat the FFT filtering over and over until the oscillations were completely removed. As can be seen in the lower left panel of Figure 4.8, the resulting power spectra follows the pseudo spectrum quite well and

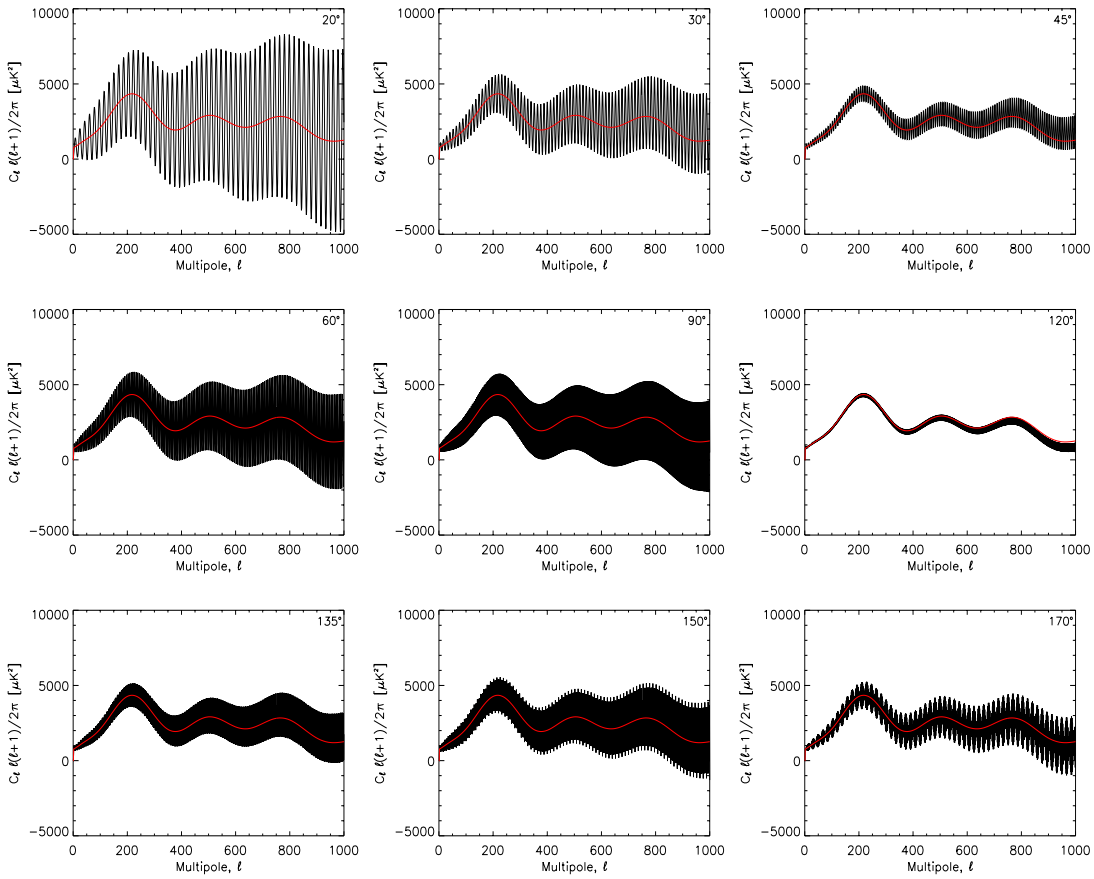

Figure 4.6: Plots of the unfiltered power spectra at partial sky coverage with $l_{\max} = 1000$ and $N_{\text{bins}} = N_{\text{bins}}^{\text{opt}}$. The solid red line is the pseudo power spectrum. The binned and the unbinned power spectra are indistinguishable since $N_{\text{bins}} = N_{\text{bins}}^{\text{opt}}$, and the spectra hence only differ by 1% or less. The amplitude and wavelength of the oscillations are seen to vary with sky coverage, but seem to be independent of the number of bins used. The wavelength is also independent of the multipoles, while the amplitude show a slight increase with increasing l.

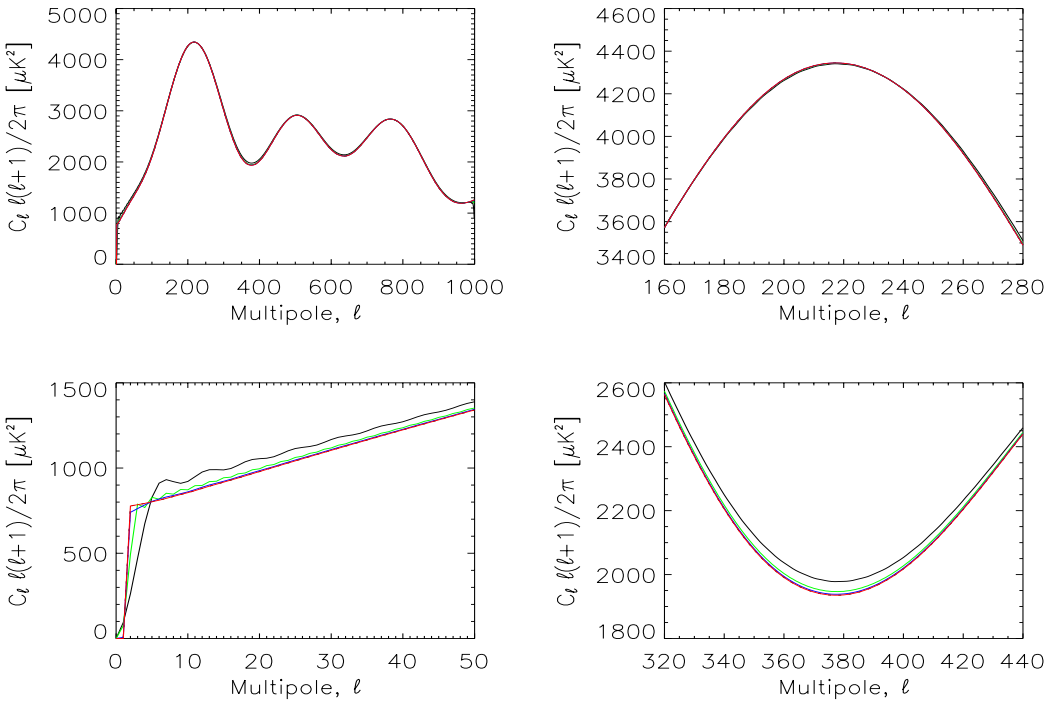

Figure 4.7: Plots of the input and pseudo power spectra at partial sky coverage with $l_{\max} = 1000$ and $R_{\max} = 30°$ (black), 90° (green) and 150° (blue). The upper left panel shows the input spectrum (red) versus the three pseudo spectra. The different spectra are almost indistinguishable. The upper right panel shows a close-up of the first top, note how well even the pseudo spectrum from $R_{\max} = 30°$ follows this top. The lower left panel shows a close-up of the first 50 multipoles, and the lower right panel a close-up of the first trough. Here there is a noticeable difference between the input spectrum and the pseudo spectrum from $R_{\max} = 30°$, while the two other pseudo spectra still follow the input spectrum quite well.

has lost little power through the filtering process. But considering the inconvenience in having to remove the oscillations manually and also the many iterations needed to obtain a satisfactory result, the FFT filter is a rather ineffective and inaccurate filter for the purpose of removing the oscillations in the rederived power spectra.

Running average filtering This method was a lot simpler than FFT filtering, as I just had to give the number of multipoles to be used as filter width before I applied a predefined IDL[1] procedure that calculated the running average filtered power spectra. Not only was this a simpler filtering method, it gave better results as well. But only if the filter width, *i.e.* the number of multipoles taken into account in each convolution

[1]Interactive Data Language.

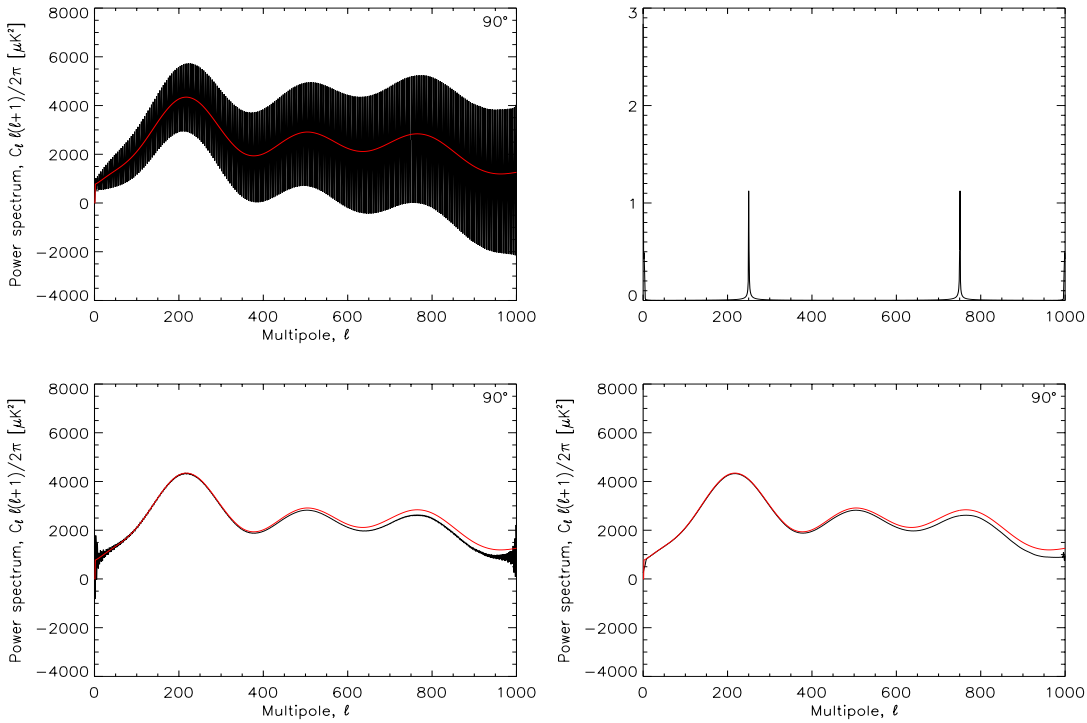

Figure 4.8: FFT vs. running average filtering. The upper left panel shows the unfiltered binned power spectrum (black) at 90^o sky coverage ($l_{\max} = 1000$). The red line imprinted on the binned spectrum is the pseudo power spectrum. The upper right panel shows the Fourier transform of the binned spectrum. The imposed oscillations from partial sky coverage is revealed by the two peaks at $l = 250$ (real) and $l = 750$ (imaginary). The lower left panel shows the resulting binned power spectrum after the two peaks at $l = 250$ and $l = 750$ have been removed, and an inverse FFT has been performed. Even after repeated use of the FFT filter, there are still oscillations present at the multipoles $l \lesssim 100$ and $l \gtrsim 900$. The lower right panel shows the resulting binned power spectrum after running average filtering. Here the oscillations are completely removed, but some small errors due to truncation can be seen at the very lowest and the very highest multipoles. When comparing the two lower panels, it is easy to see that the running average filter gives the best results.

was chosen optimally.

The optimal value of multipoles to be used in the filter, $N_{\text{conv}}^{\text{opt}}$, depends on the sky coverage $R_{\max}$, or to be more precise, on the wavelength λ_{osc} of the oscillations at the given sky coverage, and is independent of the l-resolution and the number of bins. The wavelength λ_{osc} is given by the simple relationship:

$$\lambda_{\text{osc}} = \frac{360^\circ}{R_{\max}}, \tag{4.2}$$

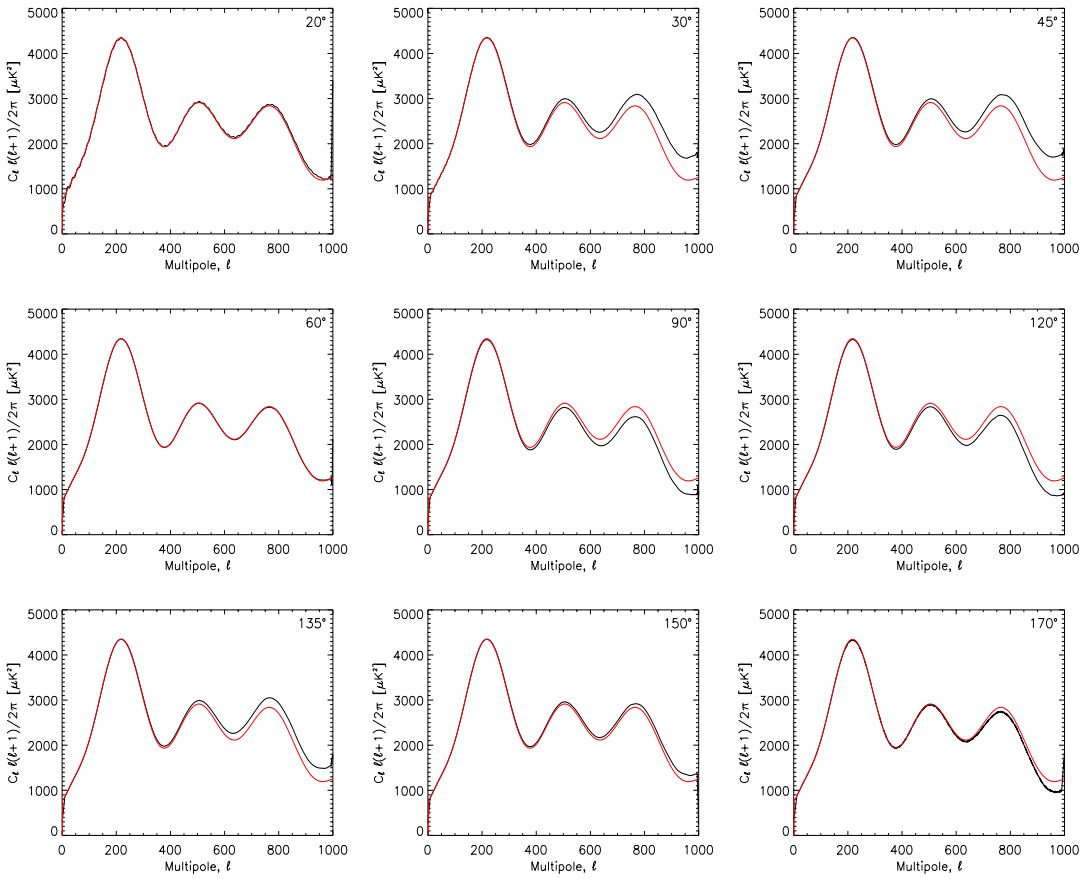

Figure 4.9: Plots of the running average filtered power spectra at partial sky coverage for $l_{\max} = 1000$, $N_{\text{bins}} = N_{\text{bins}}^{\text{opt}}$, and $N_{\text{conv}} = N_{\text{conv}}^{\text{opt}}$. The red lines imprinted on the running average filtered power spectra, is the pseudo power spectrum. The binned and the unbinned spectra are indistinguishable since $N_{\text{conv}} = N_{\text{conv}}^{\text{opt}}$. For practically all $R_{\max} \geq 30°$, the oscillations are completely removed with the running average filter. The first exceptions is $R_{\max} = 20°$, where the filter width is set to only one wavelength λ_{osc} to avoid severe loss of information. The second exception is $R_{\max} = 170°$ where the filter width, for the same reason as for $R_{\max} = 20°$ is set to $\approx 10 \cdot \lambda_{\text{osc}}$. Since the filter width then do not strictly contain an integer number of wavelengths, the filter is not able to remove the oscillations completely. Note that, depending on the sky coverage, the running average filtered spectra are either over- or underestimated compared to the pseudo spectrum.

$R_{\max}[^\circ]$	$\lambda_{\rm osc}$ $[l]$	$N_{\rm conv}^{\rm opt}[l]$
10	36	36
20	18	18
30	12	12
40	9	18
50	$\frac{36}{5}$	36
60	6	12
70	$\frac{36}{7}$	36
80	$\frac{9}{2}$	18
90	4	12
100	$\frac{18}{5}$	18
110	$\frac{36}{11}$	10
120	3	12
130	$\frac{36}{13}$	36
140	$\frac{18}{7}$	36
150	$\frac{12}{5}$	12
160	$\frac{9}{4}$	18
170	$\frac{36}{17}$	21
180	2	arbitrary

Table 4.1: The relation between sky coverage, wavelength of the oscillations imposed on the rederived power spectrum and the convolution width necessary to satisfactory remove the oscillations from the power spectrum. $N_{\rm conv}^{\rm opt}$ is chosen so that it is equal to the the smallest number of wavelengths that give an integer number of 10 or more. For $R_{\max} < 30^\circ$ the wavelengths are longer than $10l$, so not too lose to much information in the filtering, $N_{\rm conv}^{\rm opt}$ was set to one wavelength in these cases.

where $\lambda_{\rm osc}$ is in units of l and $R_{\max}$ is the sky coverage given in degrees. The optimal convolution width at different sky coverage is given in Table 4.1. How well the running average filter perform depends on how close the filter width is to $n \cdot \lambda_{\rm osc}$, where n is an integer ≥ 2 I have chosen to use $N_{\rm conv}^{\rm opt}$ equal to the the smallest number of wavelengths that gives an integer number of 10 or more, which for most $R_{\max}$ means two wavelengths or more. But for $R_{\max} < 30^\circ$ the wavelengths are longer than $10l$, so in order not to lose too much information in the filtering, I set $N_{\rm conv}^{\rm opt}$ equal to one wavelength in these cases. For the same reason I also chose to use filter widths that were only approximately an integer number of $\lambda_{\rm osc}$ for some $R_{\max}$ where $\lambda_{\rm osc}$ was a fractional number.

Having applied the running average filter on the rederived spectra, I found that if $N_{\rm bins}$ was lower than 5% of $N_{\rm bins}^{\rm opt}$, it was impossible to reconstruct the underlying input power spectrum from the binned C_l's (see the upper left panel in Figure 4.10). If $N_{\rm bins}$ was between 5 and 15% of $N_{\rm bins}^{\rm opt}$, then the unbinned and binned C_l's fell off rapidly as the number of bins decreased, and even obtained negative values (see the upper right panel in Figure 4.10). The behaviour of the power spectra is explained by the fact that

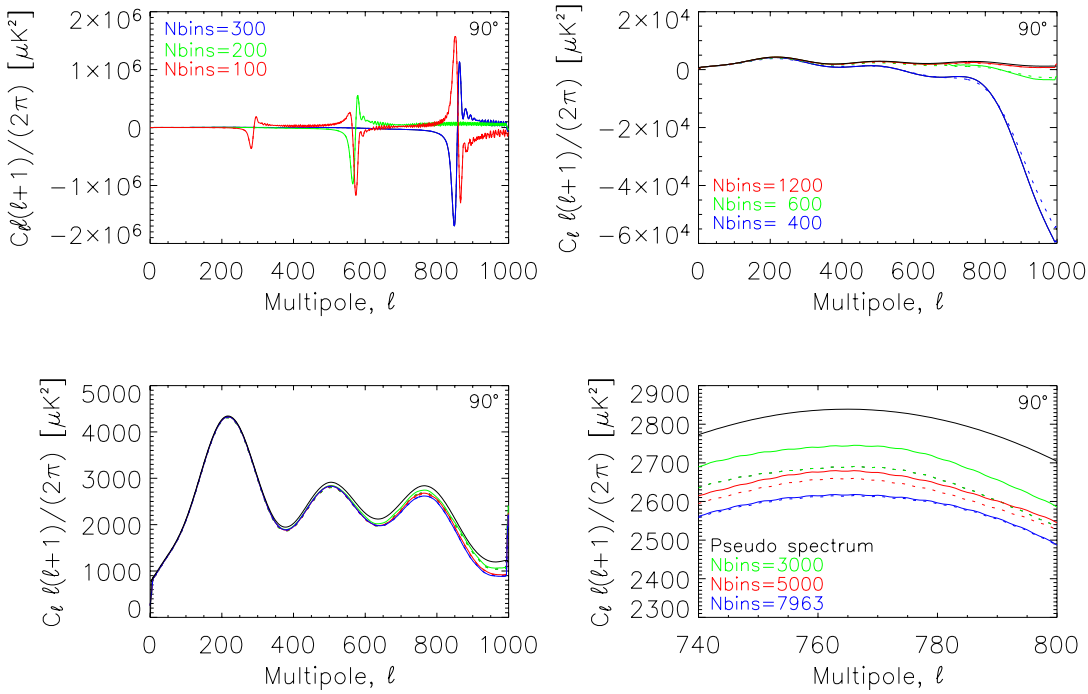

Figure 4.10: Comparison of the binned and unbinned power spectra at 90° sky coverage after convolution for $N_{\rm bins} \leq N_{\rm bins}^{\rm opt}$ ($N_{\rm bins}^{\rm opt} = 7963, l_{\rm max} = 1000, N_{\rm conv} = N_{\rm conv}^{\rm opt}$). The upper left panel shows the binned and the unbinned power spectra for $N_{\rm bins} \leq 0.05 N_{\rm bins}^{\rm opt} \lll N_{\rm bins}^{\rm opt}$. Practically all information about the input spectrum has been lost, and hence it is impossible to retrieve any of the original information about the spectrum. The upper right panel shows the two spectra for $N_{\rm bin} \leq 0.15 N_{\rm bins}^{\rm opt} \ll N_{\rm bins}^{\rm opt}$, where the spectra begin to resemble the input spectrum, though the information about the higher l's is still lost. In the lower left panel, the two-point spectra with $N_{\rm bins} = 3000$ (green), $N_{\rm bins} = 5000$ (red) and $N_{\rm bins} = N_{\rm bins}^{\rm opt} = 7963$ (blue) are plotted against the pseudo spectrum (black). As expected the rederived spectra have less power than the input spectrum, but all features from the input spectrum are now retrieved. The lower right panel shows a close up the spectra in the lower left panel for multipoles $l = [740, 800]$, and here we get a clear demonstration of how the two rederived spectra move towards each other and at the same time away from the input spectrum.

when $N_{\rm bins}^{\rm opt} \gg N_{\rm bins}$, the average bin size is so large compared to the smallest angular separations of the pixel pairs that the information they carry with them is completely lost, and instead the pixel value is picked more or less at random. This is basically the same as what we found for full sky coverage in Section 4.1.2.

For $N_{\rm bins}$ larger than 15% of $N_{\rm bins}^{\rm opt}$, the two power spectra moved towards each other as the number of bins increased. But as long as $N_{\rm bins} < N_{\rm bins}^{\rm opt}$, the resulting binned power spectrum was lower than the resulting unbinned spectrum (see the two lower panels in Figure 4.10). This was as expected, since more information has been lost in both the calculation of the correlation function and the rederived power spectrum and in the filtering because of the binning, than in the process of obtaining the unbinned rederived spectrum. When the rederived binned and unbinned power spectra only differed by 1% or less $N_{\rm bins} = N_{\rm bins}^{\rm opt}$ per definition, and the two power spectra became visually indistinguishable (see Figure 4.9). But note that as the number of bins increased, the two power spectra do not necessarily move towards the pseudo power spectrum. I have not been able to find an explanation for this behaviour. Because of truncation at both ends of the spectra in the filtering process, the maximum number of multipoles possible to retrieve after filtering is, for any $N_{\rm conv}$, given by

$$l_{\rm retr}^{\rm max} = l_{\rm max} - 2N_{\rm conv} \tag{4.3}$$

and will be in the range $l = [N_{\rm conv}, l_{\rm max} - N_{\rm conv}]$. If the number of bins used is less than the optimal number of bins, *i.e.* $N_{\rm bins} < N_{\rm bins}^{\rm opt}$, then the number of multipoles possible to retrieve after filtering $l_{\rm retr}$ will be less than $l_{\rm retr}^{\rm max}$.

During my work with the running average filtered power spectra I noticed that there seemed to be a relationship between sky coverage, $l_{\rm max}$ and the optimal number of bins. I examined the behaviour of $R_{\rm max}$ and $N_{\rm bins}^{\rm opt}$ a little more closely for $l_{\rm max} = 400, 600$ and 1000, and from the results (see Tables 4.2-4.4) I found the following relationship

$$N_{\rm bins}^{\rm opt} = A\left(\frac{R_{\rm max}}{180^\circ}\right) l_{\rm max}, \tag{4.4}$$

where A is a parameter in the range of [10,20] when the difference between the binned and unbinned filtered power spectra is set to be 1.0% or less, $R_{\rm max}$ is the sky coverage in degrees, $N_{\rm bins}^{\rm opt}$ the number of bins needed to obtain the desired maximum difference between the binned power spectrum, and $l_{\rm max}$ is the maximum multipole value in the input spectrum. In general the number of bins necessary to obtain the desired accuracy increases with $R_{\rm max}$, but note that as $R_{\rm max}$ gets close to 180° then $N_{\rm bins}^{\rm opt}$ decreases even though $R_{\rm max}$ continues to increase. This trend can be seen for all $l_{\rm max}$ (see Tables 4.2-4.4).

For a given sky coverage, Equation (4.4) can be used to find the number of bins necessary to retrieve a given number of multipoles, or to find the highest number of multipoles one can hope to retrieve information about with a given number of bins. In the first case, it is advisable to use $A = 20$ in order to obtain a high enough number of bins, while it in the latter case is more advisable to use $A = 10$ to get a reliable estimate

of $l_{\max}$. Equation (4.4) can also be used to find the smallest sky coverage necessary to obtain information about multipoles up to a given $l_{\max}$ with a given number of bins. In this case we have to use a small value of A, i.e. $A = 20$.

Conclusions

For partial sky coverage the conclusion are the following: As in the case of full sky coverage, the analytical comparison of the binned and the unbinned two-point correlation functions were found to differ most at those scales where the features in the CMB was approximately equal to or smaller than the bin size. The partial sky coverage naturally also caused a cut-off in the correlation function at $\chi = R_{\max}$.

For partial sky coverage the rederived power spectra inhabit strong oscillations induced by the cut-off in the two-point correlation function. These oscillations have to be removed since they mask the information contained in the spectra.

FFT filtering is too cumbersome and inaccurate to be useful for the purpose of removing the oscillations, while a running average filter is much easier. This filtering gives very good results, provided that the filter width is the appropriate filter width for the given sky coverage.

Once the oscillations are removed we can see that, if the input power spectrum is defined up to $l_{\max}$, most of the information in the higher l's are lost if the correlation function is measured with fewer bins than the optimal $N_{\text{bins}} < N_{\text{bins}}^{\text{opt}}$. The optimal number of bins to be used at a given sky coverage in order to retrieve information about the desired number of multipoles is given by Equation (4.4). If $N_{\text{bins}} \gtrsim N_{\text{bins}}^{\text{opt}}$, the rederived power spectra differs very little. But they might still differ severely from the input power spectrum, so in the case of partial sky coverage the binning effect have to be taken into account when the power spectrum is calculated from the correlation function. One way to correct for the binning effect could be to develop a binning window W_b from the relation $C_{l\,\text{Partial sky}}^{\text{Binned}}/C_{l\,\text{Partial sky}}^{\text{Theory}}$, but due to time limitations this has not been looked into in this thesis.

$R_{max}[^\circ]$	$N_{\rm bins}^{\rm opt}$	A
20	852	19.17
30	1330	19.95
45	1976	19.76
60	2490	18.68
90	3485	17.43
120	4511	16.92
135	4657	15.52
150	4798	14.39
170	4365	11.55

Table 4.2: Relation between sky coverage, the number of bins necessary to obtain the desired accuracy and the parameter A for $l_{\rm max} = 400$.

$R_{\rm max}[^\circ]$	$N_{\rm bins}^{\rm opt}$	A
20	1206	18.09
30	1795	17.95
45	2709	18.06
60	3600	18.00
90	5399	18.00
120	6000	15.00
135	6499	14.44
150	6547	13.09
170	5914	10.44

Table 4.3: Relation between sky coverage, the number of bins necessary to obtain the desired accuracy and the parameter A for $l_{\rm max} = 600$.

$R_{\rm max}[^\circ]$	$N_{\rm bins}^{\rm opt}$	A
20	2010	18.09
30	2300	13.80
45	3401	13.60
60	6001	18.00
90	7963	15.93
120	9035	13.55
135	10197	13.60
150	10309	12.37
170	9593	10.16

Table 4.4: Relation between sky coverage, the number of bins necessary to obtain the desired accuracy and the parameter A for $l_{\rm max} = 1000$.

Chapter 5

Preparing for maximum likelihood analysis

In this chapter I will first give a brief general introduction to the maximum likelihood method, the basic concepts connected to this method and how they are related to the two-point correlation function. Then I develop a general analytical expression for the covariance matrix, before I develop analytical expressions for the covariance matrix for the two-point correlation functions. At the end of the chapter I comment on the effect of the altered power spectrum on the covariance function, before I draw some lines for future work on the possible use of the two-point correlation functions in CMB analysis.

5.1 Introduction

Most of this introduction is based on a paper by Douspis et al. (2001).

The extraction of information from the CMB is a classic problem of model testing and parameter estimation, one of the main goals being to constrain the cosmological parameters from an assumed model and to decide if the best fit parameter values is a good description of the data.
CMB analysis can be divided into four levels, each with a more compressed data set than at the previous level:

1. Time series of data (TODs)
2. Pixel maps
3. Power spectrum
4. Cosmological parameters

We could in principle develop a method that would take us directly from 1) to 4), but the step-by-step approach is found to give more information because each level is found to contain interesting information about the CMB, not just about the cosmological

parameters, but also on fields like non-Gaussianity and nucleosynthesis. In this thesis I have chosen to focus on how to get from from 2) to 3) in the analysis, examining whether the two-point correlation function might offer a useful intermediate step between pixel maps and the power spectrum.

The power spectrum has become the standard way of reporting CMB results, both because it is a very good visual way to understand the data and because it is what is actually calculated in the cosmological models. It has also become generally excepted in the CMB community as the intermediate step from pixel representation to the parameter room, since there in principle is no loss of information when using the second order moments as a "radically compressed" representation of the pixel data, provided that the CMB temperature fluctuations are Gaussian (Bond et al., 2000). In many ways the power spectrum is an interesting result on its own, but it is also needed in other CMB analyses.

One of the methods often used for analysis of CMB data is the maximum likelihood method, but estimating the power spectrum directly from pixel data using this method is complicated by the complexity of the model calculations and not least by the size of the data sets (Bond et al., 1998). The million-pixel maps from WMAP and from the upcoming Planck experiment are too large to be analysed by this method in any practical way. Using maximum likelihood analysis directly on the pixel data simply takes up too much CPU-time even on the fastest computers available today, so there is a strong need to find more efficient methods. Over the last decade much effort has been put into this field in search for such methods (see *e.g.* Bond et al., 2000; Wandelt et al., 2001; Wandelt and Hansen, 2003).

Almost without exception, the present methods use band-power estimates as their starting points. Band-power is simply signal power over a finite range of multipoles, and is commonly estimated with likelihood analysis. The problem is that a set of band-powers do not fully describe the data (Douspis et al., 2001). The correlation function can be calculated directly from the pixel maps without using maximum likelihood, and in principle also without loss of information, which gives the correlation function an advantage compared with the power spectrum. The fact that the correlation function is rotationally invariant does also come in extremely handy when dealing with partial sky coverage, where power spectrum estimation suffer from bias and the effect of coupled a_{lm}'s.

5.1.1 General functions and properties

The common approach to CMB analysis is, as mentioned above, through the maximum likelihood method. In this method the probability distribution of the data is maximised as a function of the model parameters, given the observed data set. Once found, the best model is then tested on its ability to account for the data. This is a very general method for statistical analysis which is not particularly connected to the CMB, but

has since the early days of anisotropy searches been found to be very useful in CMB research (Readhead et al., 1989; Bond et al., 1991; Dodelson and Jubas, 1993).

The maximum likelihood method is based on a fundamental tool in statistical analysis called the likelihood function $\mathcal{L}$. Given a set of data, the likelihood function relates the predictions of a particular model to the observations: The best possible estimate of the set of parameters obtained from the data, is the set of parameters that gives the largest $\mathcal{L}$, *i.e.* the set Θ that maximises the likelihood function, hence the name of the method.

The likelihood function is simply the probability density function (pdf) for obtaining a set of observed data, represented by a data vector $\mathbf{d}$, given a set of parameters Θ that we wish to constrain

$$\mathcal{L}(\Theta) \equiv \mathrm{Pdf}(\mathbf{d}|\Theta). \tag{5.1}$$

Since we are working with the transition from level 2) to level 3) in the CMB analysis, $\mathbf{d}$ represents the set of N_{pix} observed sky temperatures or temperature differences (*i.e.* the map) and the parameters we wish to constrain is the power spectrum. Hence the likelihood in our case can be written

$$\mathcal{L}(\Theta) \equiv \mathrm{Pdf}(\mathbf{d}|C_l) \tag{5.2}$$

Likelihood functions can be constructed for all types of statistical distributions, but the many favourable properties of Gaussian distributions make Gaussian maximum likelihood analysis desirable. One particularly favourable feature of Gaussian distribution is the fact that the variates are independent, and hence only need to be computed once, which saves a lot of time compared with distributions where the variates are dependent and have to be computed for each entry in the ensemble.

Since inflation predicts Gaussian temperature fluctuations, the observed pixel temperatures are expected to be well described by random variables following a multivariate Gaussian distribution, with a covariance matrix that is given as a function of the power spectrum, in addition to a noise term.

The covariance function is simply the second order statistical moments of the temperature fluctuations, *i.e.* the two-point correlation function. If we use the spherical harmonic coefficients a_{lm} found from the pixel maps to calculate the power spectrum, then C_l is also second order moments of the temperature fluctuations. For Gaussian theories these second order moments are all that is needed to construct the appropriate likelihood function $\mathcal{L}$. It is through the dependence of the covariance matrix C on $C(\chi)$ that the power spectrum C_l enters the likelihood.

Assuming that the data have a multivariate Gaussian distribution, the likelihood function is given by

$$\mathcal{L}(\Theta) = \frac{e^{-\frac{1}{2}\mathbf{d}^T\cdot \mathrm{C}^{-1}\cdot\mathbf{d}}}{(2\pi)^{N_{\mathrm{pix}}/2}(\det \mathrm{C})^{1/2}}, \tag{5.3}$$

where C is the pixel-pixel covariance matrix

$$\mathrm{C}_{ij} \equiv \langle d_i d_j \rangle = C(\chi)_{ij}^{\mathrm{signal}} + N_{ij}. \tag{5.4}$$

The average is taken over the theoretical ensemble of all possible universes realizable with the same set of parameters. The signal part of the covariance matrix, $C(\chi)_{ij}^{\text{signal}}$, is the two-point correlation functions reviewed and developed in Section 2.4 and Chapter 3. Having assumed Gaussian, *i.e.* uncorrelated, noise, the noise contribution to the covariance matrix, N_{ij}, is diagonal.

The main problem when computing (5.3), is the extremely time consuming computation of the inverse covariance matrix, C^{-1}. For WMAP the covariance is a $3 \cdot 10^6 \times 3 \cdot 10^6$ matrix, and an iterative inversion of this matrix alone takes a million years. For Planck, the same matrix is $5 \cdot 10^7 \times 5 \cdot 10^7$, and since matrix inversion scales as $\mathcal{O}(\mathrm{N}^3)$, the inversion will take approximately $4 \cdot 10^9$ years! Cosmologists are in other words in strong need of faster methods to find the power spectrum from the pixel maps.

5.2 Parameter estimation with compressed data sets

Once the power spectrum is estimated, the Monte Carlo Markov Chains method is used to estimate the cosmological parameters. Ideally maximum likelihood would have been used to estimate the parameters, but Markov Chains are faster, simpler and give very good results (Christensen et al., 2001; Verde, 2003). With Monte Carlo Markov Chains the transition from the power spectrum to parameter space is considered to be solved (Christensen et al., 2001). So the critical issue is to find a fast and precise transition from pixel representation to representation through the power spectrum.

One possible solution, which is the motivation behind this thesis, might be found in the two-point correlation function, since the two-point function is the real-space equivalent of the power spectrum, and there in principle is no loss of information when going from one of these two second order statistical moments to the other. If this is to be an attractive way to estimate the power spectrum, then the calculation of C_l from the two-point correlation function have to be efficient and give good results. To estimate the power spectrum using direct integration of the two-point correlation function, like I did in Chapter 4, might introduce bias. The maximum likelihood method do not, which is why we wish to use this method to estimate the power spectrum.

There are two effects that can make the two-point correlation function highly undesirable, or even unfit, for these calculations. First, if the two-point function has a non-Gaussian distribution, we will have to use a non-Gaussian likelihood function where the variates are correlated. These variates will then have to be estimated iteratively, which is time consuming and would make the correlation function a highly undesirable intermediate step.

Second, if the covariance matrix is singular then the covariance matrix will be non-invertible no matter how small it is. With the compressed data set that the binned correlation function form, the covariance matrix can be reduced to a $\lesssim 10^4 \times 10^4$ matrix, which is considerably less time-consuming to invert than the full pixel-pixel covariance

matrix. Since matrix inversion scales as $\mathcal{O}(\mathrm{N}^3)$, inverting the two-point two-point correlation matrix M will take a maximum of 280 hours, or less than 12 days. But this does not matter much if we are not be able to perform the maximum likelihood analysis at all.

The questions of statistical distribution and inversion of the covariance function will be investigated in more detail in Section 5.3 and 5.5 respectively, but for as long I will assume that the correlation function is both Gaussian distributed and non-singular.

5.2.1 The likelihood functions

Using the two-point function to constrain the power spectrum, the likelihood function is defined as

$$\mathcal{L}(C_l) \equiv \mathrm{Pdf}(C(\chi)|C_l). \tag{5.5}$$

Here $C(\chi)$ is the two-point correlation function calculated for N_{bins} different angles χ_i from the pixel map. The likelihood function is then

$$\mathcal{L}(C_l) = \frac{e^{-\frac{1}{2}C(\chi)^T \cdot \mathrm{M}^{-1} \cdot C(\chi)}}{(2\pi)^{N_{\mathrm{bins}}/2}(\det \mathrm{M})^{1/2}}, \tag{5.6}$$

where M is the two-point two-point covariance matrix

$$\mathrm{M}_{ij} \equiv \langle C(\chi)_i C(\chi)_j \rangle = M_{ij}^{\mathrm{signal}} + N_{ij}. \tag{5.7}$$

The average is taken over the theoretical ensemble of all possible universes realizable with the same power spectrum. The signal part of the covariance, M_{ij}^{signal}, can be expressed as a function of the power spectrum, while the noise contribution to the covariance matrix, N_{ij}, is diagonal. Explicit functions for $\mathrm{M}_{ij}^{\mathrm{signal}}$ will be developed in Section 5.4.

Partial sky coverage

In the sections above full sky coverage have been assumed. As mentioned earlier, the spherical harmonic coefficients a_{lm} become coupled in the case of partial sky coverage, and the likelihood function must be rewritten (Douspis et al., 2001)

$$\mathcal{L}(\Theta) \equiv \mathrm{Prob}(\tilde{d}|\Theta) \propto \frac{e^{-\frac{1}{2}\tilde{d}^T \cdot \left[C(\chi)^{\mathrm{partial}} + \tilde{\mathbf{N}}\right]^{-1} \cdot \tilde{d}}}{|C(\chi)^{\mathrm{partial}} + \tilde{\mathbf{N}}|^{1/2}}, \tag{5.8}$$

where $\tilde{d}$ is

$$\tilde{\mathbf{d}} = \Omega_{pix} \mathbf{\Psi}^T \cdot \mathbf{d}. \tag{5.9}$$

Here Ω_{pix} represents the the solid angle subtended by the pixel elements, and $\mathbf{\Psi}$ is the new basis functions made of linear combinations of the orthonormal set of spherical harmonic functions Y_{lm} that spans the full sphere.

The noise is given by

$$\tilde{\mathbf{N}} = \Omega_{pix}^2 \mathbf{\Psi}^T \cdot \langle \mathbf{d} \cdot \mathbf{d}^T \rangle \cdot \mathbf{\Psi}. \tag{5.10}$$

Using the two-point correlation function as a compressed representation of the pixel data and assuming a multivariate Gaussian distribution, the likelihood function used to estimate the power spectrum is written

$$\mathcal{L}(C_l) \equiv \text{Prob}(C(\chi)_{\text{partial}}|C_l) \propto \frac{e^{-\frac{1}{2}C(\chi)^T_{\text{partial}}\cdot\left[C(\chi)^{partial}+\tilde{\mathbf{N}}\right]^{-1}\cdot C(\chi)_{\text{partial}}}}{|C(\chi)^{\text{partial}}+\tilde{\mathbf{N}}|^{1/2}}, \tag{5.11}$$

where $C(\chi)_{\text{partial}}$ is the estimated two-point function, and the noise is diagonal. Analytical expressions for the covariance matrix M_{ij}^{partial} will be derived later in Section 5.4.

Equation (5.11) is a lot simpler to work with than Equation (5.8) since the partial sky coverage is incorporated in the correlation functions, and we hence do not have to define a new basis to correct for this. The same is the case for binning, so using the two-point function is less likely to suffer from bias and coupling of the a_{lm}'s.

5.3 Statistical distribution

If there is to be any point in using the two-point correlation function in CMB analysis, we need the computations of the power spectrum to be fast and to give good results. Both these requirements can be achieved using the Gaussian maximum likelihood method, but before using this method, we have to be certain that the distribution truly is Gaussian. Thus in this section I examine the distribution of the two-point function.

5.3.1 Full sky coverage

To investigate the statistical distribution of the two-point correlation function, I first simulated 10.000 maps with a resolution of $N_{\text{side}} = 128$, using the the map-making routine in *correlations.pl* of the Correlation Suite. I then used the *structures* and the *twopt_calc_element* routines of the Suite to calculate the values of the two-point correlation function at three different angles, $\chi = 0.6°, 1.0°$ and $3.6°$, corresponding to the multipoles $l = 50, 200$ and 300. The angles were chosen so that I checked the distribution of $C(\chi)$ at the area around the first peak, the first through and the low-l Sachs-Wolfe plateau. The results are shown in Figure 5.1.

From Figure 5.1 it was easy to see that the two-point function did not have the favourable Gaussian distribution, but were instead χ^2-distributed (see the upper panels in Figure 5.1). If we take a look at the analytical expressions in Equation (2.29) and (3.19), this is not really a surprise. Knowing that C_l is quadratic (with $2l+1$ degrees of freedom) and that $(2l+1)\cdot C_l$ goes as l^{-1}, it is easy to see that the χ^2-distribution of the lower multipoles will be dominating the Gaussian distribution of the higher multipoles. Hence the total two-point correlation function also becomes χ^2-distributed.

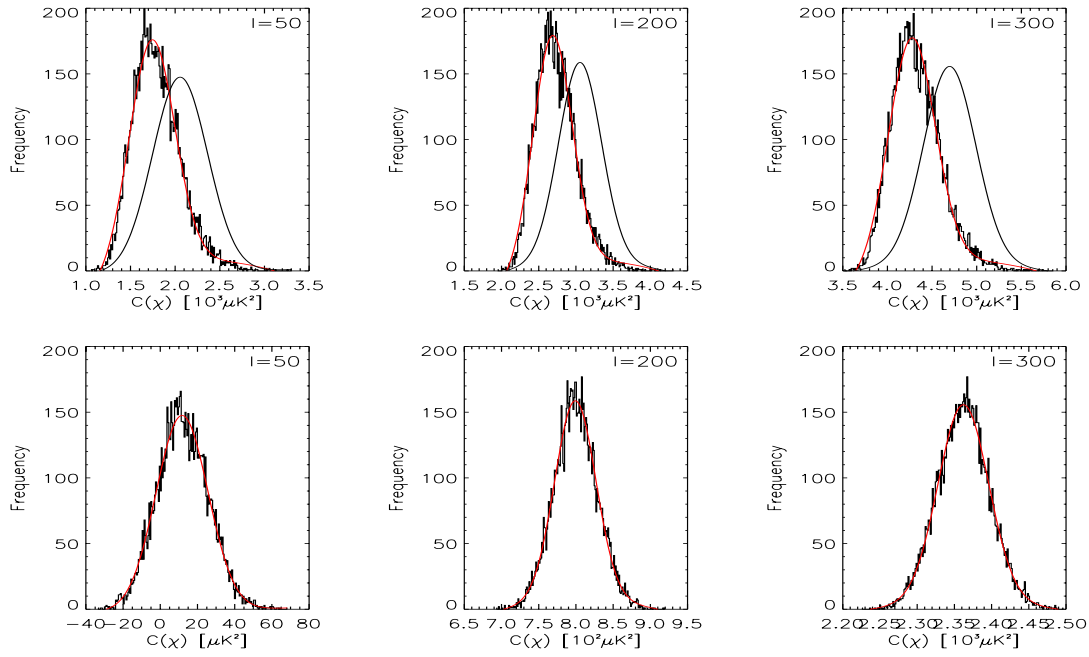

Figure 5.1: Statistical distribution of $C(\chi)$ at given angles χ with full sky coverage. The histograms in the upper panels show the statistical distribution of $C(\chi)$ at $\chi = 3.6°(l = 50), 1.0°(l = 200)$ and $0.6°(l = 300)$. The χ^2-fit to the distributions are plotted in red, and the solid black lines are the distributions expected if $C(\chi)$ had been Gaussian distributed. The χ^2-distribution is shown to be a good fit to the data. The histograms in the lower panels show the statistical distribution of $C(\chi)$ at the same angles after the multipoles $l = [0, 20]$ have been removed from the input spectrum. Here the red lines are the Gaussian fit to the distributions. The Gaussian distribution is shown to be a very good approximation to the data after the removal of the lower multipoles.

But if the two-point correlation function was to be used in a Gaussian maximum likelihood analysis, it had to be Gaussian distributed. Since the χ^2-distribution comes from the lower multipoles which are already well known from previous experiments like COBE, and the information we seek is contained in the higher multipoles, I decided to try to remove the multipoles $l = 0 - 20$ from the input power spectrum and look at the distribution again. This I could do because a continuous, asymmetric distribution with a single peak and not to heavy tail, like the χ^2, is well approximated by a Gaussian distribution for 60 or more degrees of freedom (Bhattacharyya and Johnson, 1977). In the case of the two point correlation function, I only needed 40 degrees of freedom for the Gaussian distribution to be a good approximation. A comparison of the two-point correlation function resulting from the original and the altered input power spectrum is shown in Figure 5.2. As can be seen in the figure, the removal of the multipoles

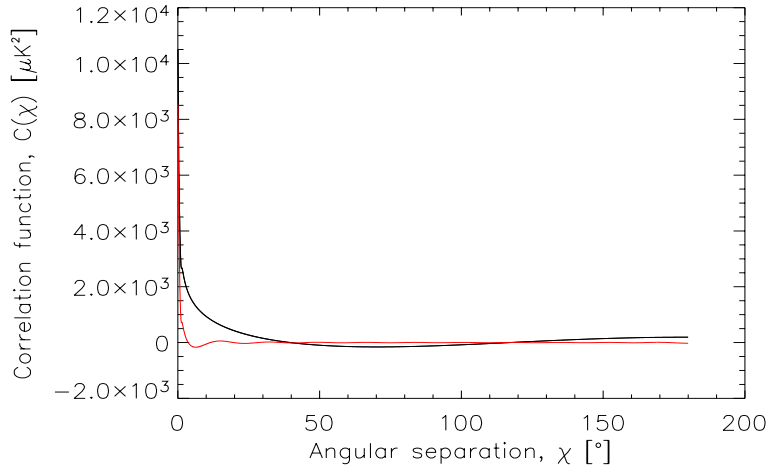

Figure 5.2: Plot comparing the two-point correlation function $C(\chi)$ calculated from the original input power spectrum (black) and the same function calculated from an input spectrum where the multipoles $l = [0, 20]$ have been removed (red), in the case of full sky coverage. In the two-point function resulting from the altered input spectrum, the features are compressed and shifted towards smaller angles and the decline at the very smallest angles is steepened.

results in a correlation function where the features are compressed and shifted towards smaller angles, and where the decline at the very smallest angles is steepened.

Once again I simulated 10.000 maps, but this time with the altered input spectrum. Then I calculated the two-point function for the same angles χ as for the maps with the original input spectrum. A comparison of the analytical full sky two-point correlation function $C(\chi)$ calculated with the original and the altered power spectrum, can be seen in Figure 5.2, while the resulting distribution after the removal of the first twenty multipoles can be seen in the lower panels of Figure 5.1. When I looked at the statistical distributions this time, it was very close to Gaussian.

5.3.2 Partial sky coverage

I used almost the same approach to find the statistical distribution of $C(\chi)$ in the case of partial sky coverage, as in the case of full sky coverage: I simulated 10.000 maps with $N_{\rm side} = 128$ using the original, unaltered input power spectrum, calculated the two-point function at $\chi = 0.6°, 1.0°$ and $3.6°$. But since I was interested in looking at the distribution of $C(\chi)$ at various degrees of sky coverage, I also used the *genmask* routine of H.K.K. Eriksen's Correlation Suite to generate masks fitting sky coverage in the range $R_{\rm max} = [20°, 170°]$. The distributions of $C(\chi)$ with partial sky coverage can be seen in Figure 5.3. As expected from both the results for full sky coverage and the shape of the two-point correlation functions in Equations (3.40) and (3.52), the

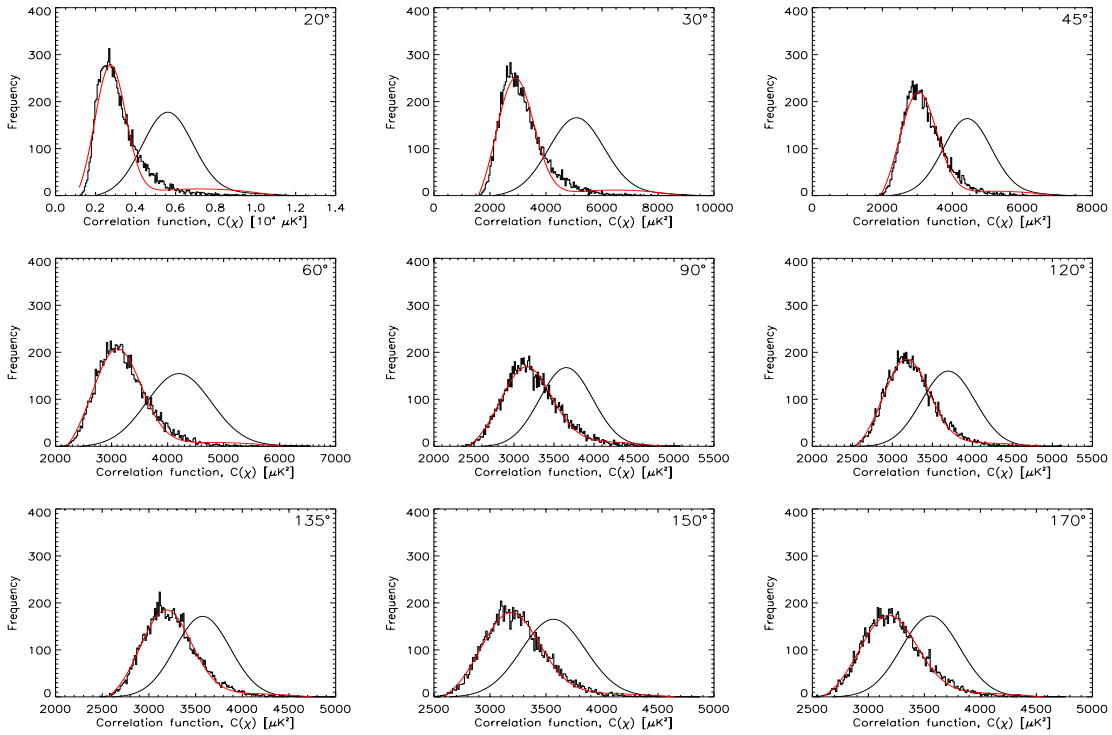

Figure 5.3: Statistical distribution of $C(\chi)$ at partial sky coverage. The histograms show the distribution of $C(\chi)$ at the angle $\chi = 1^\circ$ ($l = 200$) for different values of $R_{\max}$. The red lines are the χ^2-fit to the distributions, and the solid black lines are the distributions expected if $C(\chi)$ had been Gaussian distributed. The χ^2-distribution is shown to be a good fit to the data.

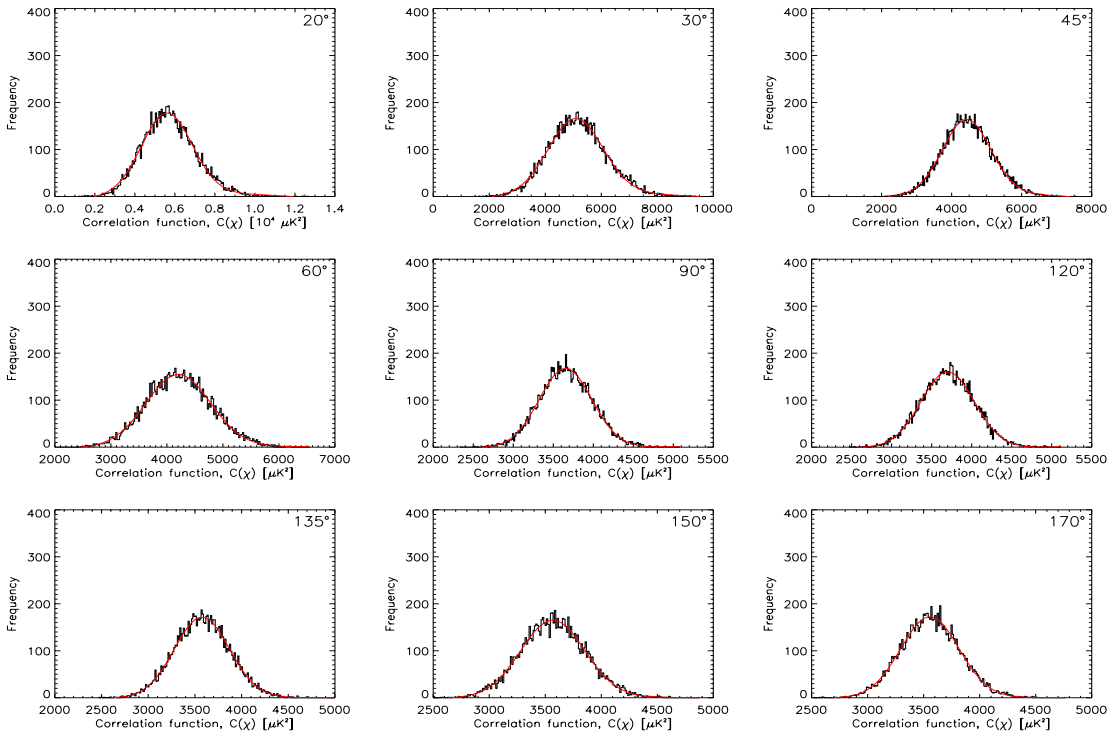

Figure 5.4: Statistical distribution of $C(\chi)$ after the multipoles $l = [0, 20]$ have been removed from the input spectrum. The histograms show the distribution of $C(\chi)$ at the angle $\chi = 1°$ ($l = 200$) for different values of $R_{\max}$. The red lines are the Gaussian fit to the distributions, and shows that the Gaussian distribution is a very good approximation to the data after the removal of the lower multipoles.

distributions were χ^2 also in this case.

In an effort to make probability distributions Gaussian, I once again removed the multipoles l=[0,20] from the input spectrum, simulated 10.000 new maps with the altered input spectrum and examined the distributions again. The resulting distributions can be seen in Figure 5.4. Like in the case of full sky coverage, the removal of the lower multipoles made the distributions clearly indistinguishable from Gaussian distributions.

5.4 The covariance matrix - analytic approach

In this section I derive a general analytic expression for the covariance matrix.

5.4.1 General analytic expression

As the measured correlation function will be fluctuating around an average value and the correlation function in a given point can be written on the form

$$C_i = \langle C_i \rangle + \delta C_i, \tag{5.12}$$

the covariance matrix can be written

$$\begin{aligned} \mathrm{M}_{ij} &= \langle C_i C_j \rangle \\ &= \langle C_i \rangle \langle C_j \rangle + \langle C_i \rangle \langle \delta C_j \rangle + \langle \delta C_i \rangle \langle C_j \rangle + \langle \delta C_i \delta C_j \rangle \\ &= \langle C_i \rangle \langle C_j \rangle + \langle \delta C_i \delta C_j \rangle, \end{aligned} \tag{5.13}$$

since $\langle \delta C_i \rangle = 0$.

5.4.2 The covariance matrix of the correlation functions

In this section I develop analytical expressions for the covariance matrix to be used in a maximum likelihood analysis to extract the true power spectrum from the observed pseudo-power spectrum.

Full sky coverage

The covariance matrix in the case of full sky coverage is given by:

$$\mathrm{M}(\chi_1, \chi_2) = \langle C(\chi_1) C(\chi_2) \rangle = \langle \langle T(\Omega_1) T(\Omega_2) \rangle \langle T(\Omega_3) T(\Omega_4) \rangle \rangle, \tag{5.14}$$

where the inner $\langle\rangle$ is the average over the sphere and the outer $\langle\rangle$ is the average over all realizations.

Replacing $\langle C(\chi_i) \rangle$ with Equation (2.24) in (5.14) gives

$$\mathrm{M}(\chi_1, \chi_2) = \frac{1}{(4\pi)^2} \sum_{ll'} P_l(\mu_1) P_{l'}(\mu_2) \sum_{mm'} \langle a_{lm} a^*_{lm} a_{l'm'} a^*_{l'm'} \rangle. \tag{5.15}$$

In order to evaluate the expectation value $\langle a_{lm}a^*_{lm}a_{l'm'}a^*_{l'm'}\rangle$ in Equation (5.15), I apply a well-known result from statistical theory which states that if x_i, $i = 1, 2, 3, 4$, are Gaussian random variables with vanishing mean, then

$$\langle x_i x_j x_k x_l\rangle = \langle x_i x_j\rangle\langle x_k x_l\rangle + \langle x_i x_k\rangle\langle x_j x_l\rangle + \langle x_i x_l\rangle\langle x_j x_k\rangle. \tag{5.16}$$

By using Equation (5.16) on the a_{lm}'s, I find

$$\begin{aligned} \mathrm{M}(\chi_1,\chi_2) &= \frac{1}{(4\pi)^2}\sum_{ll'} P_l(\mu_1)P_{l'}(\mu_2)[\sum_m \langle a_{lm}a^*_{lm}\rangle \sum_{m'}\langle a_{l'm'}a^*_{l'm'}\rangle \\ &+ \sum_{mm'}\langle a_{lm}a_{l'm'}\rangle\langle a^*_{lm}a^*_{l'm'}\rangle + \sum_{mm'}\langle a_{lm}a^*_{l'm'}\rangle\langle a_{l'm'}a^*_{lm}\rangle]. \end{aligned} \tag{5.17}$$

With the power spectrum from Equation (2.28), and the relationship between the power spectrum and the harmonic coefficients given by Equation (2.27), I find that

$$\begin{aligned} \mathrm{M}(\chi_1,\chi_2) &= \frac{1}{(4\pi)^2}\sum_{ll'} P_l(\mu_1)P_{l'}(\mu_2)\left[(2l+1)(2l'+1)C_lC_{l'} + 2C_lC_{l'}\delta_{ll'}\sum_{mm'}\delta_{mm'}\right] \\ &= \frac{1}{(4\pi)^2}\sum_l (2l+1)C_lP_l(\mu_1)\sum_{l'}(2l'+1)C_{l'}P_{l'}(\mu_2) + \frac{1}{8\pi^2}\sum_l C_l^2 P_l(\mu_1)P_l(\mu_2) \end{aligned} \tag{5.18}$$

With the full sky correlation function averaged over all realizations given by Equation (2.27), I get that in the case of full sky coverage, the covariance is

$$\boxed{\mathrm{M}(\chi_1,\chi_2) = \langle C(\chi_1)\rangle\langle C(\chi_2)\rangle + \frac{1}{8\pi^2}\sum_l C_l^2 P_l(\mu_1)P_l(\mu_2).} \tag{5.19}$$

This is precisely the form 'predicted' in Section 5.4.1.

Partial sky coverage - disk-shaped sky patches

Looking at disk-shaped sky patches, the covariance is

$$\mathrm{M}(\chi_1,\chi_2)_{\mathrm{disk}} = \langle C(\chi_1)_{\mathrm{disk}}C(\chi_2)_{\mathrm{disk}}\rangle = \langle\langle T(\Omega_1)T(\Omega_2)\rangle_{\mathrm{disk}}\langle T(\Omega_3)T(\Omega_4)\rangle_{\mathrm{disk}}\rangle \tag{5.20}$$

where $\langle\rangle$ is the average over all realizations, and $\langle\rangle_{\mathrm{disk}}$ is the average taken over the disk-shaped sky patches.

Replacing $C(\chi_i)_{\mathrm{disk}}$ with Equation (3.40) in (5.20), I get

$$\mathrm{M}(\chi_1,\chi_2)_{\mathrm{disk}} = \frac{\sum_{ll'} P_l(\mu_1)P_{l'}(\mu_2)\sum_{mm'}\langle\tilde{a}_{lm}\tilde{a}^*_{lm}\tilde{a}_{l'm'}\tilde{a}^*_{l'm'}\rangle}{D(\chi_1)D(\chi_2)}. \tag{5.21}$$

where $D(\chi_i)$ is given by Equation (3.42).

Since the $\tilde{a}_{lm}$'s are Gaussian random variables I can use Equation (5.16), which gives

$$\begin{aligned} \mathrm{M}(\chi_1,\chi_2)_{\mathrm{disk}} &= \frac{\sum_{ll'} P_l(\mu_1)P_{l'}(\mu_2)}{D(\chi_1)D(\chi_2)} \\ &\times \sum_{mm'} \left[\langle\tilde{a}_{lm}\tilde{a}^*_{lm}\rangle\langle\tilde{a}_{l'm'}\tilde{a}^*_{l'm'}\rangle + \langle\tilde{a}_{lm}\tilde{a}_{l'm'}\rangle\langle\tilde{a}^*_{lm}\tilde{a}^*_{l'm'}\rangle + \langle\tilde{a}_{lm}\tilde{a}^*_{l'm'}\rangle\langle\tilde{a}_{l'm'}\tilde{a}^*_{lm}\rangle\right]. \end{aligned} \tag{5.22}$$

The average pseudo power spectrum is given by Equation (3.43), and in the case of partial sky coverage I have that

$$\langle\tilde{a}_{lm}\tilde{a}^*_{l'm'}\rangle = \sum_{l''} W^m_{ll''}C_{l''}W^{m'}_{l'l''}\delta_{mm'}. \tag{5.23}$$

Here

$$W^{m'}_{l'l''} = A^{m'}_{l'l''}I^{m'}_{l'l''}, \tag{5.24}$$

where $A^{m'}_{l'l''}$ is given by Equation (3.24), and $I^{m'}_{l'l''}$ by Equation (3.25).

Thus the covariance is

$$\mathrm{M}(\chi_1,\chi_2)_{\mathrm{disk}} = \frac{\sum_{ll'} P_l(\mu_1)P_{l'}(\mu_2)}{D(\chi_1)D(\chi_2)} \times \left[(2l+1)(2l'+1)\langle\tilde{C}_l\rangle\langle\tilde{C}_{l'}\rangle + 2\sum_m \left(\sum_{l''} W^m_{ll''}C_{l''}W^m_{l'l''}\right)^2\right], \tag{5.25}$$

where $D(\chi_i)$ is given by Equation (3.42).

For disk-shaped sky patches, the average correlation function is given by Equation (3.52). This gives

$$\mathrm{M}(\chi_1,\chi_2)_{\mathrm{disk}} = \langle C(\chi_1)_{\mathrm{disk}}\rangle\langle C(\chi_2)_{\mathrm{disk}}\rangle + \frac{2\sum_{ll'} P_l(\mu_1)P_{l'}(\mu_2)\sum_m \left(\sum_{l''} W^m_{ll''}C_{l''}W^m_{l'l''}\right)^2}{D(\chi_1)D(\chi_2)}, \tag{5.26}$$

where $W^m_{l'l''}$ is given by Equation (5.24).

Partial sky coverage - ring-shaped sky patches

The covariance in the case of ring-shaped sky patches is given by

$$\mathrm{M}(\chi_1,\chi_2)_{\mathrm{ring}} = \langle C(\chi_1)_{\mathrm{ring}}C(\chi_2)_{\mathrm{ring}}\rangle = \langle\langle T(\Omega_1)T(\Omega_2)\rangle_{\mathrm{ring}}\langle T(\Omega_3)T(\Omega_4)\rangle_{\mathrm{ring}}\rangle \tag{5.27}$$

where $\langle\rangle$ is the average over all realizations, and $\langle\rangle_{\mathrm{ring}}$ is the average over the ring-shaped sky patches.

The derivation of the covariance in the case of ring-shaped sky patches is almost identical to the derivation in the case of disk-shaped sky patches. By replacing $C(\chi)_{\mathrm{ring}}$ from Equation (3.58) in (5.27), I get

$$\mathrm{M}(\chi_1,\chi_2)_{\mathrm{ring}} = \frac{\sum_{ll'} P_l(\mu_1)P_{l'}(\mu_2)}{E(\chi_1)E(\chi_2)} \times \sum_{mm'}\langle\tilde{a}_{lm}\tilde{a}^*_{lm}\tilde{a}_{l'm'}\tilde{a}^*_{l'm'}\rangle, \tag{5.28}$$

where $E(\chi_i)$ is given by Equation (3.60).

Using Equation (5.16) on the $\tilde{a}_{lm}$'s and the pseudo power spectra from Equation (3.37) and (3.59), with $\langle \tilde{a}_{lm}\tilde{a}^*_{l'm'}\rangle$ given by Equation (5.23), the covariance matrix in the case of ring-shaped sky patches becomes

$$\mathrm{M}(\chi_1,\chi_2)_{\mathrm{ring}} = \langle C(\chi_1)_{\mathrm{ring}}\rangle\langle C(\chi_2)_{\mathrm{ring}}\rangle + \frac{2\sum_{ll'} P_l(\mu_1)P_{l'}(\mu_2)\sum_m \left(\sum_{l''} W^m_{ll''}C_{l''}W^m_{l'l''}\right)^2}{E(\chi_1)E(\chi_2)}. \tag{5.29}$$

5.4.3 The covariance matrix for binned correlation functions

Full sky coverage

The covariance matrix for two binned correlation functions in the case of full sky coverage is given by

$$\mathrm{M}(\chi_1,\chi_2)_{\mathrm{binned}} = \langle C(\chi_1)^{\chi_B}_{\chi_A} C(\chi_2)^{\chi_D}_{\chi_C}\rangle \tag{5.30}$$

where the average is taken over all realizations.

From Section 3.1.1 I have that

$$C(\chi)^{\chi_B}_{\chi_A} = \frac{1}{4\pi k_0(\chi)^{\chi_B}_{\chi_A}}\sum_{lm} k_l(\chi)^{\chi_B}_{\chi_A} \mid a_{lm} \mid^2$$

and

$$\langle C(\chi)^{\chi_B}_{\chi_A}\rangle = \frac{1}{4\pi k_0(\chi)^{\chi_B}_{\chi_A}}\sum_{l}(2l+1)C_l k_l(\chi)^{\chi_B}_{\chi_A}.$$

Using these two equations and the same approach as in the Section 5.4.2, I get

$$\mathrm{M}(\chi_1,\chi_2)_{\mathrm{binned}} = \langle C(\chi_1)^{\chi_B}_{\chi_A}\rangle\langle C(\chi_2)^{\chi_D}_{\chi_C}\rangle + \frac{\sum_l C_l^2 k_l(\chi_1)^{\chi_B}_{\chi_A} k_l(\chi_2)^{\chi_D}_{\chi_C}}{8\pi^2 k_0(\chi_1)^{\chi_B}_{\chi_A} k_0(\chi_2)^{\chi_D}_{\chi_C}}. \tag{5.31}$$

Partial sky coverage - disk-shaped sky patches

The covariance matrix for two binned correlation functions in the case of disk-shaped sky patches is given by

$$\mathrm{M}(\chi_1,\chi_2)_{\mathrm{binned\ disk}}\langle = C(\chi_1)^{\chi_B}_{\chi_A,\mathrm{disk}} C(\chi_2)^{\chi_D}_{\chi_C,\mathrm{disk}}\rangle. \tag{5.32}$$

From Section 3.2.2 I have that

$$C(\chi)^{\chi_B}_{\chi_A,disk} = \frac{\sum_{lm}(2l+1)k_l(\chi)^{\chi_B}_{\chi_A}|\tilde{a}_{lm}\tilde{a}^*_{lm}|^2}{2\pi D(\chi)^{\chi_B}_{\chi_A}}$$

and

$$\langle C(\chi)^{\chi_B}_{\chi_A,disk}\rangle = \frac{\sum_l(2l+1)k_l(\chi)^{\chi_B}_{\chi_A}\sum_m\langle\tilde{a}_{lm}\tilde{a}^*_{lm}\rangle}{2\pi D(\chi)^{\chi_B}_{\chi_A}}.$$

Using these two equations, I get

$$\begin{aligned} \mathrm{M}(\chi_1,\chi_2)_{\text{binned disk}} &= \langle C(\chi_1)^{\chi_B}_{\chi_A,disk}\rangle\langle C(\chi_2)^{\chi_D}_{\chi_C,disk}\rangle \\ &+ \frac{\sum_{ll'} k_l(\chi_1)^{\chi_B}_{\chi_A} k_{l'}(\chi_2)^{\chi_D}_{\chi_C} \sum_m \left(\sum_{l''} W^m_{ll''} C_{l''} W^m_{l'l''}\right)^2}{4\pi^2 D(\chi_1)^{\chi_B}_{\chi_A} D(\chi_2)^{\chi_D}_{\chi_C}}. \end{aligned} \quad (5.33)$$

Partial sky coverage - ring-shaped sky patches

The covariance for two binned correlation functions in the case of ring-shaped sky patches is given by

$$\mathrm{M}(\chi_1,\chi_2)_{\text{binned ring}} = \langle C(\chi_1)^{\chi_B}_{\chi_A,\text{ring}} C(\chi_2)^{\chi_D}_{\chi_C,\text{ring}}\rangle, \quad (5.34)$$

where the average is taken over all realizations.

From Section 3.2.3 I have that

$$C(\chi)^{\chi_B}_{\chi_A,\text{ring}} = \frac{\sum_{lm} k_l(\chi)^{\chi_B}_{\chi_A} |\tilde{a}_{lm}|^2}{2\pi E(\chi)^{\chi_B}_{\chi_A}}$$

and

$$\langle C(\chi)^{\chi_B}_{\chi_A,\text{ring}}\rangle = \frac{\sum_{lm} k_l(\chi)^{\chi_B}_{\chi_A} \langle a_{lm} a^*_{l''m}\rangle}{2\pi E(\chi)^{\chi_B}_{\chi_A}},$$

where $k_l(\chi)^{\chi_B}_{\chi_A}$ is given by Equation (3.11) and $E(\chi_i)^{\chi_B}_{\chi_A}$ by Equation (3.60).

Using the same approach as in the sections above, I get that

$$\begin{aligned} \mathrm{M}(\chi_1,\chi_2)_{\text{binned ring}} &= \langle C(\chi)^{\chi_B}_{\chi_A,\text{ring}}\rangle\langle C(\chi)^{\chi_D}_{\chi_C,\text{ring}}\rangle \\ &+ \frac{\sum_{ll'} k_l(\chi_1)^{\chi_B}_{\chi_A} k_{l'}(\chi_2)^{\chi_D}_{\chi_C} \sum_m \left(\sum_{l''} W^m_{ll''} C_{l''} W^m_{l'l''}\right)^2}{4\pi^2 E(\chi_1)^{\chi_B}_{\chi_A} E(\chi_2)^{\chi_D}_{\chi_C}}. \end{aligned} \quad (5.35)$$

5.5 Conclusions

Both in the case of full and partial sky coverage, I found that the two-point correlation function had a χ^2-distribution around its mean for each bin. Since C_l is quadratic and $(2l+1)\cdot C_l$ goes as l^{-1}, it is easy to see from the analytical expressions for the two-point correlation functions that the χ^2-distribution of the lower multipoles will be dominating the Gaussian distribution of the higher multipoles, and the total two-point function hence will be χ^2-distributed.

From χ^2 to Gaussian distribution

By removing the multipoles that dominated the distribution, *i.e.* $l = [0, 20]$, from the input power spectrum, the two-point functions became indistinguishable from Gaussian distributions.

With the alteration of the input spectrum, the features of the correlation function became compressed and shifted towards smaller angles, and the decline at the very smallest angles became correspondingly steepened. What consequences this alteration might have for the maximum likelihood analysis have to be looked into in further work.

It is possible to perform a χ^2 maximum likelihood analysis using the correlation function with the unaltered input power spectrum, but it would be much more time consuming compared to perform a Gaussian maximum likelihood analysis, because in the χ^2 case the variates are coupled and have to be calculated iteratively.

The covariance matrix M

If the exclusion of the first 20 multipoles from the calculations of the two-point correlation function is found to have no effect on the maximum likelihood analysis, the possible use of the correlation function in CMB analysis looks promising.

But before we can make a final conclusion on this subject we have to take a closer look at the covariance matrix M. If the $\langle C_i \rangle \langle C_j \rangle$ term in M is non-singular and dominates over the $\langle \delta C_i \delta C_j \rangle$ term, then the overall covariance matrix is non-singular and the correlation function can be used to estimate the power spectrum using maximum likelihood.

If the $\langle C_i \rangle \langle C_j \rangle$ term in M_{ij} is singular and also dominates over the $\langle \delta C_i \delta C_j \rangle$ term, then the overall covariance matrix becomes singular and it will be impossible to use maximum likelihood to estimate the power spectrum from the correlation function. In that case the correlation function will be highly unfit for use in CMB analysis through the maximum likelihood method.

Chapter 6

Summary

After much work I have finally arrived at the end of this thesis, and it is time to take a look at what I have accomplished.

6.1 A short review of the thesis

First lets take a short review of the main subjects of this thesis.

6.1.1 The two-point correlation function

I have developed analytical expressions for the two-point correlation function in the cases of limited sky coverage and of binned data.

In the case of full sky coverage the two-point correlation function is (Peebles, 1973)

$$\langle C(\chi)\rangle = \frac{1}{4\pi}\sum_l (2l+1)C_l P_l(\cos\chi),$$

while the equivalent two-point correlation function at partial sky coverage is given by

$$\langle C(\chi)_{\rm disk}\rangle = \frac{\sum_l (2l+1)\langle\tilde{C}_l\rangle P_l(\cos\chi)}{D(\chi)},$$

where $\tilde{C}_l$ is the pseudo power spectrum defined by E. Hivon, B. Wandelt and K. Gorski (Wandelt et al., 2001)

$$\tilde{C}_l = \frac{1}{2l+1}\sum_m \tilde{a}_{lm}\tilde{a}^*_{lm},$$

and the pseudo spherical harmonic coefficients $\tilde{a}_{lm}$ is given by

$$\tilde{a}_{lm} = \sum_{l'm'} a_{l'm'}\int_{\delta\Omega} Y_{l'm'}(\Omega)Y^*_{lm}(\Omega)d\Omega.$$

In the case of azimuthal symmetry $D(\chi)$ is

$$D(\chi) = \pi \left[(\cos r - 1)^2 + \sin^2 r \sum_{l=1}^{\infty} (2l+1) P_l(\cos\chi) \left[P_{l,-1}(\cos r) \right]^2 \right].$$

Note that all dependence on the geometry of the surface area $\delta\Omega$ of the observed sky patch is contained in the pseudo spherical harmonic coefficients $\tilde{a}_{lm}$.

In the case where the data are binned the two-point correlation function at full sky coverage is

$$\langle C(\chi)_{\chi 1}^{\chi 2} \rangle = \frac{1}{4\pi k_0} \sum_l (2l+1) C_l k_l^{\mu_2}{}_{\mu_1},$$

where the coefficient k_l is given by

$$k_l^{\mu_2}{}_{\mu_1} \equiv \frac{4\pi}{2l+1} b_l^{\mu_2}{}_{\mu_1}.$$

The equivalent two-point correlation function at partial sky coverage is given by

$$\langle C(\chi)_{\chi 1,\mathrm{disk}}^{\chi 2} \rangle = \frac{\sum_l (2l+1) \langle \tilde{C}_l \rangle k_l^{\mu_2}{}_{\mu_1}}{2\pi D(\chi)_{\mathrm{bin}}},$$

where $D(\chi)_{\mathrm{bin}}$ in the case of azimuthal symmetry is

$$D(\chi)_{\mathrm{bin}} = \pi \left[k_0^{\mu_2}{}_{\mu_1} (\cos r - 1)^2 + \sin^2 r \sum_{l=1}^{\infty} (2l+1) k_l^{\mu_2}{}_{\mu_1} [P_{l,-1}(\cos r)]^2 \right].$$

At both full and partial sky coverage analytical comparisons of the binned and the unbinned two-point correlation functions showed that the largest differences between the two correlation functions appeared at small scales, since the bins have little sensitivity to features smaller than the bin size. At partial sky coverage the limited sky coverage naturally also caused a cut-off in the correlation function at $\chi = R_{\mathrm{max}}$.

Apart from the positive effect of increasing the number of bins, it was difficult to read out any informative trends or details about the binning effect from the two-point functions.

6.1.2 The rederived power spectrum

To obtain a more 'easy-to-read' picture of the binning effect, I numerically rederived the power spectra from the correlation functions, using Gauss-Legendre integration.

For full sky coverage, if the input power spectrum is defined up to l_{max}, most of the information in the higher l's are lost if the correlation function is measured with $N_{\mathrm{bins}} < l_{\mathrm{max}}$. If $N_{\mathrm{bins}} \gtrsim 4 l_{\mathrm{max}}$, the rederived power spectrum differs very little from

the input power spectrum, hence the binning effect need not be taken into account. But for $l_{\max} \leq N_{\text{bins}} \leq 4l_{\max}$, the binning effect results in suppression of the power in the rederived spectra and need to be taken into account when rederiving the power spectrum from the correlation function.

For partial sky coverage the rederived power spectrum inhabit strong oscillations induced by the cut-off in the two-point correlation function. To read the information contained in the spectra, the oscillations have to be filtered out.

Once the oscillations are removed I found that most of the information in the higher l's is lost if the correlation function is measured with $N_{\text{bins}} < N_{\text{bins}}^{\text{opt}}$. The optimal number of bins to use at a given sky coverage in order to retrieve information about the desired number of multipoles, is given by

$$N_{\text{bins}}^{\text{opt}} = A\left(\frac{R_{\max}}{180^\circ}\right) l_{\max},$$

where A is a parameter in the range [10,20] when the maximum deviation between the binned and the unbinned power spectrum is set to 1%.

If $N_{\text{bins}} \gtrsim N_{\text{bins}}^{\text{opt}}$, the rederived power spectra differs very little. But they might still differ severely from the input power spectrum, so in the case of partial sky coverage the binning effect should be taken into account for all $R_{\max}$, when using Gauss-Legendre integration to rederive the power spectrum from the correlation function.

One way to correct for the binning effect at both full and partial sky coverage is to develop a binning window W_b from the relation ${C_l}^{\text{Binned}}/{C_l}^{\text{Theory}}$.

6.1.3 Filtering

When working with partial sky coverage, the rederived power spectrum inhabits an extra oscillation, where the wavelength is given by the sky coverage through the simple relationship:

$$\lambda_{\text{osc}} = \frac{360^\circ}{R_{\max}}$$

where λ is in units of l, and $R_{\max}$ is sky coverage in degrees.

The oscillations can successfully be filtered out by using a running average filter with filter width $\geq 2\lambda_{\text{osc}}$. For $R_{\max} \leq 30^\circ$ it is advisable to use a filter width equal to one λ_{osc}, otherwise the rederived power spectra will be suppressed.

FFT filtering was also tried, but was rejected because it was too cumbersome and did not remove the oscillations properly.

6.1.4 Statistical distribution

Both in the case of full and partial sky coverage, the two-point correlation function is found to have a χ^2 distribution.

The χ^2 distribution comes from the fact that C_l is quadratic and that $(2l+1)\cdot C_l$ goes as l^{-1}, and hence the lower multipoles are dominating the Gaussian distribution at the higher multipoles so that the total two-point correlation function becomes χ^2 distributed.

By removing the first 20 multipoles of the input power spectrum, it is possible to make the distribution of the two-point function Gaussian.

6.1.5 Alteration of the input power spectrum

When removing the first 20 multipoles from the input spectrum, the features of the correlation function become compressed and shifted towards smaller angles, and the decline at the very smallest angles is steepened correspondingly. This is highly likely to affect the rederived power spectrum and might also have consequences for the maximum likelihood analysis. Exactly how the alterations will affect the rederived power spectrum and which consequences it might have for the analysis have to be examined further.

6.1.6 The two-point two-point covariance matrix, M

The general analytic expression for the two-point two-point covariance matrix M can be written

$$\mathrm{M}_{ij} = \langle C_i \rangle \langle C_j \rangle + \langle \delta C_i \delta C_j \rangle.$$

From the two-point correlation function in Section 2.4 and the equations I derived in Chapter 3, I have developed analytical expressions for the covariance matrix M: In the case of full sky coverage M is given by

$$\mathrm{M}(\chi_1, \chi_2) = \langle C(\chi_1) \rangle \langle C(\chi_2) \rangle + \frac{1}{8\pi^2} \sum_l C_l^2 P_l(\mu_1) P_l(\mu_2).$$

With only limited sky coverage available, the covariance matrix is

$$\mathrm{M}(\chi_1, \chi_2)_{\mathrm{disk}} = \langle C(\chi_1)_{\mathrm{disk}} \rangle \langle C(\chi_2)_{\mathrm{disk}} \rangle + \frac{2 \sum_{ll'} P_l(\mu_1) P_{l'}(\mu_2) \sum_m \left(\sum_{l''} W^m_{ll''} C_{l''} W^m_{l'l''} \right)^2}{D(\chi_1) D(\chi_2)},$$

where $W^m_{l'l''}$ is given by Equation (5.24) and $D(\chi_i)$ is the same as $D(\chi)$ in the correlation function with partial sky coverage.

In the binned cases the equivalent correlation matrices are

$$\mathrm{M}(\chi_1, \chi_2)_{\mathrm{binned}} = \langle C(\chi_1)^{\chi_B}_{\chi_A} \rangle \langle C(\chi_2)^{\chi_D}_{\chi_C} \rangle + \frac{\sum_l C_l^2 k_l(\chi_1)^{\chi_B}_{\chi_A} k_l(\chi_2)^{\chi_D}_{\chi_C}}{8\pi^2 k_0(\chi_1)^{\chi_B}_{\chi_A} k_0(\chi_2)^{\chi_D}_{\chi_C}},$$

and

$$\begin{aligned} \mathrm{M}(\chi_1, \chi_2)_{\text{binned disk}} &= \langle C(\chi_1)^{\chi_B}_{\chi_A, disk} \rangle \langle C(\chi_2)^{\chi_D}_{\chi_C, disk} \rangle \\ &+ \frac{\sum_{ll'} k_l(\chi_1)^{\chi_B}_{\chi_A} k_{l'}(\chi_2)^{\chi_D}_{\chi_C} \sum_m \left(\sum_{l''} W^m_{ll''} C_{l''} W^m_{l'l''} \right)^2}{4\pi^2 D(\chi_1)^{\chi_B}_{\chi_A} D(\chi_2)^{\chi_D}_{\chi_C}}, \end{aligned}$$

where $D(\chi_i)_{\chi_a}^{\chi_b}$ is the same as $D(\chi)_{\rm bin}$ in the binned correlation function with partial sky coverage.

All these four expressions for M are of the same form as the general analytic expression above.

When using the Gaussian maximum likelihood to estimate the power spectrum from the correlation function, the two-point two-point correlation matrix M must be inverted, and in order to do this the matrix must be non-singular. Because of time limitations I have not been able to examination this matter further, so whether M is invertible or not will have to be a subject for future investigation.

It is possible to perform a χ^2 maximum likelihood analysis using the correlation function with the unaltered input power spectrum, but in this case the variates are coupled and have to be calculated iteratively. Compared to the Gaussian variates which are independent and thus only need to be calculated once, this is a time consuming process and could make the correlation an undesirable component in CMB analysis.

6.2 Problems for future work

During my work with this thesis there are two important questions that have emerged, but which I, because of time limitations, have not been able to answer within the scope of this thesis.

First, what happens when parts of the power spectrum is not included in the calculations of the two-point correlation function? We have already seen how this alters the shape of the correlation function, but not including all multipoles in the calculations of the two-point function is highly likely to affect the rederived power spectrum as well, and might also have consequences for the maximum likelihood analysis. How the alterations will affect the rederived power spectrum, and even more important, which consequences it might have for the maximum likelihood analysis is a subject for future work.

Second, if there is to be any point in using the two-point correlation function as an intermediate representation of the pixel data in CMB analysis, we need to be able to perform a Gaussian maximum likelihood analysis to estimate the power spectrum from the correlation function. This means that the two-point two-point correlation matrix M must be invertible, *i.e.* non-singular. To find out if whether M is invertible or not, we need to calculate M analytically, using one of the four expressions I have developed in this thesis.

It could also be of interest to develop a binning window W_b from the relation ${C_l}^{\rm Binned}/{C_l}^{\rm Theory}$, since I found that in the more realistic case of partial sky coverage, the binning effect should be taken into account in experiments where the number of

bins available is less than $N_{\rm bins}^{\rm opt}$. For experiments like WMAP and Planck, though, with arc minute resolution and full sky coverage, the binning effect will be insignificant.

Appendix A

Properties of spherical harmonics

Orthonormality function

$$\int_0^{2\pi}\int_0^{\pi} Y^*_{l'm'}(\theta,\phi)Y_{lm}(\theta,\phi)\sin\theta d\theta d\phi = \delta_{l,l'}\delta_{m,m'}. \tag{A.1}$$

The addition theorem for spherical harmonics for two given direction unit vectors on the sphere

$$P_l(\cos\alpha_{12}) = \frac{4\pi}{2l+1}\sum_m Y^*_{lm}(\theta_1,\phi_1)Y_{lm}(\theta_2,\phi_2). \tag{A.2}$$

The angle between the two unit vectors is

$$\cos\alpha_{12} = \cos\theta_1\cos\theta_2 + \sin\theta_1\sin\theta_2\cos(\phi_1-\phi_2). \tag{A.3}$$

Spherical harmonics as a function of associated Legendre polynomials

$$Y_{lm}(\Omega) = A_{lm}P_{lm}(\cos\theta)e^{im\phi}, \tag{A.4}$$

where

$$A_{lm} = \sqrt{\frac{(2l+1)}{4\pi}\frac{(l-m)!}{(l+m)!}}. \tag{A.5}$$

Special functions

$$Y_{00}(\theta,\phi) = Y^*_{00}(\theta,\phi) = \frac{1}{\sqrt{4\pi}}. \tag{A.6}$$

Appendix B

Properties of Legendre polynomials

Orthogonality and normalisation relation

$$\int_{-1}^{1} P_l(x)P_{l'}(x)dx = \frac{2\delta_{l,l'}}{2l+1}. \tag{B.1}$$

Recursion formula for Legendre polynomials

$$(2l+1)P_l(x) = \frac{d}{dx}P_{l+1}(x) - \frac{d}{dx}P_{l-1}(x) \tag{B.2}$$

for $l \geq 1$.

Recursion formula for associated Legendre polynomials

$$\frac{P_{l-1,m}(x) - P_{l+1,m}(x)}{(2l+1)} = \sqrt{1-x^2}P_{l,m-1}(x) \tag{B.3}$$

for $l \geq 1$.

Special functions

$$P_0(x) = 1. \tag{B.4}$$

Bibliography

Adams, W. S.: 1941, ApJ **93**, 11

Alpher, R. A., Follin, J. W., and Herman, R. C.: 1953, *Physical Review* **92**, 1347

Alpher, R. A. and Herman, R. C.: 1949, *Physical Review* **75**, 1089

Baker, J. C. *et al.*: 1999, MNRAS **308**, 1173

Balbi, A. *et al.*: 2001, ApJ **558**, L145

Bennett, C. L. *et al.*: 1996, ApJ **464**, L1+

Bennett, C. L. *et al.*: 2003a, *First Year Wilkonson Microwave Anisoptropy Probe (WMAP) Observations: Foreground Emission*, preprint astro-ph/0302208

Bennett, C. L. *et al.*: 2003b, *First Year Wilkonson Microwave Anisoptropy Probe (WMAP) Observations: Preliminary Maps and Basic Results*, preprint astro-ph/0302207

Benoît, A. *et al.*: 2003, A&A **399**, L19

Bersanelli, M., Bensadoun, M., de Amici, G., Levin, S., Limon, M., Smoot, G. F., and Vinje, W.: 1994, ApJ **424**, 517

Bhattacharyya, G. K. and Johnson, R. A.: 1977, *Statistical Concepts and Methods*, J. Wiley & Sons

Birkinshaw, M.: 1999, Phys. Rep. **310**, 97

Boas, M. L.: 1983, *Mathematical Methods in the Physical Sciencies*, J. Wiley and Sons, 2nd edition

Bond, J. R., Efstathiou, G., Lubin, P. M., and Meinhold, P. R.: 1991, Phys. Rev. Lett. **66**, 2179

Bond, J. R., Jaffe, A. H., and Knox, L.: 1998, Phys. Rev. D **57**, 2117

Bond, J. R., Jaffe, A. H., and Knox, L.: 2000, ApJ **533**, 19

Carlstrom, J. E. and DASI Collaboration: 2000, *American Astronomical Society Meeting* **197**, 0

Christensen, N., Meyer, R., Knox, L., and Luey, B.: 2001, *Classical and Quantum Gravity* **18**, 2677

de Bernardis, P. *et al.*: 1990, ApJ **360**, L31

Dicke, R. H., Peebles, P. J. E., Roll, P. G., and Wilkinson, D. T.: 1965, ApJ **142**, 414

Dodelson, S. and Jubas, J. M.: 1993, Phys. Rev. Lett. **70**, 2224

Doroshkevich, A. G. and Novikov, I., D.: 1964, *Soviet Phys. Doklady* **9**, 111

Douspis, M., Bartlett, J. G., Blanchard, A., and Le Dour, M.: 2001, A&A **368**, 1

Eriksen, H. K.: 2002, *Master's thesis*, ITA, UiO

Eriksen, H. K., Banday, A. J., and Górski, K. M.: 2002, A&A **395**, 409

Fischer, M. L. *et al.*: 1991, in *AIP Conf. Proc. 222: After the first three minutes*, pp 123–128

Fraser, G., Lillestøl, E., and Sellevåg, I.: 1995, *The search for infinity : solving the mysteries of the universe*, New York : Facts on File

Górski, K. M., Wandelt, B. D., Hansen, F. K., Hivon, E., and Banday, A. J.: 2000, *The HEALPix Primer*, preprint astro-ph/9905275

Grainge, K. *et al.*: 2002, *The CMB power spectrum out to $\ell = 1400$ measured by VSA*, astro-ph/0212495

Hinshaw, G. *et al.*: 2003, *First Year Wilkonson Microwave Anisoptropy Probe (WMAP) Observations: The Angular Power Spectrum*, preprint astro-ph/0302217

Hoyle, F.: 1948, MNRAS **108**, 372

Hu, W. and Sugiyama, N.: 1996, ApJ **471**, 542

Hu, W. and White, M.: 1996, ApJ **471**, 30

Hu, W. T.: 1995, *Ph.D. Thesis*

Hwang, J., Padmanabhan, T., Lahav, O., and Noh, H.: 2002, Phys. Rev. D **65**, 43005

Jungman, G., Kamionkowski, M., Kosowsky, A., and Spergel, D. N.: 1996, Phys. Rev. D **54**, 1332

Kamionkowski, M., Spergel, D. N., and Sugiyama, N.: 1994, ApJ **426**, L57

Kosowsky, A.: 2002, in *Modern Cosmology*, pp 219–+

Mauskopf, P. D. *et al.*: 2000, ApJ **536**, L59

McKellar, A.: 1940, PASP **52**, 187

Melchiorri, A. *et al.*: 2000, ApJ **536**, L63

Miller, A. D. *et al.*: 1999, ApJ **524**, L1

Ostriker, J. P. and Vishniac, E. T.: 1986, ApJ **306**, L51

Page, L. *et al.*: 2003, *First Year Wilkonson Microwave Anisoptropy Probe (WMAP) Observations: Interpretation of the TT and TE Power Spectrum Peaks*, preprint astro-ph/030220

Partridge, R. B.: 1995, *3K: The cosmic microwave background radiation*, Cambridge Astrophysics Series, Cambridge, New York: Cambridge University Press

Peacock, J. A.: 1999, *Cosmological physics*, Cambridge University Press, 1999.

Peebles, P. J. E.: 1973, ApJ **185**, 413

Penzias, A. A. and Wilson, R. W.: 1965, ApJ **142**, 419

Perlmutter, S. *et al.*: 1999, ApJ **517**, 565

Persi, F. M., Spergel, D. N., Cen, R., and Ostriker, J. P.: 1995, ApJ **442**, 1

Plionis, M.: 2002, in *LNP Vol. 592: Cosmological Crossroads*, pp 147–+

Press, W. H., Teukolsky, S. A., Vetterling, W. T., and Flannery, B. P.: 1992, *Numerical recipes in FORTRAN. The art of scientific computing*, Cambridge: University Press, 2nd edition

Readhead, A. C. S., Lawrence, C. R., Myers, S. T., Sargent, W. L. W., Hardebeck, H. E., and Moffet, A. T.: 1989, ApJ **346**, 566

Rephaeli, Y.: 1995, ARA&A **33**, 541

Riess, A. G. *et al.*: 1998, AJ **116**, 1009

Rottmann, K.: 1991, *Mathematische Formelsammlung*, Bracan Forlag, 4th edition

Sachs, R. K. and Wolfe, A. M.: 1967, ApJ **147**, 73

Sæbø, T. O.: 2002, *Master's thesis*, ITA, UiO

Seljak, U.: 1996, ApJ **463**, 1

Seljak, U. and Zaldarriaga, M.: 1996, ApJ **469**, 437

Smoot, G. F. *et al.*: 1992, ApJ **396**, L1

Spergel, D. N. *et al.*: 2003, *First Year Wilkonson Microwave Anisoptropy Probe (WMAP) Observations: Determination of Cosmological Parameters*, preprint astro-ph/0302209

Sunyaev, R. A. and Zel'dovich, I. B.: 1980, ARA&A **18**, 537

Sunyaev, R. A. and Zel'dovich, Y. B.: 1970, Ap&SS **7**, 3

Tegmark, M.: 1995, *Doppler Peaks and all that: CMB anisotropies and what they can tell us*, preprint astro-ph/9511148

Tegmark, M. and Efstathiou, G.: 1996, MNRAS **281**, 1297

Tytler, D., O'Meara, J. M., Suzuki, N., and Lubin, D. .: 2000, Phys. Rep. **333**, 409

Verde, L. *et al.*: 2003, *First Year Wilkonson Microwave Anisoptropy Probe (WMAP) Observations: Parameter Estimation Methodology*, preprint astro-ph/0302218

Wandelt, B. D. and Hansen, F. K.: 2003, Phys. Rev. D **67**, 23001

Wandelt, B. D., Hivon, E., and Górski, K. M.: 2001, Phys. Rev. D **64**, 83003

Watts, P. and Coles, P.: 2003, MNRAS **338**, 806

Winant, C. D. *et al.*: 2000, *American Astronomical Society Meeting* **196**, 0